MEASUREMENT OF SPALLATION RESIDUALS IN MERCURY FOR ACCELERATOR FACILITY TARGETS

A Dissertation
Presented to
The Academic Faculty

By

Dwayne Patrick Blaylock

In Partial Fulfillment
Of the Requirements for the Degree
Doctor of Philosophy in Nuclear and Radiological Engineering

Georgia Institute of Technology
May 2016

MEASUREMENT OF SPALLATION RESIDUALS IN MERCURY FOR ACCELERATOR FACILITY TARGETS

Approved By:

Dr. Nolan Hertel, Advisor
School of Mechanical Engineering
Nuclear and Radiological Engineering Program
Georgia Institute of Technology

Dr. Jiri (Art) Janata
School of Chemistry
Georgia Institute of Technology

Dr. Bojan Petrovic
School of Mechanical Engineering
Nuclear and Radiological Engineering Program
Georgia Institute of Technology

Dr. Phillip Ferguson
Oak Ridge National Laboratory

Dr. C.K. Chris Wang
School of Mechanical Engineering
Nuclear and Radiological Engineering Program
Georgia Institute of Technology

Date Approved: March 21, 2016

ACKNOWLEDGEMENTS

To Amy, my wife and best friend thank you for your encouragement and support through the preparation of this dissertation.

I would like to thank the following two individuals for their continued support, encouragement and guidance in the development and preparation of this work. To Dr. Nolan Hertel, I'm am grateful for the opportunities I have had to work with you on this dissertation and other projects over the years. To Dr. Philip Ferguson, for your help with the original project comparing measured spallation residuals from the start up sample at SNS that led to this experiment and for your help in the development of the experiment and coordination of resources at ORNL to help with his work.

To Mr. Robert Sangrey, thank you for the help in filling and weighing the experimental targets with mercury and emptying them for the final stage of analysis.

To Dr. Franz Gallmeier, Dr. Eric Iverson, Mrs. Wendy Brooks, thank you for the hours of help in acquiring computer access to ORNL and for the assistance in the discussions on the results of the MCNPX production cross section cases throughout this work.

To Dr. W. David Kulp and Mr. Bernie Riemer, I'm grateful for the assistance during the irradiation of the experimental targets and the gamma spectroscopy setup at LANSCE.

To Mrs. Christina Tabor and Mr. Gary Spichiger, thank you for the assistance in receiving and shipping the irradiated mercury sample to and from Georgia Tech.

TABLE OF CONTENTS

LIST OF TABLES

LIST OF FIGURES

LIST OF ABBREVIATIONS

A	Atomic Mass Number
Ag	Silver
Al	Aluminum
AMS	Accelerator Mass Spectroscopy
Au	Gold
C/M	Calculated vs. Measured
Ce	Cerium
Co	Cobalt
Cs	Cesium
CSNS	Chinese Spallation Neutron Source
Er	Erbium
ESS	European Spallation Source
Eu	Europium
FGR	Federal Guidance Report
Gd	Gadolinium
GeV	Giga-Electron Volt
GSI	Gesellschaft fuer Schwerionenforschung
Hf	Hafnium
Hg	Mercury
Ho	Holmium
HPGe	High Purity Germanium
IAEA	International Atomic Energy Agency

ICRP	International Counsel on Radiation Protection
IHEP	Institute of High Energy Physics
INC	Intra-Nuclear Cascade
Ir	Iridium
ITEP	Institute for Theoretical and Experimental Physics
J-PARC	Japan Proton Accelerator Research Complex
keV	kilo-electron volt
LAHET	Los Alamos High-Energy Transport
LAMPF	Los Alamos Meson Physics Facility
LANSCE	Los Alamos Neutron Science Center
Lu	Lutetium
mb	milli-barn
MCNP	Monte Carlo N-Particle
MCNPX	Monte Carlo N-Particle Extended
Mn	Manganese
Na	Sodium
nA	nano-Ampere
Nb	Niobium
NIST	National Institute of Standards and Technology
ORNL	Oak Ridge National Laboratory
Os	Osmium
Pb	Lead
Pm	Promethium
Pt	Platinum
QMD	Quantum Molecular Dynamics

Rb	Rubidium
Re	Rhenium
Rh	Rhodium
Sb	Antimony
Se	Selenium
Sn	Tin
SNS	Spallation Neutron Source
SS316	Stainless Steel Type 316
T1/2	Half-life
Ta	Tantalum
Tl	Thallium
Tm	Thulium
U	Uranium
W	Tungsten
WNR	Weapons Neutron Research
Y	Yttrium
Yb	Ytterbium
Z	Atomic Number
Zn	Zinc
Zr	Zirconium
ZSR	Zentrum fuer Strahlenschutz und Radiooekologie Universitaet

SUMMARY

Two accelerator facilities, the Spallation Neutron Source in the United States and the Japan Proton Accelerator Complex make use of a flowing liquid mercury spallation target for the production of neutrons. While the use of mercury is advantageous for higher power proton beam operations due the enhanced cooling capabilities over solid metal targets, the use of mercury can lead to other radiation safety challenges due to residual radioisotopes circulating and depositing within the target system. While benchmark data exists for the production cross sections of residuals in solid targets no data currently exists for a mercury target. Developing a set of production cross section data for spallation in mercury is one motivation for this work. The second motivation is to study the distribution and deposition of the residuals from a mercury target to provide knowledge for the operation, maintenance and radiological safety of spallation facilities using mercury targets.

An experiment was conducted with two small volume mercury targets at the Weapon Neutron Research facility at the Los Alamos Neutron Science Center that measured the production cross sections of 53 medium and longer-lived spallation residuals using gamma spectroscopy. The measured cross sections were then compared with predicted cross sections from the MCNPX code. After acquisition of the gamma spectroscopy data the targets were drained and disassembled to study the distribution and the deposition of the spallation residuals.

CHAPTER 1: INTRODUCTION

One method of producing a broad energy range of neutrons for experimental applications is through the use of accelerators. Accelerator production of neutrons can be accomplished via accelerating protons to high energies ($600 MeV \lesssim E \lesssim 3.0 GeV$) and inducing spallation of nuclei in a target made of heavy metal. Several facilities, notably the Swiss Spallation Neutron Source (SINQ), the Los Alamos Neutron Science Center (LANSCE) in the United States and the ISIS Pulsed Neutron and Muon facility in the United Kingdom use solid metal targets, typically tungsten, for the production on the neutrons. The planned European Spallation Source (ESS) and the Chinese Spallation Neutron Source (CSNS) are also designed to use solid metal targets. Two other primer facilities, the Spallation Neutron Source (SNS) in the United States, and the Japan Proton Accelerator Research Complex (J-PARC), use liquid mercury targets.

While tungsten and mercury both make good targets for the production of neutrons for experiments there are advantages and drawbacks to either choice of target. The primary drawback of a metal target is maintaining cooling and the resulting limit on the proton beam power. While liquid metal targets allow for efficient cooling of the target, they also present radiation safety challenges with radioisotopes from the resulting spallation reaction are circulated and deposited throughout the target system. In contrast the radioisotopes in a solid metal target are fixed within the target making the possibility of contamination from target system maintenance less likely.

In spallation facilities, the spallation nuclear reaction occurs when the accelerated proton interacts with a target nucleus. The spallation reaction is a two-step process consisting of an intranuclear cascade followed by evaporation-fission stage [49]. During

the intranuclear cascade the incoming proton interacts with the individual nucleons of the target nucleus. These individual interactions may cause other nucleons to be released from the target nucleus. Following the intranuclear cascade, the target nucleus is left in an excited state. The resulting excited nucleus may relieve its excitation energy via one of two processes. The first process is through fission of the excited nucleus. The second process is through the evaporation of nucleons or small groups of nucleons until the excitation energy of the target nucleus falls below the nucleon binding energy. The remaining excitation energy is released via gamma-ray emissions.

In 2008, the International Atomic Energy Agency (IAEA) along with the Abdus Salam International Center for Theoretical Physics (ICTP) organized a benchmark committee to review computer codes simulating the spallation reaction. The spallation reaction is typically modeled through a two-stage process using Monte Carlo techniques. The first stage implemented by these codes is a model of the Intra-Nuclear Cascade (INC), or a Quantum Molecular Dynamics (QMD) model. The INC models reviewed by the benchmark committee were: Bertini, CEM, INCL and ISABEL [1]. While models such as JQUMD, QMD-SDM, BUU and SMM that implement a QMD model [1] were part of the benchmark review. After the initial simulation of the reaction the original nucleus in both INC and QMD models remains in an excited state. The second stage resulting in the removal of the excess excitation energy from the target nucleus is determined other models. These are typically an evaporaton/fisson model or combination of models such as ABLA, GEM, GEMINI or a list of others [1]. For spallation facilities, one or more of these models are incorporated into a Monte Carlo simulation code. The Monte Carlo simulation codes MCNPX [2], FLUKA [45, 46], GEANT [47, 48] and PHITS [44] being the most frequently used.

The initial meeting of the benchmark committee brought together physics model developers who presented the different computational models that were participating in

the benchmark and experimentalists from spallation data measurements. During this meeting, a set of experimental data were agreed upon by the participants. These experiments were to be to be calculated with the various physics models. The goal, to determine how well the various codes modeled the various emissions from the spallation reaction. The chosen experimental data covered an energy range of 40 – 3,000 MeV consisting of several different target materials, with data incorporating neutron and light particles from protons to alphas, pions and residuals. For residuals the experimental data sets selected were from the proton irradiation of iron, lead or uranium targets. The methods of measurement of the production cross sections of these residuals ranged from x-ray and gamma-ray spectroscopy, to accelerator mass spectrometry (AMS), to fragment separation. Many of the experiments involved the irradiation of thin foils. This type of experiment is designed to give an energy specific production cross section free of contamination from the reactions from high energy secondary nucleons emitted from the initial spallation reaction. The fragment separator experiment involves the acceleration on a target ion beam into a liquid H_2 target and measuring the mass and charge of the residuals escaping the target. While these methods provide good benchmark data for code developers to model the spallation reaction and individual particles they are not an ideal match to many spallation facilities where the target is thicker and secondary reactions from high-energy protons, neutrons and pions also contribute to the production of radionuclides in the target material.

In thick solid targets the combination of the loss of energy of the proton beam as it penetrates the target along with the secondary reactions results in a heterogeneous distribution of radioisotopes within the target. However with flowing liquid targets as found at SNS and J-PARC the distribution of residual radionuclides is mixed by the flowing target liquid making a quasi-homogeneous mixture. To determine the production rate of the residuals in liquid targets and to provide a benchmark that tests the physics modeling of

both the initial spallation reaction and of secondary reactions a moderately thick target of liquid mercury was designed, irradiated and spallation residuals analyzed in this dissertation.

The secondary goal in this dissertation is to provide additional information regarding the distribution of the residual radionuclides in the quasi-homogeneous mixture including residuals that remain in the mercury and those that separate from the mercury and can deposit on piping and equipment. Both the SNS and J-PARC have target assemblies in which the liquid mercury flows that can be replaced on a regular basis. Each replacement results in the opening of the mercury systems and can result in contamination of the target cell. After replacement and a period of decay the used target assembly is ultimately disposed of as radioactive waste. Knowledge of the residuals that remain in and/or fall out of the mercury can assist in the decontamination of the cell as well as the decontamination, segregation, packaging and disposal of the target assembly. As the spallation facilities age, information on the distribution of the residuals that deposit on the pipe and equipment can assist health physics offices in the planning and execution of maintenance tasks.

CHAPTER 2: BACKGROUND

2.1 MCNPX

One of the common codes used to model the spallation events including the production of residuals is MCNPX [2]. In MCNPX the simulation of radiation transport through materials is accomplished via Monte Carlo techniques. MCNPX is an extension of the Los Alamos Monte Carlo N-Particle (MCNP) [50] and the Los Alamos High Energy Transport (LAHET) [3] codes. The LAHET code is a Los Alamos modification of the HETC [51] Monte Carlo code originally developed at Oak Ridge National Laboratory. In general the LAHET physics portion of MCNPX is used for energies greater than 150 MeV. Below this threshold, tabular cross section data are used in the modeling of neutron transport. Above this threshold the user must choose between two or more physics models. The default physics model was chosen in this work to model and compare to the experimental results of the irradiated mercury target. The default physics models of MCNPX are: Bertini Intranuclear cascade [4,5], the multi-stage preequilibrium excitation model (MPM) [6], Dresner evaporation with Gilbert-Cameron-Cook-Ignatyuk (GCCI) level density [7], and the Rutherford Appleton Library (RAL) [8] fission model.

The Bertini intranuclear cascade model is used to describe nucleon-nucleus interaction below 3.5 GeV and pion-nucleon interactions below 2.5 GeV through the use of approximations instead of the tracking of individual nucleons. These approximations have proven appropriate for most applications. The model starts with the incident nucleon entering the nucleus at a point uniformly selected over a projection area. The total particle-particle cross-section and a region-dependent nucleon density are used to determine the path length of the incoming nucleon. In the Bertini model, the nucleus is modeled as three nested concentric spheres each with a uniform density of neutrons and protons. The

Fermi-type charge-distribution function is used to determine the radii of the various spheres according to fractions of the central density. Once the incoming particle interacts with the nucleus, statistical sampling is used to determine the type of reaction, momentum, and scattering angle of the reaction product. Up to four different types of reactions are considered: 1.) scattering, 2.) production of π-mesons, 3.) pion absorption, and 4.) charge exchange scattering (for π-nucleon interactions). The cascade continues until the energy of the excited nucleus is ~7-10 MeV above its Fermi breakup energy. The kinetic energy of the cascading particles is adjusted based on the electrical potential between the various regions of the modeled nucleus as the particle crosses the region boundaries. The majority of the time the cascading particle energy is large and the particle passes undisturbed through the nucleus.

Once the Bertini model is complete, MCNPX uses the MPM preequilibrium model. The MPM models starts with the initial excitation energy, hole-particle exchanges and exciton number (sum of the number of excited holes and pairs) as determined by the Bertini INC model. If the exciton number is greater than the equilibrium exciton number then further emission of fragments is simulated through statistical sampling. The additional fragments emitted may be a neutron, proton, deuteron, triton, ^{3}He, or an alpha particle. Fission of the nucleus is not considered at this stage. The MPM model determines the kinetic energy, scattering angle, and the momentum of the emitted fragment. Once a particle is emitted the state of the nucleus is updated and the model repeated until the equilibrium exciton number is reached. When the equilibrium excition number is reached then MCNPX proceeds to use an evaporation/fission model to simulate the emission of the remaining excitation energy in the nucleus.

The Dresner evaporation model is the next step in modeling the spallation reaction to relieve the excitation energy. This is accomplished through the emission of a neutron, proton, deuteron, triton, ^{3}He or alpha particle via Monte Carlo sampling. Alternatively if

the emission of a neutron is selected then the Rutherford Appleton Laboratory (RAL) fission model by Atchison may be applied using the fission probability. The RAL model allows fission for both actinides ($Z \geq 89$) and for subactinides ($71 \leq Z \leq 88$) but uses different routines for each group. For mercury in the subactinide group, a statistical model used is determine the probability of fission based on the fission barrier energy. The fission barrier energy is a function of (A, Z) and the excitation energy of the nucleus and is determined by the difference between the stability saddle-point and ground state mass. It should be noted, however that the subactinide fission routine may suppress fission for some subactinidies at intermediate energies. Based on the evaporation/fission models the production rates of the spallation residuals are determined.

2.2 Cinder'90

The CINDER'90 [9] code is the result of several evolutions of development at the Los Alamos National laboratory of the work originally developed by T. England at the Bettis Atomic Power Laboratory in the early 1960's. The code calculates the atom density and the activity density (curies per unit volume) of radionuclides present at specified units of time. The latest version of the CINDER'90 code contains data for a total of 3400 nuclides in the range of $1 \leq Z \leq 103$. The atom or activity density is determined through solving the differential equation that describes the rate of change in atom density as given by Equation (1).

$$\frac{dN_m(t)}{dt} = -N_m(t)(-\lambda^m + \phi\sigma_a^m) + R_m + \sum_{k \neq m} N_k \gamma_{k \to m} \qquad (1)$$

The initial term on the right hand side of the equation describes the rate of loss of atoms of the nuclide *m* from either decay or transmutation through absorption when exposed to a neutron flux. The following summation term gives the rate of gain of atoms of the nuclide *m* through the radioactive decay of all other nuclides *k*. R_m is the rate of

production of the nuclide from non-decay sources. Ultimately the coupled differential equations of the 3400 nuclides are solved using the Markov method. In this work CINDER'90 was used to compute the spallation residuals from an irradiated target. The highest activity nuclides calculated by CINDER'90 at various times of decay were used to create the gamma spectroscopy data libraries that assists the spectroscopy software locate and identify full energy gamma-ray photopeaks. To determine rate of production of the spallation residuals and the neutron flux, the irradiation experiment was modeled in MCNPX. An activation script [10] written by F. Gallmeier and M. Wohlmuther was used to prepare the CINDER'90 input file from the MCNPX output.

2.3 Previous spallation residual measurements

Spallation residual yields have been measured in the past for protons on tungsten, tantalum and gold [11-20] in the energy range of 500 to 800 MeV. The production cross sections were measured in 10 of these experiments via gamma spectroscopy, 3 by radiochemical analysis, and 1 via a fragment separator. More recent measurements via a fragment separator involving ^{208}Pb and ^{238}U [23-28] have been performed. When spallation models have been compared to these measurements the production cross section is generally within a factor of two of the measured cross section. Spallation residual measurements of 800 MeV protons on ^{197}Au were made at Gesellschaft fuer Schwerionenforschung (GSI) in Darmstadt, Germany, Institute for Theoretical and Experimental Physics (ITEP) in Russia and Zentrum fuer Strahlenschutz und Radiooekologie Universitaet (ZSR) in Germany were compared to the LAHET code [21]. In these experiments the average mean squared deviation factor was 2.8. However the paper did not note which of the physics models in LAHET were used. A measurement by Mashnik et al. [22] also made a comparison between simulations and experimental measurements. In general it was found that simulations were reasonable with the

experimental measurements in the region of residuals close to the target nuclide (evaporation region). Comparisons of residuals further away from the target nuclide (fission region) were comparably worse.

2.4 Los Alamos Neutron Science Center

The Los Alamos Neutron Science Center (LANSCE) is consists of an 800 MeV proton linear accelerator that provides beam current to five major facilities. These facilities are, the Proton Radiography Facility, the Isotope Production Facility, an Ultra-cold Neutrons facility, the Lujan Neutron Scattering Center and the Weapons Neutron Research (WNR) Facility. An overall layout of LANSCE and the five facilities is shown in Figure 1.

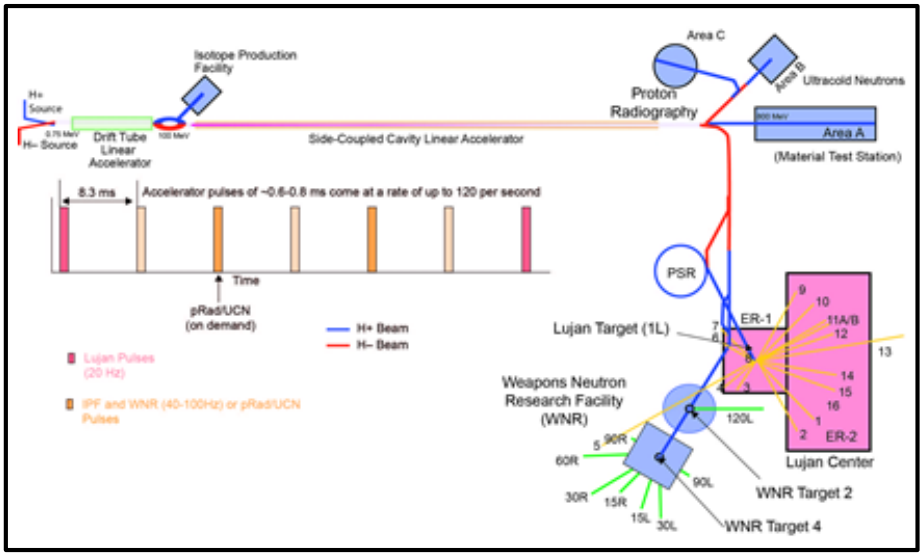

Figure 1: LANSCE facility layout

WNR Target 2, commonly referred as the “Blue Room” was used for the proton irradiation of the designed liquid mercury targets in this dissertation. The Blue Room is a large domed room with a diameter of 40 feet with the main floor elevated 20 feet above the basement floor that minimizes neutron scatter to experiments within the beam path at the center of the room. A beam current of up to 80 nA of 800 MeV protons is available for

experiments requiring direct access to the proton beam. Irradiations within the Blue Room can take place in either a sole use or a parasitic mode depending on the status of other experiments that may ongoing from neutrons produced in the solid metal Target 4 immediately downstream of the Blue Room. All irradiations in this dissertation were conducted in sole use mode, meaning that Target 4 was used as a beam stop and not for the production of neutrons.

CHAPTER 3: METHODS

There have been two common ways to determine the production of spallation residuals in a targets. The first method is via a thick target experiment, where a target similar to a facility target is irradiated. The experimental target is then sliced into thin layers to determine the production within small proton energy intervals. With the proton energy being degraded as it passes through the target each slice can be used for a specific proton energy range. The individual slices are then assayed to determine the quantity of residuals produced. This gives a measurement of the production rate of the residuals of concern as a function of depth in the target thus giving the production rates as a function of proton energy. The primary concern with this type of experiment is contamination from high-energy secondary particles.

The second and more common method is via a thin foil experiment. In the thin foil experiment, the proton energy loss through the foil is negligible resulting in a production cross-section measurement for the incident proton energy. Many of the IAEA benchmark experimental results were determined using this method enabling a fine-tuning of the results from the various spallation reaction models. However for liquid targets neither method is suitable so a new method was used to provide a benchmark for the development of nuclear physics models and the design of facilities using liquid targets.

In order to provide a benchmark for a liquid target, a small target using mercury in a stainless steel encapsulation with thin entry and exit windows was designed for irradiation. To determine the production rates of both medium (hours to days) and longer (days to years) half-life spallation residuals the thickness of the target and irradiation time were adjusted so gamma spectroscopy counting could be performed on the samples shortly after irradiation while still allowing a sufficient amount of longer half-life residuals to be produced for gamma spectroscopy counting after significant decay periods. Secondly,

due to the self-shielding effect to lower energy gamma-rays in the target mercury the thickness of the target was limited to maximize detection efficiency.

3.1 Experimental setup

The final configuration of the target taking into account the variables above was a volume of mercury that measured 1.73 cm thick by 3.175 cm in radius. The mercury was encapsulated in a Stainless Steel (Type 316) enclosure. The sidewalls of the encapsulation measured 2.525 cm thick with the entry and exit target windows were milled to 0.33 cm thickness. The target assembly was then mounted within a polyethylene enclosure acting as a secondary containment per LANSCE facility requirements. The thickness of the polyethylene sidewalls measured 0.356 cm. See Figures 2 and 3 showing the final target assembly MCNP model and photo of the assembly prior to irradiation.

The loss of energy of the proton beam while traveling through the polyethylene sidewall of the secondary container and through the stainless steel window is minimal, less than 0.6% of the incoming 800 MeV protons. The 800 MeV protons in turn lose approximately 3.7% of their energy as they pass through the mercury of the target. For the experiment two separate targets filled with mercury were irradiated and measured via gamma spectroscopy at various times after the irradiation. In addition a third target assembly without mercury in the central cavity was irradiated to provide characteristic gamma lines from the SS316 windows. The target assembly and encapsulation were placed in the centerline of the beam of the LANSCE facility in the approximate center of the “blue room” for irradiation with 800 MeV protons. A phosphor monitor screen provided the measurement of the size of the proton beam, which was a radius of ~0.5cm.

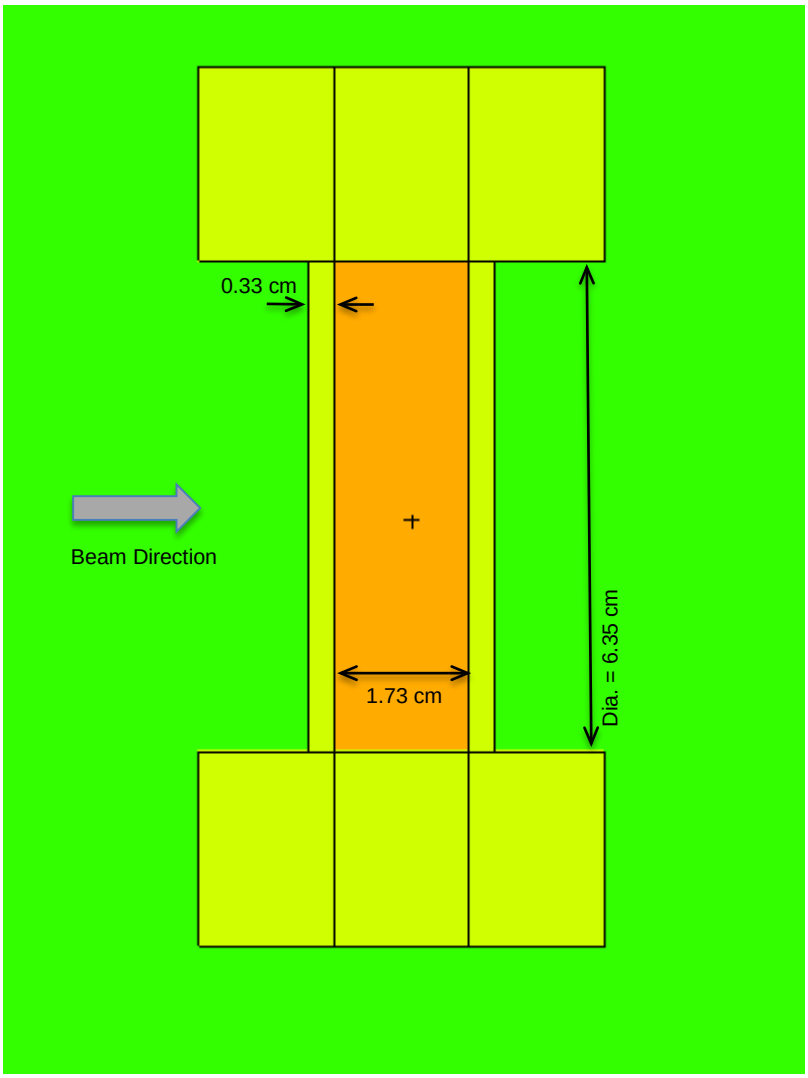

Figure 2: MCNP Model of Mercury Filled Target Assembly

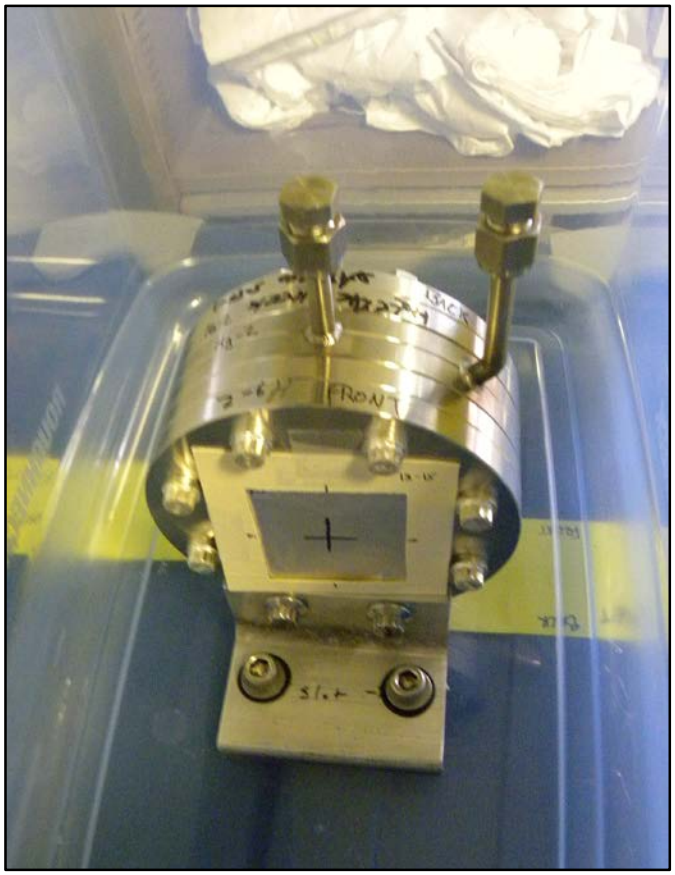

Figure 3: Photo of Target Mounted in Polyethylene Enclosure Prior to Irradiation

3.2 Calculation of cross sections

Within each mercury target there were a total N_{Hg} atoms that were irradiated with a proton flux density ϕ (p / cm^2-s^1). The total rate of production of any spallation residual (X) is given by:

$$R_X = N_{Hg}\phi\sigma_X \tag{2}$$

Where σ_X is the production cross section for the Hg(p,x)X reactions. The activity A_0 of the spallation residual of concern at the end of an irradiation lasting t_{irr} is:

$$A_X(0) = R_X(1 - e^{-\lambda_X t_{irr}}) \tag{3}$$

Where, λ_x is the known decay constant of the spallation residual (X) being measured. Then for any decay time after the irradiation, t_d the activity of the residual is given by

$$A_X(t_d) = A_x(0)e^{-\lambda_X t_d} \tag{4}$$

After this period of decay, the target was measured via gamma spectroscopy. The time of the gamma spectroscopy measurement is t_c. The total number of counts under a photopeak in the measurement spectrum is

$$C(E_\gamma) = \int_{t_d}^{t_d+t_c} A(t)\varepsilon(E_\gamma)I_\gamma(E_\gamma)dt \tag{5}$$

With $\varepsilon(E_\gamma)$ and $I_\gamma(E_\gamma)$ being the efficiency of the detector and the branching ratio, respectively, for the gamma-ray of energy E_γ. After solving for the integral in Equation (5) and combining it with Equations (3) and (4), the rate of production of the residual of concern can be determined by the total number of counts in a measured energy peak.

$$C(E_\gamma) = \frac{R_X\varepsilon(E_\gamma)I_\gamma(E_\gamma)}{\lambda_X}\left(e^{-\lambda_X t_d}(1-e^{-\lambda_X t_c})(1-e^{-\lambda_X t_{irr}})\right) \tag{6}$$

Combining Equation (6) with Equation (1) the production cross section for the residual of concern is:

$$\sigma_X = \frac{C(E_\gamma)\lambda_X}{N_{Hg}\phi\varepsilon(E_\gamma)I_\gamma(E_\gamma)}\left(\frac{1}{e^{-\lambda_X t_d}(1-e^{-\lambda_X t_c})(1-e^{-\lambda_X t_{irr}})}\right) \tag{7}$$

Equations (1), (2) and (7) as are strictly valid for independently produced residual radionuclides that are produced directly by the spallation reaction. However, this is true in very few cases. For the majority of the residuals measured, the production cross section is a cumulative cross section of several residual precursors that decay via β^-, β^+,

$EC-$, or $\alpha-decay$ into the residual of concern and includes the direct production of the residual.

The production cross section for a residual is considered independent if that radionuclide of concern is produced directly via the spallation event and not from radioactive decay of other residual precursors. The independent cross section can be obtained if:

- If the residual of concern is shielded by stable nuclides against β^- ,or β^+ decay or the precursor is a long-lived radioisotope in comparison to the time scale of the gamma spectrum measurement.
- Otherwise if the production cross section of the precursor radioisotope has been measured then the independent production cross section of the residual can be calculated by decay correction.

If neither of these two cases are true, the production cross section calculated is considered cumulative. Table B.1 in Appendix B shows the chain of the precursors for each cumulative radionuclide as well as the fraction of the contribution to the cumulative radionuclide from each precursor.

3.3 Corrections for radioactive progenitors

In the case where all of the radioactive progenitors have a short half-life compared to the decay time between the irradiation and the start of the gamma spectrum measurement, it can be assumed that they have completely decayed to the spallation residual being measured, then Equation (6) holds true for a cumulative production cross section. This is the case for most of the radioisotopes measured in this work.

However there are two cases where the mother and daughter radioisotopes measured have similar half-lives. These cases are ^{88}Zr (T1/2=83.4 days) decaying to ^{88}Y (T1/2=106.6 days) and ^{95}Zr (T1/2=64 days) decaying to ^{95}Nb (T1/2 34.97 days). In these

cases where the mother radionuclide *m* decays to the daughter product *d* then the use of the Equations 1 through 6 give the incorrect activity of the daughter at the end of the irradiation. This incorrect activity shall be denoted as $A_d^*(0)$. The true activity of the daughter product $A_d(0)$ can be found knowing the activity of the mother nuclide $A_m(0)$. Then the true activity of the daughter product $A_d(0)$ can be calculated by Equation (8)

$$A_d(0) = A_d^*(0) + A_m(0)\frac{\lambda_d}{\lambda_d - \lambda_m}\left(1 - e^{-(\lambda_m - \lambda_d)t_d}\right)\frac{\lambda_d}{\lambda_m}\left(\frac{1 - e^{-\lambda_m t_c}}{1 - e^{-\lambda_d t_c}}\right) \quad (8)$$

Another case were the independent cross section can be found for a mother/daughter decay chain is in the case were the cumulative production cross sections for both the mother and daughter are known. If this is the case and the half-life of the mother radioisotope is short compared to the half-life of the daughter, then for large decay times the independent cross section for the daughter residual can be calculated using the following.

$$\sigma_{d,cum} = \sigma_d + \sigma_m\left(\frac{\lambda_m}{\lambda_m - \lambda_d}\right) \quad (9)$$

3.4 Proton flux measurement

The $^{27}Al(p,x)^{22}Na$ reaction was used to measure the proton flux via aluminum foils that were irradiated along with the mercury targets. The resulting ^{22}Na (T1/2 = 2.6027 yr.) radionuclide emits a 1,274 keV photon that was measured via gamma-ray spectroscopy. The Goodfellow Cooperation manufactured the aluminum foils used in the measurement of the proton flux. The high purity (99.0%) aluminum foils measuring 50mm x 50mm by 0.010mm thick were weighed prior the experiment to determine the total number of target atoms N_{Al} in each foil (Table 1). The thickness of the foils was chosen as to minimize the proton energy loss through the foils while allowing for sufficient reactions to take place to

measure the proton flux. A stack of three foils was placed on the entrance and exit window of the mercury target. In order to determine the proton flux only the middle foil of the foil stack at the entrance window was analyzed. This method assumes that the recoil loss of any ^{22}Na atoms from the middle foil will be balanced by a recoil gain from the first foil in the stack.

Table 1: Mass of Aluminum Foils

Foil #	Mass (mg)	Foil #	Mass (mg)
Al-1	61.3 ± 0.1	Al-10	62.6 ± 0.1
Al-2	61.5 ± 0.1	Al-11	62.2 ± 0.1
Al-3	61.9 ± 0.1	Al-12	64.3 ± 0.1
Al-4	61.2 ± 0.1	Al-13	63.3 ± 0.1
Al-5	62.3 ± 0.1	Al-14	62.4 ± 0.1
Al-6	62.4 ± 0.1	Al-15	62.6 ± 0.1
Al-7	64.2 ± 0.1	Al-16	62.7 ± 0.1
Al-8	62.0 ± 0.1	Al-17	63.9 ± 0.1
Al-9	63.1 ± 0.1	Al-18	62.5 ± 0.1

Equation (6) from the previous section can be rearranged and used to determine the proton flux given that a production cross section for the $^{27}Al(p,x)^{22}Na$ is known.

Seven measurements of the $^{27}Al(p,x)^{22}Na$ cross section exist for 800 MeV protons (Table 2) [29-35]. The average of the seven cross section measurements is 14.3 ± 0.4 mb. This is consistent with the value measured by George Morgan et al. in 2003 of 14.3 ± 0.4 mb [30] that is the most reliable for 800 MeV. The other measurements are not as reliable for a variety of reasons, either due to how the absolute proton flux measurement was taken or due to variations of the cross sections with respect to other energies.

Table 2: Previous ^{22}Na production cross section measurements at 800 MeV

Measurement	Facility	^{22}Na Cross Section (mb)
Heydegger 1976	LAMPF	15.0 ± 1.5
Tobailem, 1981	Saclay	15.5 ± 0.9
Michel, 1995	LAMPF	15.1 ± 1.1
Vonach, 1997	LAMPF	14.2 ± 0.47
Teddeucci 1997	LAMPF	13.2 ± 0.5
Krupnyi, 2000	IHEP	12.7 ± 0.9
Morgan, 2003	LANSCE	14.3 ± 0.4

3.5 Gamma spectroscopy

Gamma spectroscopy using High Purity Germanium (HPGe) detectors was used to measure the samples after the irradiation. HPGe detectors are a semiconductor type of detector that measures the energy deposited through the interaction of gamma-rays within the detector crystal. However since gamma-rays may interact via photoelectric effect, Compton scattering, or pair production, the intrinsic efficiency of HPGe detectors varies between 10 and 100% depending on the size and geometry of the detector. With the three interactions and the typical crystal, the effects of single escape, double escape, bremsstrahlung and backscatter peaks may be seen with in the acquired spectrum along with a full energy photopeak. After the activation the gamma spectroscopy data from the mercury targets show hundreds of full energy peaks corresponding to the numerous radionuclide residuals.

Gamma spectroscopy measurements were taken with one of two different HPGe detectors. A Coaxial HPGe detector was used to take measurements shortly after irradiation at the LANSCE facility prior to the targets being sent back to Georgia Tech for further decay and analysis. The second detector used was a planar HPGe detector with a carbon fiber window for gamma-ray spectroscopy measurements at Georgia Tech. Details on these detectors and their associated setups can be found in their respective sections later in this dissertation.

To analyze the measured gamma spectra from the detectors the GENIE2000™ [36] spectroscopy software suite was used. GENIE2000™ is a modern spectroscopy software suite, with several algorithms available to select for the peak location and the peak area routines. With the complex spectra from the irradiated targets, the Library (Gamma-M) Peak Locate and the Library (Gamma-M) Peak Area algorithms were used to analyze the data. Using these two algorithms, involved creating a specialized data library for each gamma spectroscopy measurement as the targets decayed after irradiation. In all a total of eight data library sets were created for use within the GENIE2000™ software.

To create these data libraries, MCNPX and CINDER'90 were used. MCNPX was used to model the irradiation of the targets and to calculate the production cross sections for all of the spallation residuals. See Appendix E for the MCNPX input file modeling the irradiation of the target. These cross sections were the imported into CINDER90 through a custom designed activation script [10] written by F. Gallmeier and M. Wohlmuther, which calculated the approximated radioisotope inventory of the samples for the representative decay times. The most prevalent radionuclide residuals that emitted gamma-rays at these various decay periods were used to create a custom library for that data set. In general, when creating the data set any gamma-rays with energy less than ~200 keV were omitted from the data set. This is due to the significant self-shielding effect of low-energy gamma-rays within the mercury of the target. Exceptions to this practice are discussed in detail later. Additionally with numerous residuals within the sample that decay by positron emission and therefore all emit the standard 511 keV annihilation gamma-ray. This energy gamma-ray was also omitted from the data set. In Appendix A the various radionuclide residuals with corresponding half-life, gamma-ray energies, branching radio and corresponding data set(s) that measured the production cross section are listed.

The majority of the data used in calculating the production cross section was taken from photopeaks with an energy greater than 200 keV. However, seven residuals where

the production cross sections were calculated made use of data below this energy. These seven residuals were: ^{139}Ce, ^{146}Gd, ^{169}Yb, ^{182}Os, ^{188}Pt, ^{193}Au, and ^{199}Au. In the case of four of these isotopes the low energy photopeaks used had a gamma-ray abundance greater than 10% as well as other higher energy photopeaks that were used to cross check the calculated activity of each isotope.

These four isotopes were ^{169}Yb, ^{182}Os, ^{188}Pt, and ^{193}Au. The production cross section of ^{169}Yb was calculated, in data sets 4 through 7, using the 109.8, 130.5, 177.2 and 198.0 keV photopeaks with abundances of 17.5%, 11.3%, 22.2% and 35.8%, respectively. The higher energy photopeak used in the calculation of the cross section of ^{169}Yb was the 307.7 keV line. For ^{182}Os 180.2 keV photopeak, abundance of 33.5%, was used in the calculation of its production cross section in data sets 1 through 3. Higher energy photopeaks used in the ^{182}Os analysis were at the energies of 263.3, 274.3 and 510.0 keV For ^{188}Pt, the production cross section was determined in data sets 3, 4 and 5 with the 187.6 and 195.0 keV photopeaks with abundances of 19.4% and 18.6%, respectively. The 381.4, 423.3 and 478.3 keV photopeaks were used to confirm the production cross section from the two lower energy peaks in ^{188}Pt. Lastly ^{193}Au production cross section was determined in data sets 1 through 3 using the 186.2 keV photopeak with an abundance of 10.1% with comparison to the 268.2 keV photopeak.

Three residuals were measured with gamma-ray photopeaks with less than 200 keV only. The photopeaks for these isotopes had a high abundances. For the isotope ^{146}Gd, the production cross section was calculated in data sets 4 and 5 using the 114.7, 115.5, and 154.6 keV photopeaks which have abundances of 44%, 44% and 46%, respectively. In the case of ^{139}Ce and ^{199}Au the production cross sections were determined using one photopeak with energy less than 200 keV. For ^{139}Ce the determination was made using the 165.9 keV peak with an abundance of 79.9%. The decay of ^{199}Au results in two photopeaks. One at 158.4 keV with 40% abundance and the second at 208.2 keV

with an abundance of 8.72%. However the second photopeak was discarded due to interference with the 208.1 keV photopeak from the ^{170}Hf isotope with an abundance of 20%.

3.5.1 Coaxial HPGe detector

The HPGe detector used at the LANSCE facility to take the initial gamma-ray spectra of the irradiated targets was manufactured by EG&G Ortec (Model No GEM-15190-P). This detector has a 1.83 keV full width at half-maximum resolution for the 1332 keV ^{60}Co photopeak. In combination with this detector a Lynx digital signal analyzer and the GENIE2000™ software was used to collect and analyze the spectra. With the freshly irradiated targets having a moderately high level of activity, the distance between the target and detector was varied to lower the dead time of the detector to a reasonable level. The targets were placed on a nearby counter top with the detector located towards the center of the room. The centerline of the detector was 0.535 cm below the centerline of the target assembly using this setup. To lower background radiation the detector was surrounded with 10.54 cm thick lead bricks on three sides as well as on the top leaving a single open side facing the target assembly. Additionally a copper lining with a thickness of 0.81mm was placed on the same three sides and top as the lead. The target to detector distance was adjusted so that the dead time for each of the gamma spectroscopy measurements was ~10% or less. An on-site energy calibration of the detector was completed using check sources of ^{22}Na, ^{54}Mn, ^{57}Co, ^{60}Co, ^{109}Cd, ^{133}Ba, and ^{137}Cs. Figure 4 show a picture of the measurement setup at the LANSCE facility

Figure 4: Photo of LANSCE facility HPGe measurement setup, detector-to-target distance was adjusted by moving target towards the back of the table

3.5.2 Planar HPGe detector

The gamma spectroscopy data acquired at Georgia Tech after the irradiated targets had been shipped back was acquired with a Canberra HPGe detector (Model BE5030). This detector has a planar HPGe crystal underneath a thin 0.6 mm carbon fiber window. This detector has a 2.20 keV full width half-maximum resolution for the 1332 keV ^{60}Co photopeak. In combination with this detector a Lynx digital signal analyzer and the GENIE2000™ software was used to collect and analyze the data. The detector resides within a Canberra Model 747 gamma spectroscopy shield. The shield has a 20.48 cm thick layer of lead on the sides, top and bottom with a small hole in the bottom for the detector cold finger to pass through. To lower the effect of the lead x-rays the shield is lined with 0.01 cm of tin and 0.016 cm of copper. The top of the detector swings open to allow placement of the sample within the shield. Due to the size and the detector-to-target

distance needed to keep the dead times below 5% during data collection, the top of the detector shield was in the open position during data acquisition. The energy calibration of the detector was performed using a Canberra multi-gamma-ray standard (Model MGS-4) that contained ^{54}Mn, ^{57}Co, ^{65}Zn, ^{113}Sn, ^{137}Cs, and ^{155}Eu.

3.5.3 Calculation of gamma spectroscopy efficiencies

With the thickness of the mercury in the target, no suitable calibration standard could be manufactured to simulate the target geometry and the gamma-ray self-shielding effect within the mercury. Therefore, MCNP models of both the coaxial and planar HPGe detectors were used to calculate an energy efficiency curve for each of the detector-to-target geometries. For the coaxial detector, an MCNP model already existed based on the Ph.D. dissertation of Z. Wang [37]. This MCNP detector model had a measured-to-calculated efficiency difference of less than 3% to a NIST calibrated mixed gamma source measured within 5% uncertainty. This previously developed MCNP model was used to calculate the energy efficiency curves that were subsequently imported into the GENIE2000™ software. The resulting efficiency for each full energy photopeak was interpolated from the MCNP efficiency curve.

No previous MCNP model existed for the planar detector. Therefore one was developed using the detector data provided by the manufacturer. The thickness of the dead layer on the top and sides of the detector as well as the dead layer/cold finger seat on the bottom, were adjusted to make the MCNP calculated efficiencies match the five full energy peak efficiencies from the NIST traceable mixed gamma point source (Canberra Model MGS-4) within 5%. The mixed gamma point source used was calibrated by the manufacturer to within 5% of a NIST traceable standard. The five full energy peak lines used were the 86.5 keV and 105.3 keV peaks from ^{155}Eu, the 661.6 keV peak ^{137}Cs, the 834.8 keV peak from ^{54}Mn and the 1115.5 keV peak from ^{65}Zn. The match of the 5 full

energy peaks was done using five different source-to-detector geometries. These geometry setups were:

1. Point source located on the top of the detector at detector centerline.
2. Point source located at the top of the detector with an offset of 1.457 cm from detector centerline.
3. Point source located 1.66 cm from the top of the detector at detector centerline.
4. Point source located 5.08 cm from the top of the detector at detector centerline.
5. Point source located 15.24 cm from the top of the detector at detector centerline.

The final MCNP model of the detector consisted of a 0.0375 cm thick dead layer on the top and sides of the crystal and a 0.295 cm thick dead layer on the bottom/cold finger side of the crystal. A sample input file containing the final MCNP model of the detector can be found in Appendix E.

Table 3: Measured vs. Calculated efficiency of a Canberra MGS-4 multigamma-ray standard (SN 1107) for 5 detector-to-source geometries

	Top/Centerline			Top/1.457cm Offset		
Energy	Measured Efficiency	Calculated Efficiency	% Difference	Measured Efficiency	Calculated Efficiency	% Difference
86.5	3.38E-01	2.92E-01	-15.9	3.23E-01	2.86E-01	-12.8
105.3	3.40E-01	3.17E-01	-7.3	3.23E-01	3.09E-01	-4.7
661.6	8.30E-02	8.22E-02	-1.0	7.53E-02	7.64E-02	1.5
834.8	6.60E-02	6.65E-02	0.7	6.00E-02	6.18E-02	2.9
1115.5	5.09E-02	5.14E-02	0.9	4.55E-02	4.77E-02	4.5

	1.66 cm/Centerline			5.08 cm/Centerline		
Energy	Measured Efficiency	Calculated Efficiency	% Difference	Measured Efficiency	Calculated Efficiency	% Difference
86.5	1.99E-01	1.91E-01	-4.6	6.58E-02	6.44E-02	-2.2
105.3	1.96E-01	1.96E-01	0.3	6.38E-02	6.51E-02	1.9
661.6	4.02E-02	4.00E-02	-0.4	1.27E-02	1.23E-02	-3.0
834.8	3.14E-02	3.20E-02	2.1	9.94E-03	9.80E-03	-1.4
1115.5	2.38E-02	2.44E-02	2.5	7.52E-03	7.44E-03	-1.0

	15.24 cm/Centerline		
Energy	Measured Efficiency	Calculated Efficiency	% Difference
86.5	1.24E-02	1.22E-02	-1.9
105.3	1.23E-02	1.25E-02	1.4
661.6	2.55E-03	2.46E-03	-3.7
834.8	1.99E-03	1.96E-03	-1.9
1115.5	1.52E-03	1.49E-03	-2.2

While it is noted that differences greater than 5% exist between the measured and calculated efficiencies, these data points represent lower energy full energy peaks that were generally not used in the determination of the spallation residual production cross sections. Furthermore these data points were for a point source located on the top of the detector. The 1.66, 5.08 and 15.24 cm detector-to-source geometries were a close match to the actual detector-to-target distances for the gamma spectroscopy data measured from the irradiated targets. For these three geometries the difference between measured and

calculated efficiencies is less than 5% for all full energy photopeaks. Typically this difference is between 2-3%, however a detector model efficiency error of 5% was used in the error calculation for the production cross sections. As with the MCNP model for the coaxial HPGe detector the MCNP model for the planar HPGe detector was used to calculate the energy efficiency curves that were subsequently imported into the GENIE2000™ software. The resulting efficiency for each full energy data peak was interpolated from the MCNP efficiency curve. The MCNP calculated gamma-ray efficiency curves for each geometry setup are given in Appendix D.

3.6 Uncertainty in measurements

The following sources of uncertainty were taken into account and the final uncertainty of the proton flux measurement and the production cross sections were calculated using the laws of the error propagation. Each source of uncertainty is discussed in detail below. For the measurement of the proton flux the uncertainties for the following parameters were used in the calculation of the final uncertainty; the mass of the aluminum monitoring foil, the gamma spectroscopy efficiency, the net peak area under the full energy peak of the ^{22}Na isotope, and the production cross section of the $^{27}Al(p,x)^{22}Na$ reaction. For the measurement of the residual production cross section uncertainties for the following parameters were used in the calculation of the final uncertainty, the proton flux, the target mass, gamma spectroscopy efficiency, net peak area under the full energy peaks of each isotope, the half-lives, and the γ - abundances.

3.6.1 Uncertainty in determination of net peak area

The uncertainty in the net peak area of full energy peaks in the gamma spectrum was calculated using the GENIE2000™ software algorithm used to determine the peak area.

As indicated before the Library (Gamma-M) peak area algorithm was used in the analysis of the collected gamma spectra.

3.6.2 Uncertainty of half-lives

The half-lives of the isotopes for which the production cross sections were measured were taken from the nuclear wallet card [38] published by the National Nuclear Data Center, part of the Brookhaven National Laboratory. While uncertainties in the individual isotopes are given as part of the data, the individual uncertainties were not used in the calculation of the final uncertainty of the production cross section. Instead a typical uncertainty of 1% was used as has been used in previous publications measuring production cross sections [39].

3.6.3 Uncertainty of γ - abundances

For the data sets the majority of the abundance of gamma-rays and their associated energies was imported into the radionuclide library using the Canberra NuChart software. The nuclear data in the software was taken from the 1997 release of NUDAT [40] from the National Nuclear Data Center. In the case the data was not available in the software, the nuclear data was taken from the ICRP publication 107 [41] data and imported by hand into the radionuclide library. As with the case of the isotope half-lives, the individual uncertainties in the abundance data were not used. Instead a global uncertainty of 2% was used consistent with previous publications [39].

3.6.4 Uncertainty in gamma spectroscopy efficiency

As detailed earlier a MCNP model was developed for each of the two HPGe detectors used in taking the gamma spectroscopy data. For the coaxial detector the MCNP model was within 3% error of a measured NIST traceable source that was measured to within a 5% error. For the planar detector the MCNP model was within 5% error of a measured

NIST traceable source measured to within a 5% error. For both detectors the MCNP models were used to calculate the efficiency of the detector to specific energy gamma-rays. A total of 67 different energies were used to calculate the detector efficiency for each of the data measurement setup geometries. Appendix D shows the specific gamma spectroscopy energy efficiency curves for each setup. The GENIE2000™ software was programed with these energy efficiency curves and interpolated between data points for the specific efficiency of full energy peaks in the measured data. For each data point on the efficiency curves the MCNP calculations were continued until an error of less than 0.2% was reported. Using the laws of error propagation the gamma spectroscopy efficiency error for data taken with the coaxial detector was 5.83%. For data taken with the planar HPGe detector the gamma spectroscopy efficiency error was 7.07%.

3.6.5 Uncertainty in time

For the time scales of the irradiation, decay and counting of the samples in comparison with the half-lives of the radionuclides measured, it was assumed that uncertainties in the measurement of the irradiation, decay and counting times were negligible.

3.6.6 Uncertainty in target/foil mass

The mass of the individual aluminum foils used for the proton flux measurement were taken using a Scientech SA-120 Analytical Balance (SN 8617). The SA-120 is capable of measuring the sample mass to within 0.1 ± 0.1 mg. Prior to the foil measurement the balance was calibrated using a set of NIST traceable weights.

The mass of the targets was measured at ORNL after they were filled with mercury and were reported with an accuracy of 0.1 g. Without having specific information on the balance used to measure the mass of the targets it was assumed that the balance used was within ±0.5 g. With the total mass of the mercury being approximately 750 g in each

target the uncertainty in the measurement of the mercury mass was only a fraction of a percent.

3.6.7 Uncertainty in proton flux density

Using laws of error propagation the uncertainty in the proton flux density was calculated by using the uncertainty in the mass of the aluminum monitoring foil, the uncertainty in the gamma spectroscopy efficiency, the uncertainty in the net peak area under the full energy peak of the ^{22}Na isotope, and the uncertainty of the production cross section of the $^{27}Al(p,x)^{22}Na$ reaction. Small fluctuations in the beam intensity were not considered due to the short irradiation period in comparison with the decay times for the irradiated samples and the half-lives of the isotopes measured.

3.6.8 Dead time and pile-up losses in gamma spectroscopy

By varying the sample to detector distance of the various data measurements the dead time of the measurement was ~10% or less for each gamma spectroscopy measurement at LANSCE and ~5% or less for each gamma spectroscopy measurement at Georgia Tech. The internal correction in the Lynx digital signal analyzer was used to correct for these losses.

3.6.9 Self-absorption of gamma-rays in the sample

Self-absorption of gamma-rays in the mercury sample were considered as part of the MCNP calculation that determined the individual gamma spectroscopy efficiency curves for each of the data measurement geometry. No further corrections on self-absorption in the sample were taken into consideration.

CHAPTER 4: EXPERIMENTS

4.1 Irradiation at LANSCE

Three irradiations were performed at the LANSCE complex in the blue room of the Weapon Neutron Research (WNR) facility (Figures 5 and 6). All three irradiations were performed with 800 MeV protons with a beam spot of ~0.5 cm radius, one irradiation on the empty target assembly and one per each mercury filled target labeled Hg-1 and Hg-2. The centerline of each target in the 3.175 cm radius window was aligned with the beam line. Stacks of three Aluminum foils (5 cm x 5 cm) were placed on beam centerline over the entry window of the target and behind the exit window of the target. The target assembly was located in a polyethylene container present as a secondary containment. The container/target were placed on top of a wooden top table used to hold its position. On the entry side of the room, a row of lead bricks was placed ~10 cm away from the side of the container and parallel to the beam line. These lead bricks acted as a shadow shield so entry could be made soon after irradiation to switch the targets and progress with the irradiations in short order. As the irradiations took place at the beginning of the summer-fall 2011 irradiation campaign they were sole use with Target 4 acting as the beam stop instead of being used for neutron production.

The irradiations took place during June 16th and 17th of 2011. The first irradiation was of the empty target and started at 21:25 and was initially planned to continue for a total of 18 minutes at an approximate beam current of 55 nA. During this irradiation however the operations lost the beam and the irradiation was stopped after 9 minutes and 33 seconds at 21:34. The beam was restarted at 21:44 and continued on for a total of 9 more minutes ending the irradiation at 21:53 for a total irradiation time of 18 minutes and 33 seconds.

Figure 5: WNR Blue room setup for irradiation of targets. Protons enter from left

Figure 6: Close up of irradiation setup looking at the entry window of the target

The mercury filled target Hg-1 was the second irradiation completed. The irradiation of Hg-1 was started at 23:58 on June 16th and ended at 00:16 on June 17th after a total of 18 minutes. Using the WNR beam current instruments the average current for this

irradiation was ~51.2 nA. The irradiation of mercury filled target Hg-2 commenced at 1:41 on June 17th and ended at 1:59 after and irradiation of 18 minutes. The average current using the WNR instruments during the irradiation of target Hg-2 was ~50.9 nA

4.2 Gamma spectroscopy measurements

Prior to the irradiation of the targets the coaxial HPGe detector was setup and an energy calibration performed in the location provided at LANSCE. A background measurement was completed after setup and calibration. After the irradiation of the samples, they were allowed to decay until the morning of June 17th before being removed from the blue room. After removal they were taken to the location of the HPGe detector for gamma spectroscopy measurements. Prior to starting the first measurement on each irradiated target, the aluminum foil stacks were removed and gamma spectroscopy measurements were completed on the individual foils while the targets were allowed to decay for additional time.

4.2.1 Measurements at LANSCE

The first measurement of the irradiated targets was taken approximately 18 hours after the irradiation. For all three targets, one empty and the two filled targets, gamma spectroscopy measurements of 30 minutes and 120 minutes were performed. The distance from the target front window to the side surface of the coaxial HPGe detector was 168.99 cm for these two measurements. A third measurement of each of the three targets was acquired on June 18th after approximately 36 hours of decay. For the third measurement, the sample to detector distance was shortened due to the lower activity of the samples. The distance from the target front window to the side surface of the detector was 128.99 cm for the third set of measurements. For each of the third set of gamma spectroscopy measurements the live time of the data acquisition was 60 minutes.

Initially the next set of gamma spectroscopy measurements was planned at LANSCE approximately 2 weeks after the irradiation. However, due to the proximity of the Los Conchas Fire, the LANSCE facility closed from June 27th to July 6th. Therefore, the next sets of gamma spectroscopy measurements occurred approximately 30 days after the irradiation. The fourth and fifth sets of gamma spectroscopy measurements occurred on July 19th and July 20th after the LANSCE facility reopened. Prior to these measurements an energy calibration was once again performed on the coaxial HPGe detector. The live time of these measurements was 120 minutes and 90 minutes, respectively. With lower activity the distance for the fourth and fifth measurements was shortened to 31.20 cm from the front window surface to the side of the coaxial HPGe detector. This resulted in a detector dead time below 5% while allowing a higher detection efficiency.

4.2.2 Measurements at Georgia Tech

After the fourth and fifth set of gamma spectroscopy measurements, the irradiated targets were shipped to Georgia Tech for further decay and analysis of the residual isotopes. All the remaining measurements of the targets were collected with the planar HPGe detector described in section 3.5.2. For each data set an energy calibration was performed prior to taking the background and gamma spectroscopy measurement of each of the three targets. The sixth, seventh and eight gamma spectroscopy counts were stared taken in November 2011, February 2012 and June 2012 respectively. For the sixth and seventh measurements the distance between the front target window to the detector carbon fiber window was 20.15 cm and for the eight measurement this distance was 3.33 cm. Table 4 shows the date and time the spectroscopy count was started for each of the two mercury filled targets. The table also shows the gamma spectroscopy live time as well as the decay time for each data set.

Table 4: Gamma spectroscopy count data for filled mercury targets Hg-1 and Hg-2

Data Set	Target	Spectroscopy Count Date and Time	Live Time (s)	Decay Time (days)	MCNP Efficiency Calculation Geometry (#)
1	Hg-1	6/17/11 18:42	1800	0.70	1
2	Hg-1	6/17/11 19:17	7200	0.72	1
3	Hg-1	6/18/11 13:38	3600	1.49	2
4	Hg-1	7/19/11 14:39	7200	32.53	3
5	Hg-1	7/20/11 11:28	5400	33.40	3
6	Hg-1	10/6/11 11:13	7200	111.39	4
7	Hg-1	2/28/12 9:21	86400	256.31	4
8	Hg-1	6/18/12 9:02	86400	367.29	5
1	Hg-2	6/17/11 21:34	1800	0.75	1
2	Hg-2	6/17/11 22:08	7200	0.77	1
3	Hg-2	6/18/11 14:49	3600	1.46	2
4	Hg-2	7/19/11 16:42	7200	32.54	3
5	Hg-2	7/20/11 13:11	5400	33.40	3
6	Hg-2	10/6/11 17:04	7200	111.56	4
7	Hg-2	3/2/12 14:34	86400	259.45	4
8	Hg-2	6/25/12 7:30	82408.22	374.16	5

4.2.3 Measurements of emptied targets and collected mercury

After the eighth data set was taken the filled targets were shipped to ORNL to be emptied into a small vial and a larger bottle. For the Hg-1 target the small vial contained 6.3258g of mercury and the small vial for the Hg-2 target contained 6.5329g of mercury. The larger bottles contained 38.4972g and 39.7223g of mercury for the Hg-1 target and the Hg-2 target, respectively. The two vials and two bottles along with the empty targets were shipped back to Georgia Tech for further gamma spectroscopy analysis. The vials and bottles were counted between December 2012 and February 2013. For the small vial of mercury taken from target Hg-1, the gamma spectroscopy count for a total live time of 172,800 seconds was started after 553.63 days of decay. The count for the vial

of mercury taken from Hg-2 incorporating the same live time was started after 556.21 days of decay. For the large bottles of the irradiated mercury, gamma spectroscopy counts with a live time of 86,400 seconds were taken after 580.30 days and 606.29 days for targets Hg-1 and Hg-2, respectively. After these data were taken the empty Hg-1 target was disassembled and gamma spectroscopy counts were taken of the front window component of target Hg-1 to analyze the residue that was left in the empty target. To fix the residue to the front window a thin layer of adhesive film was placed over the side facing the mercury cavity. Following this count the adhesive film was removed from the front window and the film was counted on the planar HPGe detector. Both these counts were for a live time of 86,400 seconds occurring at 587.26 days decay for the front window component and 588.30 days of decay for the adhesive film.

Neither the data from the vials, bottles, or the individual components were suitable to contribute to the production cross section calculations. However these data are discussed in the conclusion section as information to identify individual radioisotopes that mix uniformly within the mercury after irradiation and other isotopes that can plate out on the stainless steel surfaces of the piping and valve structures in accelerators with mercury target systems. In order to analyze the data from the gamma spectroscopy measurements of the vials and bottles, a MCNP gamma-ray efficiency curve was calculated for each of the data sets. These calculated efficiency curves are MCNP efficiency calculation geometry numbers 6 and 7 for the small vial and large bottle, respectively. For the data collected for the front window component and the adhesive film only an energy calibration was performed on the HPGe detector. No efficiency calibration curves were developed for these data sets since the two counts were taken in an identical geometry setup and the data reported are ratios of the full energy photo peaks.

CHAPTER 5: RESULTS

5.1 Proton current measurement

The proton current was measured through the gamma spectroscopy analysis of the activated aluminum foils that were mounted to the front window of targets Hg-1 and Hg-2. Within the stack of three foils the center foil was used in the determination of the proton current. The proton current was determined with two gamma spectroscopy counts with the planar HPGe detector. The first count was in September 2011 with a live time of 48 hr. The second count was in June 2012 with a live time of 72 hr. The average proton current for Hg-1 was 50.5 ± 2.7 nA. For Hg-2 the average proton current was 47.1 ± 2.6 nA. The average proton current measured by the gamma spectroscopy analysis agrees closely with the LANSCE measured proton beam current of 51.2 nA and 50.9 nA for the irradiation of Hg-1 and Hg-2, respectively.

5.2 Spallation residual production cross sections

The production cross sections of 53 residual radioisotopes were measured from the irradiation of the mercury filled targets. The results were acquired via either the coaxial HPGe detector or the planar HPGe detector measurement discussed previously.

The half-lives of the residuals analyzed range from approximately 5 hours for ^{192}Au (4.94 hr.) to approximately 2.75 years for ^{125}Sb (2.7586 yr.). Because of the decay time needed after irradiation to be able to handle, move and set up the targets for analysis with the coaxial HPGe detector, residual isotopes with half-lives less than ~5 hours were not analyzed as part of this work. In general, due the thickness of the target, isotopes with only gamma-rays with emission energies below 200 keV were not considered except for

the seven radioisotopes: ^{139}Ce, ^{146}Gd, ^{169}Yb, ^{182}Os, ^{188}Pt, ^{193}Au and ^{199}Au that have been previously discussed.

A total of eight gamma-ray spectroscopy counts were acquired for each target. These counts ranged from a decay period of a few hours to just over a year. Production cross sections were determined for each of the gamma-ray full energy photopeaks for the most prominent residuals. Residuals with more than one full energy photopeak were averaged to obtain the production cross section for that data set. For many isotopes the cross sections were determined from more than one data set and an average production cross section was determined along with a maximum uncertainty from the multiple data points.

In the analysis of the data to determine the production cross section the following three criteria were used.

1. The decay time between the irradiation and the start of the data acquisition must be less than 5 half-lives of the residual being analyzed for the production cross section to be determined
2. No other residual radionuclides contained gamma-ray emission energies that contaminated the gamma-ray emission energies of the residual of interest. Two sources of this contamination were considered, the first from other spallation residuals in the mercury the second was from radioisotopes created in the stainless steel encapsulation of the target. Gamma-ray spectroscopy data from the empty irradiated target taken at approximately the same decay time was used to determine these potential contamination peaks.
3. In the case where an isotope with a gamma-ray emission line may contaminate the one being analyzed, the decay time between the irradiation and the start of the data acquisition must be greater than five half-lives for the contaminating isotope before using the photopeak in determining the production cross section for the residual of interest.

Tables 5 and 6 give the production cross section results for the residual radionuclides measured. Results shown in italics are measured individual production cross sections for those residuals. All other results are a cumulative production cross sections. Table 7 presents the resulting average measured production cross section result for all data sets and the corresponding MCNPX calculated production cross section using the Bertini model. Also show in Table 7 is the resulting calculated-over-measured (C/M) ratio for each of the 53 residual isotopes analyzed. The results for individual production cross section residuals are shown in italics in Table 7 as previously done in Table 5 and 6.

Table 5: Radioisotope production cross section measurements for mercury targets irradiated at 800 MeV (Data Sets 1-4)

Isotope	Half-life	Target	Data Set 1 (mb)	Data Set 2 (mb)	Data Set 3 (mb)	Data Set 4 (mb)
^{147}Eu	24.1 d	Hg-1	-	-	-	3.1 ± 0.4
		Hg-2	-	-	-	2.8 ± 0.4
^{146}Gd	48.27 d	Hg-1	-	-	-	15.5 ± 3.7
		Hg-2	-	-	-	18.0 ± 6.3
^{149}Gd	9.28 d	Hg-1	-	-	-	3.6 ± 0.6
		Hg-2	-	-	-	2.9 ± 0.5
^{160}Ho/ ^{160}Er	25.6 m / 28.58 h	Hg-1	-	-	13.3 ± 1.4	-
		Hg-2	-	-	14.4 ± 1.5	-
^{165}Tm	30.06 h	Hg-1	-	-	23.0 ± 2.4	-
		Hg-2	-	-	23.0 ± 1.5	-
^{166}Tm/ ^{166}Yb	7.70 h	Hg-1	-	-	43.8 ± 4.5	-
		Hg-2	-	-	42.3 ± 4.4	-
^{167}Tm	9.25 h	Hg-1	-	-	-	90.1 ± 9.4
		Hg-2	-	-	-	78.4 ± 8.2
^{169}Yb	32.018 d	Hg-1	-	-	-	68.6 ± 6.9
		Hg-2	-	-	-	65.4 ± 6.6
^{169}Lu	34.06 h	Hg-1	-	-	20.7 ± 2.5	-
		Hg-2	-	-	23.6 ± 2.8	-

Table 5: (Continued)

Isotope	Half-life	Target	Data Set 1 (mb)	Data Set 2 (mb)	Data Set 3 (mb)	Data Set 4 (mb)
^{171}Lu	8.24 d	Hg-1	-	-	-	32.7 ± 3.3
		Hg-2	-	-	-	35.4 ± 3.6
^{172}Lu	6.7 d	Hg-1	-	-	-	26.3 ± 2.6
		Hg-2	-	-	-	29.0 ± 2.9
^{173}Lu	1.37 y	Hg-1	-	-	-	100.4 ± 11.7
		Hg-2	-	-	-	92.4 ± 10.9
^{170}Hf	16.01 h	Hg-1	-	-	31.1 ± 3.2	-
		Hg-2	-	-	34.3 ± 3.5	-
^{173}Hf	23.6 h	Hg-1	-	-	73.4 ± 7.8	-
		Hg-2	-	-	86.2 ± 8.9	-
^{175}Hf	70 d	Hg-1	-	-	-	72.1 ± 7.4
		Hg-2	-	-	-	73.8 ± 7.6
^{175}Ta	10.5 h	Hg-1	-	-	43.6 ± 4.7	-
		Hg-2	-	-	46.2 ± 5.2	-
^{176}Ta	8.09 h	Hg-1	39.1 ± 3.9	43.2 ± 4.3	39.3 ± 4.0	-
		Hg-2	41.2 ± 4.1	44.6 ± 4.4	42.5 ± 4.3	-
^{181}Re	19.9 h	Hg-1	50.1 ± 5.1	50.7 ± 5.1	55.4 ± 5.6	-
		Hg-2	51.8 ± 5.2	59.3 ± 6.0	59.8 ± 6.0	-
^{182}Os	22.1 h	Hg-1	120.0 ± 12.8	144.5 ± 15.2	102.9 ± 10.8	-
		Hg-2	142.5 ± 15.0	139.9 ± 14.5	100.7 ± 10.6	-
^{183}Os	13.0h	Hg-1	32.5 ± 3.4	36.5 ± 3.9	43.7 ± 4.5	-
		Hg-2	34.9 ± 3.7	37.8 ± 4.0	47.5 ± 4.9	-
^{185}Os	93.6 d	Hg-1	-	-	-	58.1 ± 5.9
		Hg-2	-	-	-	62.1 ± 6.4
^{186}Ir	16.64 h	Hg-1	29.9 ± 3.0	26.8 ± 2.7	30.3 ± 3.1	-
		Hg-2	36.6 ± 3.7	26.4 ± 2.7	32.3 ± 3.3	-
^{187}Ir	10.5 h	Hg-1	66.6 ± 6.8	70.6 ± 7.1	74.6 ± 7.8	-
		Hg-2	71.6 ± 7.3	71.7 ± 7.2	79.9 ± 8.3	-
^{189}Ir	13.2 d	Hg-1	-	-	-	186.9 ± 27.1
		Hg-2	-	-	-	173.1 ± 25.2
^{190}Ir	*11.78 d*	*Hg-1*	-	-	-	*2.5 ± 0.3*
		Hg-2	-	-	-	*2.6 ± 0.3*
^{188}Pt	10.2 d	Hg-1	-	-	75.2 ± 12.0	103.3 ± 10.4
		Hg-2	-	-	102.5 ± 13.0	112.8 ± 11.4

Table 5: (Continued)

Isotope	Half-life	Target	Data Set 1 (mb)	Data Set 2 (mb)	Data Set 3 (mb)	Data Set 4 (mb)
^{189}Pt	10.87 h	Hg-1	67.6 ± 6.9	74.7 ± 7.6	75.5 ± 7.7	-
		Hg-2	74.3 ± 7.6	78.9 ± 8.0	82.2 ± 8.4	-
^{191}Pt	2.862 d	Hg-1	-	-	71.0 ± 7.3	-
		Hg-2	-	-	79.9 ± 8.2	-
^{192}Au	4.94 h	Hg-1	108.2 ± 11.6	121.8 ± 13.1	-	-
		Hg-2	119.7 ± 12.0	131.4 ± 14.1	-	-
^{193}Au	17.65 h	Hg-1	81.2 ± 13.1	87.2 ± 13.4	65.4 ± 9.4	-
		Hg-2	74.1 ± 12.6	79.8 ± 12.4	80.9 ± 11.5	-
^{194}Au	38.02 h	Hg-1	32.6 ± 3.4	33.9 ± 3.5	24.3 ± 2.6	-
		Hg-2	34.4 ± 3.6	34.6 ± 3.5	23.3 ± 2.6	-
^{196}Au	*6.1669 d*	*Hg-1*	-	-	*22.5 ± 2.4*	-
		Hg-2	-	-	*21.3 ± 2.4*	-
^{198}Au	*2.6956 d*	*Hg-1*	-	-	*23.8 ± 2.5*	-
		Hg-2	-	-	*23.6 ± 2.5*	-
^{199}Au	*3.139 d*	*Hg-1*	-	-	*63.4 ± 10.7*	-
		Hg-2	-	-	*62.6 ± 11.5*	-
^{193m}Hg	*11.8 h*	*Hg-1*	-	-	*25.4 ± 2.7*	-
		Hg-2	-	-	*25.9 ± 2.7*	-
^{195}Hg	10.53 h	Hg-1	48.7 ± 6.4	49.0 ± 5.4	55.2 ± 7.0	-
		Hg-2	39.5 ± 5.1	58.7 ± 6.3	63.2 ± 7.4	-
^{197m}Hg	23.8 h	Hg-1	-	-	59.1 ± 9.9	-
		Hg-2	-	-	57.8 ± 9.8	-
^{200}Tl	*26.1 h*	*Hg-1*	-	-	*8.9 ± 0.9*	-
		Hg-2	-	-	*8.9 ± 0.9*	-
^{202}Tl	*12.23 d*	*Hg-1*	-	-	-	*1.8 ± 0.2*
		Hg-2	-	-	-	*1.7 ± 0.2*

Table 6: Radioisotope production cross section measurements for mercury targets irradiated at 800 MeV (Data Sets 5-8)

Isotope	Half-life	Target	Data Set 5 (mb)	Data Set 6 (mb)	Data Set 7 (mb)	Data Set 8 (mb)
^{75}Se	119.779 d	Hg-1	-	3.2 ± 0.4	3.1 ± 0.3	5.2 ± 0.6
		Hg-2	-	2.1 ± 0.2	4.0 ± 0.4	5.1 ± 0.5
^{83}Rb	86.2 d	Hg-1	-	2.8 ± 0.3	2.5 ± 0.3	3.8 ± 0.4
		Hg-2	-	4.0 ± 0.4	3.3 ± 0.4	3.5 ± 0.4
^{88}Y	*106.61d*	*Hg-1*	-	*1.9 ± 0.2*	*1.1 ± 0.1*	*1.0 ± 0.1*
		Hg-2	-	*1.9 ± 0.2*	*1.7 ± 0.2*	*0.7 ± 0.1*
^{88}Zr	83.4 d	Hg-1	-	1.8 ± 0.2	1.1 ± 0.1	1.6 ± 0.2
		Hg-2	-	1.9 ± 0.2	1.5 ± 0.2	1.5 ± 0.2
^{95}Zr	64.032 d	Hg-1	-	1.2 ± 0.1	1.0 ± 0.1	1.3 ± 0.1
		Hg-2	-	1.3 ± 0.1	1.5 ± 0.2	1.3 ± 0.2
^{95}Nb	*34.991 d*	*Hg-1*	-	*2.8 ± 0.3*	*1.6 ± 0.2*	-
		Hg-2	-	*2.6 ± 0.3*	*1.5 ± 0.2*	-
^{102}Rh	207 d	Hg-1	-	-	1.1 ± 0.1	1.9 ± 0.2
		Hg-2	-	-	-	1.8 ± 0.2
^{110m}Ag	*249.76 d*	*Hg-1*	-	-	-	*0.7 ± 0.1*
		Hg-2	-	-	-	*0.7 ± 0.1*
^{125}Sb	2.7586 y	Hg-1	-	-	-	2.2 ± 0.2
		Hg-2	-	-	-	3.7 ± 0.4
^{139}Ce	137.64 d	Hg-1	-	-	2.3 ± 0.3	3.7 ± 0.4
		Hg-2	-	-	3.4 ± 0.4	3.9 ± 0.4
^{143}Pm	265 d	Hg-1	-	-	0.4 ± 0.1	0.6 ± 0.1
		Hg-2	-	-	0.6 ± 0.1	0.5 ± 0.1
^{147}Eu	24.1 d	Hg-1	2.8 ± 0.4	-	-	-
		Hg-2	3.4 ± 0.5	-	-	-
^{149}Eu	93.1 d	Hg-1	-	-	-	-
		Hg-2	-	-	6.8 ± 1.2	-
^{146}Gd	48.27 d	Hg-1	16.7 ± 5.4	-	-	-
		Hg-2	18.8 ± 3.6	-	-	-
^{167}Tm	9.25 h	Hg-1	94.8 ± 9.9	-	-	-
		Hg-2	87.1 ± 9.1	-	-	-
^{169}Yb	32.018 d	Hg-1	73.2 ± 7.4	57.7 ± 6.3	-	-
		Hg-2	74.0 ± 7.5	64.6 ± 7.0	-	-

Table 6: (Continued)

Isotope	Half-life	Target	Data Set 5 (mb)	Data Set 6 (mb)	Data Set 7 (mb)	Data Set 8 (mb)
^{171}Lu	8.24 d	Hg-1	34.1 ± 3.5	-	-	-
		Hg-2	37.4 ± 3.8	-	-	-
^{172}Lu	6.7 d	Hg-1	27.9 ± 2.0	37.2 ± 4.0	34.8 ± 3.7	45.1 ± 4.8
		Hg-2	29.9 ± 3.0	41.4 ± 4.4	47.1 ± 5.0	46.6 ± 5.0
^{173}Lu	1.37 y	Hg-1	87.4 ± 10.9	108.3 ± 11.7	97.9 ± 10.5	104.7 ± 11.2
		Hg-2	90.6 ± 11.4	122.8 ± 13.3	96.1 ± 10.3	103.2 ± 11.1
^{175}Hf	70 d	Hg-1	74.9 ± 7.8	91.1 ± 9.7	76.4 ± 8.2	112.5 ± 12.1
		Hg-2	80.7 ± 8.3	99.0 ± 10.6	101.9 ± 11.0	108.1 ± 11.7
^{178}Ta / ^{178}W	2.36 h	Hg-1	-	32.0 ± 4.3	-	-
		Hg-2	-	36.0 ± 4.7	-	-
^{185}Os	93.6 d	Hg-1	59.8 ± 6.0	77.5 ± 8.3	60.4 ± 6.5	83.1 ± 8.9
		Hg-2	65.3 ± 6.6	83.2 ± 8.9	79.1 ± 8.5	77.6 ± 8.3
^{189}Ir	13.2 d	Hg-1	207.4 ± 30.1	-	-	-
		Hg-2	193.3 ± 28.2	-	-	-
^{190}Ir	*11.78 d*	*Hg-1*	*2.5 ± 0.3*	-	-	-
		Hg-2	*2.6 ± 0.3*	-	-	-
^{192}Ir	*73.827 d*	*Hg-1*	-	*1.8 ± 0.4*	*1.8 ± 0.2*	*2.6 ± 0.2*
		Hg-2	-	*2.0 ± 0.2*	*2.5 ± 0.2*	*2.4 ± 0.2*
^{188}Pt	10.2 d	Hg-1	115.0 ± 11.6	-	-	-
		Hg-2	123.9 ± 12.5	-	-	-
^{202}Tl	*12.23 d*	*Hg-1*	*1.8 ± 0.2*	-	-	-
		Hg-2	*1.7 ± 0.2*	-	-	-

Table 7: Radioisotope production cross section measurements: Average vs. MCNPX results (All Data Sets).

Isotope	Half-life	Average (mb)	MCNPX (mb)	C/M Ratio
^{75}Se	119.779 d	3.8 ± 0.5	0.6 ± 0.04	0.16 ± 0.02
^{83}Rb	86.2 d	3.3 ± 0.4	1.0 ± 0.1	0.30 ± 0.05
^{88}Y	*106.61d*	*1.4 ± 0.2*	*0.5 ± 0.04*	*0.36 ± 0.06*
^{88}Zr	83.4 d	1.6 ± 0.2	0.6 ± 0.1	0.38 ± 0.08
^{95}Zr	64.032 d	1.3 ± 0.2	0.3 ± 0.02	0.23 ± 0.04
^{95}Nb	*34.991 d*	*2.1 ± 0.2*	*0.4 ± 0.03*	*0.19 ± 0.02*
^{102}Rh	207 d	1.6 ± 0.2	0.4 ± 0.03	0.25 ± 0.04
^{110m}Ag	*249.76 d*	*0.7 ± 0.1*	*0.1 ± 0.01*	*0.14 ± 0.02*
^{125}Sb	2.7586 y	3.0 ± 0.4	0.05 ± 0.004	0.02 ± 0.003
^{139}Ce	137.64 d	3.3 ± 0.4	1.0 ± 0.1	0.30 ± 0.05
^{143}Pm	265 d	0.5 ± 0.1	0.2 ± 0.2	0.40 ± 0.41
^{147}Eu	24.1 d	3.0 ± 0.4	2.9 ± 0.2	0.97 ± 0.15
^{149}Eu	93.1 d	6.8 ± 1.2	3.8 ± 0.3	0.56 ± 0.11
^{146}Gd	48.27 d	16.8 ± 6.3	2.4 ± 0.2	0.09 ±0.02
^{149}Gd	9.28 d	3.3 ± 0.4	3.5 ± 0.3	1.06 ± 0.16
^{160}Ho/ ^{160}Er	25.6 m / 28.58 h	13.9 ± 1.5	14.3 ± 1.1	1.03 ± 0.14
^{165}Tm	30.06 h	23.0 ± 2.5	20.2 ± 1.6	0.88 ± 0.12
^{166}Tm/^{166}Yb	7.70 h	43.1 ± 4.5	22.2 ± 1.7	0.52 ± 0.07
^{167}Tm	9.25 h	87.6 ± 9.2	23.2 ± 1.8	0.26 ± 0.03
^{169}Yb	32.018 d	67.3 ± 7.3	25.1 ± 1.9	0.37 ± 0.05

Table 7: (Continued)

Isotope	Half-life	Average (mb)	MCNPX (mb)	C/M Ratio
^{169}Lu	34.06 h	22.2 ± 2.7	24.8 ± 1.9	1.12 ± 0.16
^{171}Lu	8.24 d	34.9 ± 3.6	28.2 ± 2.2	0.81 ± 0.10
^{172}Lu	6.7 d	36.5 ± 3.9	27.6 ± 2.7	0.76 ± 0.11
^{173}Lu	1.37 y	100.4 ± 12.6	32.9 ± 3.1	0.33 ± 0.06
^{170}Hf	16.01 h	32.7 ± 3.5	24.0 ± 1.8	0.66 ± 0.08
^{173}Hf	23.6 h	79.8 ± 5.9	32.5 ± 2.5	0.41 ± 0.04
^{175}Hf	70 d	89.1 ± 12.1	34.1 ± 2.6	0.38 ± 0.06
^{175}Ta	10.5 h	44.9 ± 5.2	33.8 ± 2.6	0.75 ± 0.10
^{176}Ta	8.09 h	41.7 ± 4.4	37.3 ± 2.9	0.89 ± 0.12
^{178}Ta / ^{178}W	2.36 h	34.0 ± 4.7	37.6 ± 2.9	1.11 ± 0.18
^{181}Re	19.9 h	54.5 ± 5.5	39.8 ± 4.6	0.73 ± 0.11
^{182}Os	22.1 h	125.1 ± 13.3	39.9 ± 3.1	0.32 ± 0.04
^{183}Os	13.0h	38.8 ± 4.1	46.2 ± 3.6	1.19 ± 0.16
^{185}Os	93.6 d	70.6 ± 7.6	46.4 ± 3.6	0.66 ± 0.09
^{186}Ir	16.64 h	30.4 ± 3.1	47.8 ± 3.7	1.57 ± 0.20
^{187}Ir	10.5 h	72.5 ± 7.6	51.9 ± 4.0	0.72 ± 0.09
^{189}Ir	13.2 d	190.2 ± 13.8	55.1 ± 4.2	0.29 ± 0.03
^{190}Ir	*11.78 d*	*2.6 ± 0.3*	*2.8 ± 0.2*	*1.08 ± 0.11*
^{192}Ir	*73.827 d*	*2.2 ± 0.5*	*1.6 ± 0.1*	*0.73 ± 0.17*
^{188}Pt	10.2 d	105.5 ± 16.8	49.2 ± 3.8	0.47 ± 0.08

Table 7: (Continued)

Isotope	Half-life	Average (mb)	MCNPX (mb)	C/M Ratio
^{189}Pt	10.87 h	75.5 ± 7.7	50.2 ± 3.9	0.66 ± 0.09
^{191}Pt	2.862 d	75.5 ± 8.2	59.7 ± 4.6	0.79 ± 0.11
^{192}Au	4.94 h	120.3 ± 12.9	52.3 ± 4.0	0.43 ± 0.06
^{193}Au	17.65 h	77.7 ± 13.7	63.1 ± 4.8	0.81 ± 0.16
^{194}Au	38.02 h	30.5 ± 3.4	78.1 ± 6.0	2.56 ± 0.35
^{196}Au	*6.1669 d*	*21.9 ± 2.5*	*26.1 ± 2.0*	*1.19 ± 0.16*
^{198}Au	*2.6956 d*	*23.7 ± 2.5*	*34.3 ± 2.6*	*1.45 ± 0.19*
^{199}Au	*3.139 d*	*63.0 ± 11.5*	*36.9 ± 2.8*	*0.31 ± 0.04*
^{193m}Hg	*11.8 h*	*25.7 ± 2.7*	*14.3 ± 1.1*	*0.56 ± 0.07*
^{195}Hg	10.53 h	52.3 ± 6.9	62.0 ± 4.8	1.19 ± 0.18
^{197m}Hg	23.8 h	58.5 ± 9.9	39.6 ± 3.0	0.68 ± 0.13
^{200}Tl	*26.1 h*	*8.9 ± 0.9*	*8.6 ± 0.7*	*0.97 ± 0.13*
^{202}Tl	*12.23 d*	*1.8 ± 0.2*	*1.9 ± 0.1*	*1.06 ± 0.13*

Comparing the experimental production cross sections to the MCNPX calculated cross sections using the Bertini model there were a wide range of results. As suggested by the IAEA benchmark study, many of the calculated production cross sections are within a factor of two of the experimental measured cross sections and a few more are within a factor of three. Of the 53 isotopes experimentally measured cross sections, 30 were within a factor of two and 38 were within a factor of three.

Of the 23 isotopes having greater than a factor of two difference between the measured and calculated cross sections, 13 were in the lower evaporation or the fission part of the spallation residual distribution and 5 were in the evaporation part of the distribution close to the original target atomic mass. For a greater than a factor of three where there were a total of 15 isotopes, 11 are within the fission/low end evaporation range of the model and 2 are close to the original target atomic mass. These residuals at the lower end of the evaporation range as well as the fission range have shown differences in the model calculated production cross sections depending on the physics model used [42].

The 15 residual isotopes that showed a larger than a factor of three differences between the calculated and measured cross sections were: ^{75}Se, ^{83}Rb, ^{95}Nb, ^{95}Zr, ^{102}Rh, ^{110m}Ag, ^{125}Sb, ^{139}Ce, ^{143}Pm, ^{146}Gd, ^{167}Tm, ^{173}Lu, ^{178}W/^{178}Ta ^{182}Os, and ^{189}Ir. Only one isotope of these 15 that were greater than an order of magnitude difference was ^{125}Sb. The experimental measured production cross section of ^{125}Sb was 3.0 ± 0.3 mb where the MCNPX calculated production cross section was 0.048 ± 0.0044 mb. The isotopes ^{75}Se, ^{102}Rh, ^{110m}Ag, and ^{146}Gd had a greater than a factor of 5 difference between the experimentally measured production cross section and the MCNPX calculated cross section. The experimentally measured production cross sections for these 4 isotopes respectively were: 3.8 ± 0.5 mb, 2.8 ± 0.4 mb, 0.7 ± 0.1 mb and 16.8 ± 6.3 mb and the respective MCNPX calculated production cross sections were 0.6 ± 0.05 mb, 0.4 ± 0.03 mb, 0.1 ± 0.01 mb and 2.4 ± 0.2 mb.

While the C/M ratio for each residual gives information regarding the prediction of the production cross sections using the physics models with MCNPX to the measured production cross section it lacks information regarding which residuals may contribute more to radiation doses to individuals. Thus two measures of relative indexes were calculated, one for intake of the residual radionuclide using ICRP 68 [43] dose coefficients

and the second for external exposure using the effective ICRP 60 ground surface dose coefficients from the Federal Guidance Report (FGR) 12 [52]. The residual radioisotopes, ^{160}Ho, ^{165}Tm, ^{183}Os, ^{192}Au and ^{196}Au, do not have ICRP 68 or FGR 12 dose coefficients and the relative indexes for the residuals are excluded.

For the measure of t internal exposure to the analyzed residuals an internal dose index was calculated by multiplying the measured production cross section by the ICRP 68 dose coefficient and multiplying the result by $1x10^{8}$ for readability. The order of the residuals with the highest internal dose index to lowest is given in Table 8 along with the corresponding C/M ratio for the residual.

For the measure of the external exposure to the analyzed residuals an external dose index was calculated by multiplying the measured production cross section by the FGR 12 effective ICRP 60 ground surface dose coefficient and multiplying the result by $1x10^{15}$ for readability. The order of the residuals with the highest external dose index to lowest is given in Table 9 along with the corresponding C/M ratio for the residual.

Table 8: Internal dose index of measured production cross section residuals (All Data Sets).

Isotope	C/M	ICRP 68 Dose Coefficient	Internal Dose Index
^{188}Pt	0.47	7.60E-10	8.02
^{182}Os	0.32	5.60E-10	7.01
^{199}Au	0.31	4.40E-10	5.26
^{167}Tm	0.26	5.60E-10	4.91

Table 8: (Continued)

Isotope	C/M	ICRP 68 Dose Coefficient	Internal Dose Index
^{169}Yb	0.37	7.10E-10	4.78
^{172}Lu	0.76	1.30E-09	4.75
^{189}Ir	0.29	2.40E-10	4.56
^{175}Hf	0.38	4.10E-10	3.65
^{185}Os	0.66	5.10E-10	3.60
^{197m}Hg	0.68	4.70E-10	2.75
^{173}Lu	0.33	2.60E-10	2.61
^{191}Pt	0.79	3.40E-10	2.57
^{146}Gd	0.09	9.60E-10	2.50
^{198}Au	1.45	1.00E-09	2.37
^{171}Lu	0.81	6.70E-10	2.34
^{181}Re	0.73	4.20E-10	2.29
^{173}Hf	0.41	2.30E-10	1.84
^{170}Hf	0.66	4.80E-10	1.73
^{186}Ir	1.57	4.90E-10	1.49

Table 8: (Continued)

Isotope	C/M	ICRP 68 Dose Coefficient	Internal Dose Index
^{176}Ta	0.89	3.10E-10	1.29
^{194}Au	2.56	4.20E-10	1.28
^{166}Tm/^{166}Yb	0.52	2.80E-10	1.21
^{193m}Hg	0.56	4.00E-10	1.03
^{169}Lu	1.12	4.60E-10	1.02
^{193}Au	0.81	1.30E-10	1.01
^{75}Se	0.16	2.60E-09	0.99
^{175}Ta	0.75	2.10E-10	0.94
^{189}Pt	0.66	1.20E-10	0.91
^{187}Ir	0.72	1.20E-10	0.87
^{178}Ta / ^{178}W	1.11	2.50E-10	0.85
^{83}Rb	0.30	1.90E-09	0.63
^{195}Hg	1.19	9.70E-11	0.51
^{125}Sb	0.02	1.10E-09	0.33
^{190}Ir	1.08	1.20E-09	0.31
^{192}Ir	0.73	1.40E-09	0.31

Table 8: (Continued)

Isotope	C/M	ICRP 68 Dose Coefficient	Internal Dose Index
^{110m}Ag	0.14	2.80E-09	0.20
^{102}Rh	0.25	1.20E-09	0.19
^{88}Y	0.36	1.30E-09	0.18
^{200}Tl	0.97	2.00E-10	0.18
^{149}Gd	1.06	4.50E-10	0.15
^{147}Eu	0.97	4.40E-10	0.13
^{95}Nb	0.19	5.80E-10	0.12
^{95}Zr	0.23	8.80E-10	0.11
^{139}Ce	0.30	2.60E-10	0.09
^{202}Tl	1.06	4.50E-10	0.08
^{149}Eu	0.56	1.00E-10	0.07
^{88}Zr	0.38	3.30E-10	0.05
^{143}Pm	0.40	2.30E-10	0.01

Table 9: External dose index of measured production cross section residuals (All Data Sets).

Isotope	C/M	FGR 12 Ground Dose Coefficient	External Dose Index
^{176}Ta	0.89	1.93E-15	80.48
^{166}Tm/^{166}Yb	0.52	1.70E-15	73.27
^{172}Lu	0.76	1.76E-15	64.24
^{182}Os	0.32	4.06E-16	50.79
^{185}Os	0.66	6.81E-16	48.08
^{186}Ir	1.57	1.51E-15	45.90
^{181}Re	0.73	7.20E-16	39.24
^{175}Ta	0.75	8.49E-16	38.12
^{175}Hf	0.38	3.45E-16	30.74
^{173}Hf	0.41	3.73E-16	29.77
^{194}Au	2.56	9.72E-16	29.65
^{193m}Hg	0.56	9.66E-16	24.83
^{187}Ir	0.72	3.37E-16	24.43
^{171}Lu	0.81	6.54E-16	22.82
^{189}Pt	0.66	2.99E-16	22.57

Table 9: (Continued)

Isotope	C/M	FGR 12 Ground Dose Coefficient	External Dose Index
^{169}Lu	1.12	9.56E-16	21.22
^{191}Pt	0.79	2.78E-16	20.99
^{188}Pt	0.47	1.82E-16	19.20
^{170}Hf	0.66	5.11E-16	18.45
^{189}Ir	0.29	6.99E-17	13.29
^{173}Lu	0.33	1.16E-16	11.65
^{167}Tm	0.26	1.31E-16	11.48
^{193}Au	0.81	1.42E-16	11.03
^{200}Tl	0.97	1.22E-15	10.87
^{195}Hg	1.19	1.85E-16	9.68
^{198}Au	1.45	4.07E-16	9.65
^{199}Au	0.31	7.97E-17	9.52
^{146}Gd	0.09	2.22E-16	5.77
^{169}Yb	0.37	7.44E-17	5.01
^{197m}Hg	0.68	8.12E-17	4.75

Table 9: (Continued)

Isotope	C/M	FGR 12 Ground Dose Coefficient	External Dose Index
^{190}Ir	1.08	1.36E-15	3.54
^{88}Y	0.36	2.41E-15	3.37
^{178}Ta / ^{178}W	1.11	9.61E-17	3.27
^{102}Rh	0.25	2.02E-15	3.23
^{110m}Ag	0.14	2.58E-15	1.81
^{83}Rb	0.30	4.76E-16	1.57
^{95}Nb	0.19	7.28E-16	1.53
^{147}Eu	0.97	4.62E-16	1.39
^{75}Se	0.16	3.61E-16	1.37
^{149}Gd	1.06	3.92E-16	1.29
^{125}Sb	0.02	4.09E-16	1.23
^{95}Zr	0.23	7.04E-16	0.92
^{202}Tl	1.06	4.40E-16	0.79
^{88}Zr	0.38	3.77E-16	0.60
^{139}Ce	0.30	1.43E-16	0.47

Table 9: (Continued)

Isotope	C/M	FGR 12 Ground Dose Coefficient	External Dose Index
^{149}Eu	0.56	5.66E-17	0.38
^{192}Ir	0.73	1.47E-16	0.32
^{143}Pm	0.40	2.97E-16	0.15

5.2.1 Residuals with A < 143

As previously discussed, it can be seen that all 11 production cross sections for the residuals with an atomic mass less than 143 have a C/M ratio of less than 0.40. Furthermore the overall average C/M ratio for this group of 11 is 0.25. These 11 isotopes are: ^{75}Se, ^{83}Rb, ^{88}Y, ^{88}Zr, ^{95}Nb, ^{95}Zr, ^{102}Rh, ^{110m}Ag, ^{125}Sb, ^{139}Ce, and ^{143}Pm with ^{88}Y, ^{95}Nb, and ^{110m}Ag being residuals with an independent production cross section. This result is consistent with previous measurements of residuals in this atomic mass range for irradiation of 800 MeV protons on a Ta, W and Au thin foil targets [15, 16, 17, 21, 42]. In addition the MCNPX-Bertini model vastly under predicted the production cross section of ^{126}I in the work by K. Kelley [42] with a C/M ratio of 0.001, 0.06 and 0.001 for 800 MeV protons on Ta, W and Au foil targets, respectively. This similar order of magnitude under prediction is seen in this work with the ^{125}Sb residual. These results suggest that an overall change in the prediction of the production cross sections is needed in the MCNPX-Bertini model for this region of the spallation residual spectrum.

5.2.2 Cumulative Production Cross Section of ^{146}Gd

The C/M ratio for the cumulative production cross section of ^{146}Gd was determined to be 0.09 based on this work. While not identified as an internal or external radiological hazard based on the internal and external dose index numbers from Tables 8 and 9. This isotope represents an important region of interest in spallation models due to its proximity to the ^{148}Gd isotope, a well-known radiological hazard due to its alpha particle decay and 70.9 year half-life. Figure 7 shows the decay scheme of the precursor residuals that feed into the ^{146}Gd cross section.

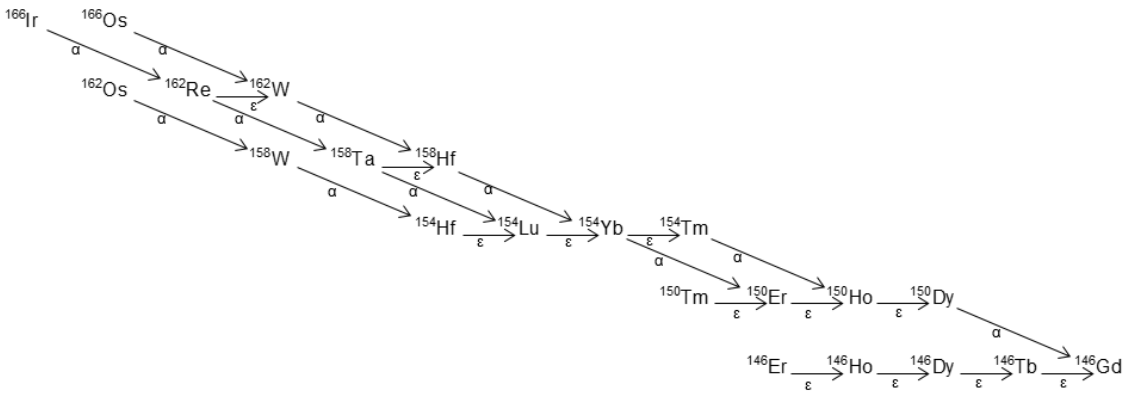

Figure 7: Decay diagram feeding ^{146}Gd

As seen in the Figure 7, a total of 20 precursor residuals feed the production of the ^{146}Gd through a series of electron capture and alpha decays. However the MCNPX model only predicts production cross sections for the precursor residuals with an atomic mass number less than 154. Residuals with higher atomic mass numbers would however only represent a small fraction <1% of the predicted production cross section due to the low probability of occurrence. The gamma spectroscopy data in data sets 4 and 5 show the activity determined from 154.6 keV photopeak is approximately twice that of the activity determined from the 114.7 and 115.5 keV photopeaks which feeds into the higher

uncertainty for the measured ^{146}Gd production. However even removing the 154.6 keV photopeak data the C/M ratio would still be ~0.30 showing that MCNPX model under predicting the production cross section.

5.2.3 Cumulative Production Cross Section of ^{182}Os

The C/M ratio for the cumulative production cross section of ^{182}Os was determined to be 0.32. While just slightly less than a factor of 2 difference, the ^{182}Os residual one of the first residuals appearing in the ranked order of internal and external dose indexes in both Table 8 and 9 with a factor of 2 difference. Figure 8 show the decay scheme of the precursor residuals that feed into the ^{182}Os production cross section.

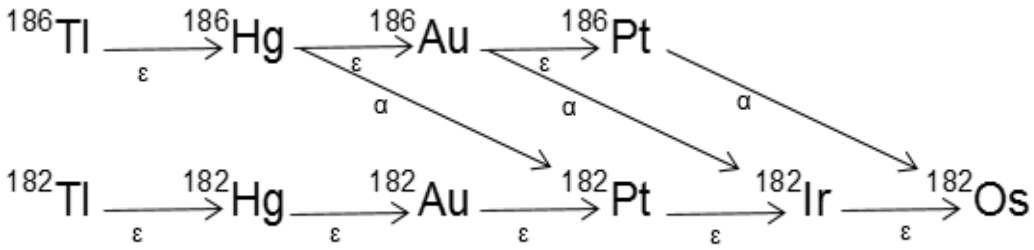

Figure 8: Decay diagram feeding ^{182}Os

Of the 8 precursors that feed the ^{182}Os production cross section only the precursors in the electron capture production chain with an atomic mass number of 182 significantly contribute to the its production since al the alpha decay probabilities are small.

5.3 Distribution of Spallation Residuals within Irradiated Mercury Targets

After acquisition of gamma-ray spectra measurements at eight various times post irradiation, the filled targets were shipped to ORNL to be drained into a two small vials (~6.5 g of mercury from each target) and two large bottles (~39 g of mercury from each target). The vials, bottles and the empty targets were then shipped back to Georgia Tech for further gamma-ray spectroscopic analysis. Gamma-ray spectroscopy counts were taken for each of the small vials and the large bottles. The empty encapsulations were taken apart and photographed, and then a thin layer of adhesive film was used to cover the interior surfaces of the encapsulation that were in contact with the irradiated mercury. This was to prevent contamination of the HPGe detector during the gamma-ray measurements of these parts.

Figures 9 and 10 show the fine layer of film that was deposited onto parts of the encapsulation. It can be seen that the deposits are greater towards the top of the cavity suggesting that these deposits attach to the stainless steel over time. This is due to the storage of the targets in an upright position on their support brackets while they decayed between gamma-ray spectroscopy counts. In addition to the noticeable film left on the components of the stainless steel encapsulations, the film was also noticed floating on the top of the liquid mercury in the vials and the bottles.

After taking the gamma-ray spectroscopy data on the components, the adhesive film was removed from the entry window side of the Hg-1 target and replaced with another layer of film. The film was then counted on the planar HPGe detector to determine the percentage of these deposited that could be readily removed.

Figure 9: Photo of back side of entry window of target Hg-1, top of assembly is to the left to the photo

Figure 10: Photo of the cavity inside of target Hg-1, top of target assembly is to the left

Figure 11: Photo of film after removal showing deposits attached

Within the data acquired after receiving the emptied targets and the associated vials and bottles only 14 remaining radioisotopes could be identified. Of those fourteen residuals, 11 were identified in the film deposits that were removed with the adhesive film layer, three did not appear on the adhesive film. Full energy photopeaks for ^{203}Hg appear in both the gamma-ray spectroscopy data of the residual film and within the vials/bottles. Table 10 shows the average percentage of each radioisotope that was removed with the adhesive film layer. The range of percentage removed for the spallation residuals was between 39% and 79%. With the percentage of removal of 66% ^{203}Hg it can be inferred that the residuals isotopes are typically made up of molecules containing mercury.

Table 10: Percentage of radioisotope removed with adhesive film layer

Isotope	Percentage Removed
^{83}Rb	39%
^{88}Y	62%
^{88}Zr	41%
^{95}Nb	61%
^{102}Rh	70%
^{125}Sb	79%
^{143}Pm	50%
^{172}Lu	75%
^{173}Lu	60%
^{185}Os	51%
^{203}Hg	66%

Of the three other isotopes, ^{110m}Ag, ^{172}Hf, and ^{195}Au were found in the vial/bottle of the irradiated mercury but not in the residue, the specific activity (Bq/cc) of these three residuals were almost identical between the vial and bottle samples suggesting that these isotopes distribute evenly within the target mercury.

The other isotopes that are found in the residue have variations of specific activity confirming their presence in the residue that floats on top of the mercury. Table 11 shows the calculated specific activity of each radioisotope in both the vial and the bottle and indicates if they are present in the residue film that deposits on the stainless steel encapsulation.

Table 11: Specific activity of isotopes in irradiated mercury from target Hg-1, in the small vial sample and the large bottle sample and if the isotope is present in residue deposits on stainless steel

Isotope	Vial Specific Activity (Bq/cc)	Bottle Specific Activity (Bq/cc)	Present in Deposited Residue?
^{83}Rb	4.85E-01 ± 3.87E-02	3.91E-01 ± 2.92E-02	Yes
^{88}Y	2.21E+00 ± 1.66E-01	1.90E+00 ± 1.42E-01	Yes
^{88}Zr	2.79E-01 ± 2.30E-02	2.24E-01 ± 1.73E-02	Yes
^{95}Nb	7.01E-02 ± 5.95E-03	5.25E-02 ± 4.07E-03	Yes
^{102}Rh	9.60E-01 ± 7.66E-02	8.78E-01 ± 6.68E-02	Yes
^{110m}Ag	1.38E-01 ± 1.03E-02	1.28E-01 ± 9.50E-03	No
^{125}Sb	9.01E-02 ± 8.28E-03	8.84E-02 ± 7.17E-03	Yes
^{143}Pm	3.07E+00 ± 2.54E-01	2.86E+00 ± 2.19E-01	Yes
^{172}Lu	1.69E+01 ± 1.25E+00	1.64E+01 ± 1.22E+00	Yes
^{173}Lu	7.89E+00 ± 5.91E-01	7.60E+00 ± 5.65E-01	Yes
^{172}Hf	1.67E+01 ± 1.29E+00	1.63E+01 ± 1.22E+00	No
^{185}Os	1.58E+01 ± 1.18E+00	1.30E+01 ± 9.65E-01	Yes
^{195}Au	1.15E+02 ± 8.55E+00	1.04E+02 ± 7.72E+00	No
^{203}Hg	6.86E-01 ± 5.17E-02	4.61E-01 ± 3.45E-02	Yes

CHAPTER 6: DISSCUSION AND CONCLUSION

The Spallation Neutron Source (SNS) and the Japan Proton Accelerator Research Complex use flowing liquid mercury targets to produce experimental neutrons through spallation reactions. Unlike other spallation neutron sources that use solid heavy metal targets these two facilities have unique radiological hazards based on the distribution of radioactive spallation residual isotopes throughout the liquid mercury target system. This poses hazards both during the operational lifetime of the facility as well as during the decommissioning of the facility at the end of its life. To better understand these hazards it is important to understand the production rate of the spallation residuals as well as the potential distribution of the residuals in the target system. In the design of these facilities the modeling of the spallation residuals was accomplished through computational models. The computational models have been developed throughout the years and typically have predicted the production of spallation residuals within a factor of two. Furthermore benchmark experiments involving the irradiation of thin-foil solid metal targets are used to validate the calculation models. While the computation models have been used to estimate the spallation residuals in the above two facilities no previous experiment has been conducted to determine the production cross sections of medium and longer half-life residuals in mercury.

Two irradiations were completed on a small volume of liquid mercury using 800 MeV protons at the Los Alamos Neutron Science Center in the WNR blue room facility. Following the irradiation the targets were measured using gamma spectroscopy with HPGe detectors at discrete times over a period of just over a year to measure the spallation residuals present and to ultimately calculate a production cross section. The

proton flux was measured via Al activation foils to produce ^{22}Na also measured by gamma spectroscopy. Overall agreement between MCNPX production cross sections and those measured by gamma spectroscopy was close especially for isotopes near the target nucleus and near the line of stability. However for several residuals in the fission modeling range and in the transition area between the fission model and the evaporation model showed larger differences between the measured and calculated production cross sections. These differences are consistent with other benchmark experiments for solid metal targets in the fission model and evaporation/fission transition model area when compared to the MCNPX predictions.

Of the 53 residual production cross sections measured there were five that showed significant differences between the MCNPX calculated cross sections and the experimentally measured ones. These were ^{75}Se, ^{102}Rh, ^{110m}Ag, ^{125}Sb and ^{146}Gd, with ^{125}Sb showing the greatest difference between the calculated and measured results. Analysis after removing the mercury from the targets showed that many of the residuals produced possible create compounds with the mercury and deposit on the stainless steel over time. In addition to depositing to the stainless steel these residue can easily be removed. The measured specific activity of three residual isotopes, ^{110m}Ag, ^{172}Hf, and ^{195}Au were nearly identical in the small vial and large bottle samples indicating that these isotopes are homogeneously distributed within the mercury. In addition these three isotopes were not identified on the residue left on the target enclosure components or on the sample of residue removed from the front target window.

APPENDIX A:

Radionuclide Library

Table A-1: Radionuclide library used in GENIE2000™ software or in manual evaluation of irradiated samples. Half-life, gamma energies, and γ – abundances, were obtained from [40]. Data set(s) indicate the associated data set in which the radionuclide library information was used.

Isotope	Half-life (T1/2)	Eγ (keV)	Abundance (%)	Data Set(s)	Comments
^{75}Se	119.779 d	264.7 400.7	58.9 11.5	6,7,8	
^{83}Rb	86.2 d	520.4 529.6	45.0 29.3	6,7,8	
^{88}Y	106.61 d	898.4 1836.1	93.7 99.1	7,8,	
^{88}Zr	83.4 d	392.9	97.2	6,7,8	
^{95}Zr	64.032 d	724.2 756.7	44.2 54.5	6,7,8	
^{95}Nb	34.991 d	765.8	99.8	6,7,8	
^{102}Rh	207 d	475.1	42.0	7,8	
^{110m}Ag	249.76 d	657.8 884.7 937.5 1384.3 1505.0	95.6 75.0 35.0 25.1 13.3	8	
^{125}Sb	2.7586 y	600.6	17.7	8	
^{139}Ce	137.64 d	165.9	79.9	7,8	
^{143}Pm	265 d	742.0	38.5	7,8	
^{147}Eu	24.1 d	197.3 677.5 955.8 1077.0	26.5 9.80 3.84 6.10	4,5	
^{149}Eu	93.1 d	277.1 327.5	3.56 4.03	7	
^{146}Gd	48.27 d	114.7 115.5 154.6	44.0 44.0 46.6	4,5	

Table A-1: (Continued)

Isotope	Half-life (T1/2)	Eγ (keV)	Abundance (%)	Data Set(s)	Comments
^{149}Gd	9.28 d	260.7 272.3 298.6 346.6 645.3	1.32 3.21 28.6 23.9 1.46	4	
^{160}Ho	25.6 m	538.6 645.4 646.3 728.2 65.3 872.0 879.4 962.4 966.2 1004.7 1130.6	6.00 24.7 4.70 46.9 5.10 9.40 26.6 25.6 21.9 2.90 1.66	4,5,6,7,8	Daughter of ^{160}Er (T1/2: 28.58h)
^{165}Tm	30.06 h	218.9 242.9 297.4 346.9 356.5 389.4 460.3 698.8 806.4 1131.3 1184.4	3.34 35.5 12.7 1.50 2.75 2.82 4.12 1.29 9.50 1.73 2.95	3	

Table A-1: (Continued)

Isotope	Half-life (T1/2)	Eγ (keV)	Abundance (%)	Data Set(s)	Comments
^{166}Tm	7.70 h	215.2 459.6 594.4 598.8 672.2 674.8 691.2 705.3 757.8 778.8 785.9 875.6 1152.3 1176.7 1275.5 1300.7 1374.2 1867.9 1895.1 2052.4 2079.5	5.20 2.51 3.46 2.10 6.10 2.57 7.40 11.0 2.33 18.9 9.90 4.06 1.55 9.50 14.9 1.33 5.60 4.04 1.20 17.2 6.30	3	
^{167}Tm	9.25 d	207.8	41.0	4,5,6	
^{169}Yb	32.018 d	109.8 130.5 177.2 198.0 261.1 307.7	17.5 11.3 22.2 35.8 1.71 10.1	4,5,6,7	
^{169}Lu	34.06 h	889.7 960.6 1007.5 1078.3 1184.9 1290.6 1379.0 1392.3 1449.7 1466.8	5.36 23.4 1.80 1.07 2.22 1.14 1.08 1.20 9.90 3.32	3	

Table A-1: (Continued)

Isotope	Half-life (T1/2)	Eγ (keV)	Abundance (%)	Data Set(s)	Comments
^{171}Lu	8.24 d	667.4 689.3 712.6 739.8 780.7 839.9 853.0	11.0 2.37 1.13 47.8 4.36 3.04 2.55	4,5	
^{172}Lu	6.7 d	203.4 323.9 372.5 377.5 410.3 432.5 490.4 540.2 697.3 912.1 929.1 1002.7 1022.4 1093.6 1488.9 1542.9 1584.1 1621.9	5.02 1.50 2.66 3.35 1.98 1.64 1.91 1.40 6.10 15.3 3.04 5.25 1.41 63.0 1.15 1.02 2.64 2.16	4,5,6,7,8	Daughter of ^{172}Hf (T1/2: 1.87y)
^{173}Lu	1.37 y	272.1 636.1	21.2 1.45	4,5,6,7,8	
^{170}Hf	16.01 h	208.1 349.0 481.3 501.6 572.9 620.7	2.70 1.10 3.70 3.70 15.0 18.0	3	
^{173}Hf	23.6 h	297.0 311.2	33.9 10.7	3	
^{175}Hf	70 d	343.4 433.0	84.0 1.44	4,5,6,7,8	

Table A-1: (Continued)

Isotope	Half-life (T1/2)	Eγ (keV)	Abundance (%)	Data Set(s)	Comments
^{175}Ta	10.5 h	207.4 266.9 348.5 393.2 436.4 475.0 857.7 998.3 1225.6 1586.0 1618.2 1636.0 1659.2 1721.8 1793.1	14.0 10.8 12.0 2.12 3.80 2.00 3.20 2.60 2.50 1.60 1.32 1.70 1.08 1.16 4.60	3	

Table A-1: (Continued)

Isotope	Half-life (T1/2)	Eγ (keV)	Abundance (%)	Data Set(s)	Comments
^{176}Ta	8.09 h	201.8 521.6 611.2 710.5 1023.1 1157.4 1159.3 1190.2 1222.9 1225.0 1252.9 1291.0 1341.3 1357.5 1555.0 1584.0 1616.2 1630.8 1633.7 1643.4 1672.3 1679.2 1696.5 1704.7 1722.0 1774.6 1823.7 1862.7 2044.9 2832.0 2920.4	5.70 2.43 1.26 5.40 2.67 3.40 24.7 4.50 2.00 5.70 3.08 1.33 3.34 2.00 4.00 5.30 1.29 1.77 2.93 2.40 1.19 1.20 4.60 1.40 3.27 1.56 4.50 4.00 1.35 4.30 2.19	1,2,3	
^{178}Ta	2.36 h	1340.0 1350.5	1.03 1.18	4,5,6	Daughter of ^{178}W (T1/2: 21.6d)

Table A-1: (Continued)

Isotope	Half-life (T1/2)	Eγ (keV)	Abundance (%)	Data Set(s)	Comments
^{181}Re	19.9 h	318.6 356.1 360.7 365.5 412.3 639.0 651.2 661.8 805.2 907.4 953.6 1000.2 1009.4 1440.7	1.10 1.70 20.0 56.0 1.00 6.40 1.00 3.00 3.10 1.00 3.60 3.30 2.40 1.90	1,2,3	
^{183}Re	70.0 d	208.8 291.7	2.95 3.05	4,5,6,7,8	
^{182}Os	22.1 h	180.2 263.3 274.3 510.0	33.5 6.71 1.81 52.4	1,2,3	
^{183}Os	13.0 h	236.4 381.8 851.5	3.41 89.6 4.56	1,2,3	
^{185}Os	93.6 d	592.1 646.1 717.4 874.8 880.5	1.32 78.0 3.94 6.29 5.17	4,5,6,7,8	
^{186}Ir	16.64 h	296.9 420.8 434.8 630.3 636.4 649.8 773.3 805.5 841.5 933.3 1026.5 1171.5 1647.4	64.0 2.87 34.4 4.40 6.20 1.39 9.10 1.19 5.00 5.30 1.22 1.50 4.80	1,2,3	

Table A-1: (Continued)

Isotope	Half-life (T1/2)	Eγ (keV)	Abundance (%)	Data Set(s)	Comments
^{187}Ir	10.5 h	400.8 427.0 491.7 501.5 610.9 912.9 977.5 987.3	3.94 4.12 1.27 1.46 3.93 4.79 3.14 2.80	1,2,3	
^{189}Ir	13.2 d	245.1	6.00	4,5	
^{190}Ir	11.78 d	207.9 361.1 371.2 407.2 477.8 557.9 569.3 605.1 630.9 829.0 839.1	1.19 13.0 22.8 4.60 1.82 30.1 28.5 39.9 2.90 3.50 1.14	4,5	
^{192}Ir	73.827 d	316.5 468.1	82.8 47.8	6,7,8	
^{188}Pt	10.2 d	187.6 195.0 381.4 423.3 478.3	19.4 18.6 7.50 4.40 1.80	3,4,5	
^{189}Pt	10.87 h	223.3 243.5 300.5 317.6 544.9 568.8 607.6 792.7	1.49 7.00 3.70 3.30 5.80 7.10 5.50 1.35	1,2,3	
^{191}Pt	2.862 d	351.2 359.9 409.4 456.5 538.9 624.1	3.40 6.00 8.00 3.40 13.7 1.41	3	

Table A-1: (Continued)

Isotope	Half-life (T1/2)	Eγ (keV)	Abundance (%)	Data Set(s)	Comments
^{192}Au	4.94 h	296.0 308.5 316.5 468.1 477.1 612.5 759.1 1122.8 1140.4 1423.0 1576.5 1624.4 1706.6 1723.1 1832.8 1921.2 1940.8 2019.2	22.0 3.40 58.0 1.75 1.08 4.0 1.65 1.10 2.60 3.00 2.30 1.67 1.92 3.10 3.20 3.20 1.60 1.48	1,2,3	
^{193}Au	17.65 h	186.2 268.2	10.1 3.90	1,2,3	
^{194}Au	38.02 h	328.5 364.9 528.8 622.0 645.2 948.3 1175.3 1342.1 1468.9 1592.4 1595.8 1887.0 1924.2 2043.7	61.0 1.51 1.65 1.71 2.14 2.20 2.01 1.22 6.40 1.10 1.71 1.40 2.01 3.60	1,2,3	
^{196}Au	6.1669 d	355.7 426.1	87.0 7.20	3	
^{198}Au	2.6956 d	411.8	95.58	3	
^{199}Au	3.139 d	208.2	8.72	3	

Table A-1: (Continued)

Isotope	Half-life (T1/2)	Eγ (keV)	Abundance (%)	Data Set(s)	Comments
^{193m}Hg	11.8 h	218.1 219.7 258.0 382.5 394.0 407.6 461.8 573.2 600.6 776.6 877.8 913.1 932.4 994.6 1174.0 1325.5 1339.6 1365.1 1648.5	5.30 2.80 61.00 4.30 3.12 25.18 1.11 14.2 2.10 1.10 2.70 1.08 6.70 1.59 2.00 2.14 1.50 1.44 1.30	3	
^{195}Hg	10.53 h	207.1 261.7 585.1 599.7 779.8 1172.4	1.57 1.50 1.99 1.78 6.80 1.24	1,2,3	
^{197m}Hg	23.8 h	279.0	6.10	3	
^{200}Tl	26.1 h	367.9 579.3 661.3 787.1 828.3 1205.7 1225.5 1273.5 1407.6 1514.9	87.2 13.8 2.28 1.03 10.8 29.9 3.36 3.31 1.45 4.00	3	
^{202}Tl	12.23 d	439.6	91.4	4,5	

APPENDIX B

Cumulative Production Cross Sections

Table B-1: Cumulative radionuclides measured and the sum of their independent contributors.

Cumulative Radionuclide	Independent radionuclides and their contributions
^{75}Se	^{75}Se + ^{75}Br + ^{75}Kr + ^{75}Rb + ^{75}Sr
^{83}Rb	^{83}Rb + ^{83}Sr + ^{83}Y
^{88}Y	^{88}Y + ^{88}Zr + ^{88}Nb + ^{88}Mo + ^{88}Tc + ^{88}Ru
^{88}Zr	^{88}Zr + ^{88}Nb + ^{88}Mo + ^{88}Tc + ^{88}Ru
^{95}Zr	^{95}Zr + ^{95}Y+ ^{95}Sr + ^{95}Rb + ^{95}Kr + ^{95}Br
^{95}Nb	^{95}Nb + ^{95}Zr + ^{95}Y+ ^{95}Sr + ^{95}Rb + ^{95}Kr + ^{95}Br
^{102}Rh	^{102}Rh
^{110m}Ag	^{110m}Ag
^{125}Sb	^{125}Sb + ^{125}Sn + ^{125}In + ^{125}Cd + ^{125}Ag
^{139}Ce	^{139}Ce + ^{139}Pr + ^{139}Nd + ^{139}Pm + ^{139}Sm + ^{139}Eu + ^{139}Gd
^{143}Pm	^{143}Pm + ^{143}Sm + ^{143}Eu + ^{143}Gd + ^{143}Tb + ^{143}Dy + ^{143}Ho + ^{147}Eu(2.2e-5)
^{147}Eu	^{147}Eu + ^{147}Gd + ^{147}Tb + ^{147}Dy + ^{147}Ho + ^{147}Er + ^{147}Tm(0.900) + ^{151}Tb(9.5e-5) + ^{151}Dy(0.056) + ^{151}Ho(0.264) + ^{151}Er(0.264) + ^{151}Tm(0.264) + ^{151}Yb(0.264) + ^{151}Lu(0.185) + ^{155}Er(1.23e-5) + ^{155}Tm(0.005) + ^{155}Yb(0.235) + ^{155}Lu(0.258) + ^{155}Hf(0.264) + ^{159}Lu(2.01e-6) + ^{159}Hf(0.097) + ^{159}Ta(0.226) + ^{159}W(0.264) + ^{163}Ta(4.02e-9) + ^{163}W(0.040) + ^{163}Re(0.159) + ^{163}Os(0.264) + ^{167}Re(2.81e-11) + ^{167}Os(0.027) + ^{167}Ir(0.159) + ^{171}Ir(2.81e-11) + ^{171}Pt(0.026) + ^{175}Au(2.64e-11) +^{175}Hg(0.026)
^{149}Eu	^{149}Eu + ^{149}Gd + ^{149}Tb(0.833) + ^{149}Dy(0.833) + ^{149}Ho(0.833) + ^{149}Er(0.833) + ^{153}Er(0.441) + ^{153}Tm(0.798) + ^{153}Yb(0.815) + ^{157}Lu(0.798) + ^{157}Hf(0.813) + ^{161}Ta(0.040) + ^{161}W(0.674)
^{146}Gd	^{146}Gd + ^{146}Tb + ^{146}Dy + ^{146}Ho + ^{146}Er + ^{146}Tm(0.550) + ^{150}Dy(0.360) + ^{150}Ho(0.360) + ^{150}Er(0.360) + ^{150}Tm(0.360) + ^{154}Tm(0.158) + ^{154}Yb(.0345) + ^{154}Lu(0.345) + ^{154}Hf(0.345) + ^{158}Hf(0.152) + ^{158}Ta(0.332) + ^{158}W(0.345) + ^{162}W(0.071) + ^{162}Re(0.316) + ^{162}Os(0.345) + ^{166}Os(0.051) + ^{166}Ir(0.297)
^{149}Gd	^{149}Gd + ^{149}Tb(0.833) + ^{149}Dy(0.833) + ^{149}Ho(0.833) + ^{149}Er(0.833) + ^{153}Er(0.441) + ^{153}Tm(0.798) + ^{153}Yb(0.815) + ^{157}Lu(0.798) + ^{157}Hf(0.813) + ^{161}Ta(0.040) + ^{161}W(0.674)
^{160}Ho	^{160}Ho + ^{160}Er + ^{160}Tm + ^{160}Yb + ^{160}Lu + ^{160}Hf(0.993) + ^{160}Ta(0.655) + ^{164}Re(0.419) + ^{168}Ir(0.419) + ^{172}Au(0.419)

Table B-1: (Continued)

Cumulative Radionuclide	Independent radionuclides and their contributions
^{165}Tm	^{165}Tm + ^{165}Yb + ^{165}Lu + ^{165}Hf + ^{165}Ta + ^{165}W + ^{165}Re(0.870) + ^{169}Re(0.002) + ^{169}Os(0.112) + ^{169}Ir(0.870) + ^{173}Au(0.870)
^{166}Tm	^{166}Tm + ^{166}Yb + ^{166}Lu + ^{166}Hf + ^{166}Ta + ^{166}W(0.999) + ^{166}Re(0.919) + ^{166}Os(0.257) + ^{170}Ir(0.689) + ^{170}Pt(0.257) + ^{174}Au(0.689) + ^{174}Hg(0.257)
^{167}Tm	^{167}Tm + ^{167}Yb + ^{167}Lu + ^{167}Hf + ^{167}Ta + ^{167}W + ^{167}Re + ^{167}Os(0.33) + ^{171}Pt(0.337) + ^{171}Ir + ^{171}Os(0.017) + ^{175}Pt(0.011) + ^{175}Au(0.940) + ^{175}Hg(0.337) + ^{179}Hg(0.006)
^{169}Yb	^{169}Yb + ^{169}Lu + ^{169}Hf + ^{169}Ta + ^{169}W + ^{169}Re + ^{169}Os(0.890) + ^{173}Os(2.1e-4) + ^{173}Ir(0.070) + ^{173}Pt(0.759) + ^{177}Pt(1.18e-5) + ^{177}Au(0.028) + ^{177}Hg(0.649) + ^{181}Hg(4.23e-6)
^{169}Lu	^{169}Lu + ^{169}Hf + ^{169}Ta + ^{169}W + ^{169}Re + ^{169}Os(0.890) + ^{173}Os(2.1e-4) + ^{173}Ir(0.070) + ^{173}Pt(0.759) + ^{177}Pt(1.18e-5) + ^{177}Au(0.028) + ^{177}Hg(0.649) + ^{181}Hg(4.23e-6)
^{171}Lu	^{171}Lu + ^{171}Hf + ^{171}Ta + ^{171}W + ^{171}Re + ^{171}Os(0.983) + ^{175}Ir(0.0085) + ^{175}Pt(0.629)
^{172}Lu	^{172}Lu + ^{172}Hf + ^{172}Ta + ^{172}W + ^{172}Re + ^{172}Os(0.990) + ^{172}Ir(0.970) + ^{172}Pt(0.058) + ^{176}Ir(0.021) + ^{176}Pt(0.990) + ^{176}Au(0.970) + ^{176}Hg(0.058) + ^{180}Au(3.78e-4) + ^{180}Hg(0.475)
^{173}Lu	^{173}Lu + ^{173}Hf + ^{173}Ta + ^{173}W + ^{173}Re + ^{173}Os + ^{173}Ir(0.93) + ^{173}Pt(0.149) + ^{177}Pt(0.113) + ^{177}Ir(0.060) + ^{177}Au(0.440) + ^{177}Hg(0.192) + ^{181}Au(7.8e-4) + ^{181}Hg(0.041)
^{170}Hf	^{170}Hf + ^{170}Ta + ^{170}W + ^{170}Re +^{170}Os(0.880) + ^{174}Pt(0.739) + ^{178}Hg(0.739)
^{172}Hf	^{172}Hf + ^{172}Ta + ^{172}W + ^{172}Re + ^{172}Os(0.990) + ^{172}Ir(0.970) + ^{172}Pt(0.058) + ^{176}Ir(0.021) + ^{176}Pt(0.990) + ^{176}Au(0.970) + ^{176}Hg(0.058) + ^{180}Au(3.78e-4) + ^{180}Hg(0.475)
^{173}Hf	^{173}Hf + ^{173}Ta + ^{173}W + ^{173}Re + ^{173}Os + ^{173}Ir(0.93) + ^{173}Pt(0.149) + ^{177}Pt(0.113) + ^{177}Ir(0.060) + ^{177}Au(0.440) + ^{177}Hg(0.192) + ^{181}Au(7.8e-4) + ^{181}Hg(0.041)
^{175}Hf	^{175}Hf + ^{175}Ta + ^{175}W + ^{175}Re + ^{175}Os + ^{175}Ir(0.991) + ^{175}Pt(0.357) +^{175}Au(0.021) + ^{179}Pt(2.4e-3) + ^{179}Au(0.220) + ^{179}Hg(0.189)
^{175}Ta	^{175}Ta + ^{175}W + ^{175}Re + ^{175}Os + ^{175}Ir(0.991) + ^{175}Pt(0.357) +^{175}Au(0.021) + ^{179}Pt(2.4e-3) + ^{179}Au(0.220) + ^{179}Hg(0.189)
^{176}Ta	^{176}Ta + ^{176}W + ^{176}Re + ^{176}Os + ^{176}Ir(0.979) + ^{176}Pt(0.607) + ^{180}Pt(.003) + ^{180}Au(0.021) + ^{180}Hg(0.302) + ^{184}Hg(3.78e-5)
^{178}Ta	^{178}Ta + ^{178}W + ^{178}Re + ^{178}Os + ^{178}Ir + ^{178}Pt(0.954) + ^{178}Au(0.572) + ^{182}Pt(3.1e-4) + ^{182}Au(1.61e-3) + ^{182}Hg(0.146) + ^{186}Hg(4.9e-4)

Table B-1: (Continued)

Cumulative Radionuclide	Independent radionuclides and their contributions
^{181}Re	^{181}Re + ^{181}Os + ^{181}Ir + ^{181}Pt + ^{181}Au(0.987) + ^{181}Hg(0.631) + ^{185}Au(2.6e-3) + ^{185}Hg(0.062)
^{182}Os	^{182}Os + ^{182}Ir + ^{182}Pt + ^{182}Au(0.998) + ^{182}Hg(0.847) +^{182}Tl(0.813) + ^{186}Pt(1.0e-6) + ^{186}Au(9.4e-6) + ^{186}Hg(1.7e-4) + ^{186}Tl(1.7e-4)
^{183}Os	^{183}Os + ^{183}Ir + ^{183}Pt + ^{183}Au(0.997) + ^{183}Hg(0.880) +^{187}Au(3.0e-5)+ ^{187}Hg(3.1e-5)
^{185}Os	^{185}Os + ^{185}Ir + ^{185}Pt + ^{185}Au + ^{185}Hg(0.94)
^{186}Ir	^{186}Ir + ^{186}Pt + ^{186}Au + ^{186}Hg + ^{186}Tl
^{187}Ir	^{187}Ir + ^{187}Pt + ^{187}Au + ^{187}Hg + ^{187}Tl
^{189}Ir	^{189}Ir +^{189}Pt + ^{189}Au + ^{189}Hg + ^{189}Tl
^{190}Ir	^{190}Ir
^{192}Ir	^{192}Ir
^{188}Pt	^{188}Pt + ^{188}Au + ^{188}Hg + ^{188}Tl
^{189}Pt	^{189}Pt + ^{189}Au + ^{189}Hg + ^{189}Tl
^{191}Pt	^{191}Pt + ^{191}Au + ^{191}Hg + ^{191}Tl
^{192}Au	^{192}Au + ^{192}Hg + ^{192}Tl
^{193}Au	^{193}Au + ^{193}Hg + ^{193}Tl
^{194}Au	^{194}Au + ^{194}Hg + ^{194}Tl
^{196}Au	^{196}Au
^{198}Au	^{198}Au
^{199}Au	^{199}Au
^{193m}Hg	^{193m}Hg
^{195}Hg	^{195}Hg + ^{195}Tl
^{197}Hg	^{197}Hg + ^{197}Tl
^{197m}Hg	^{197m}Hg
^{200}Tl	^{200}Tl
^{202}Tl	^{202}Tl

APPENDIX C:

Gamma Spectroscopy Spectra

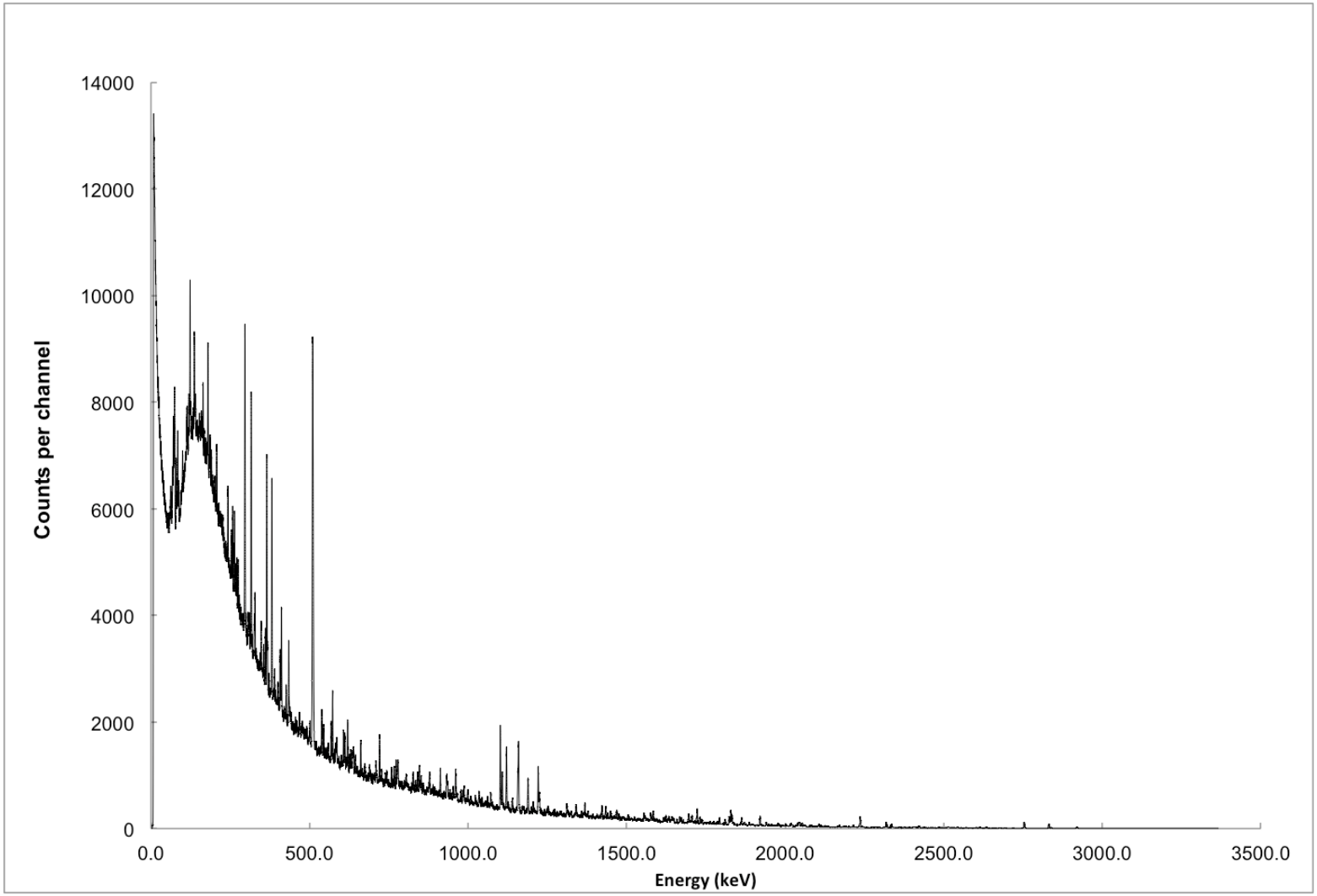

Figure C-1: Mercury Target Hg-1 Gamma Spectra, Data Set #1

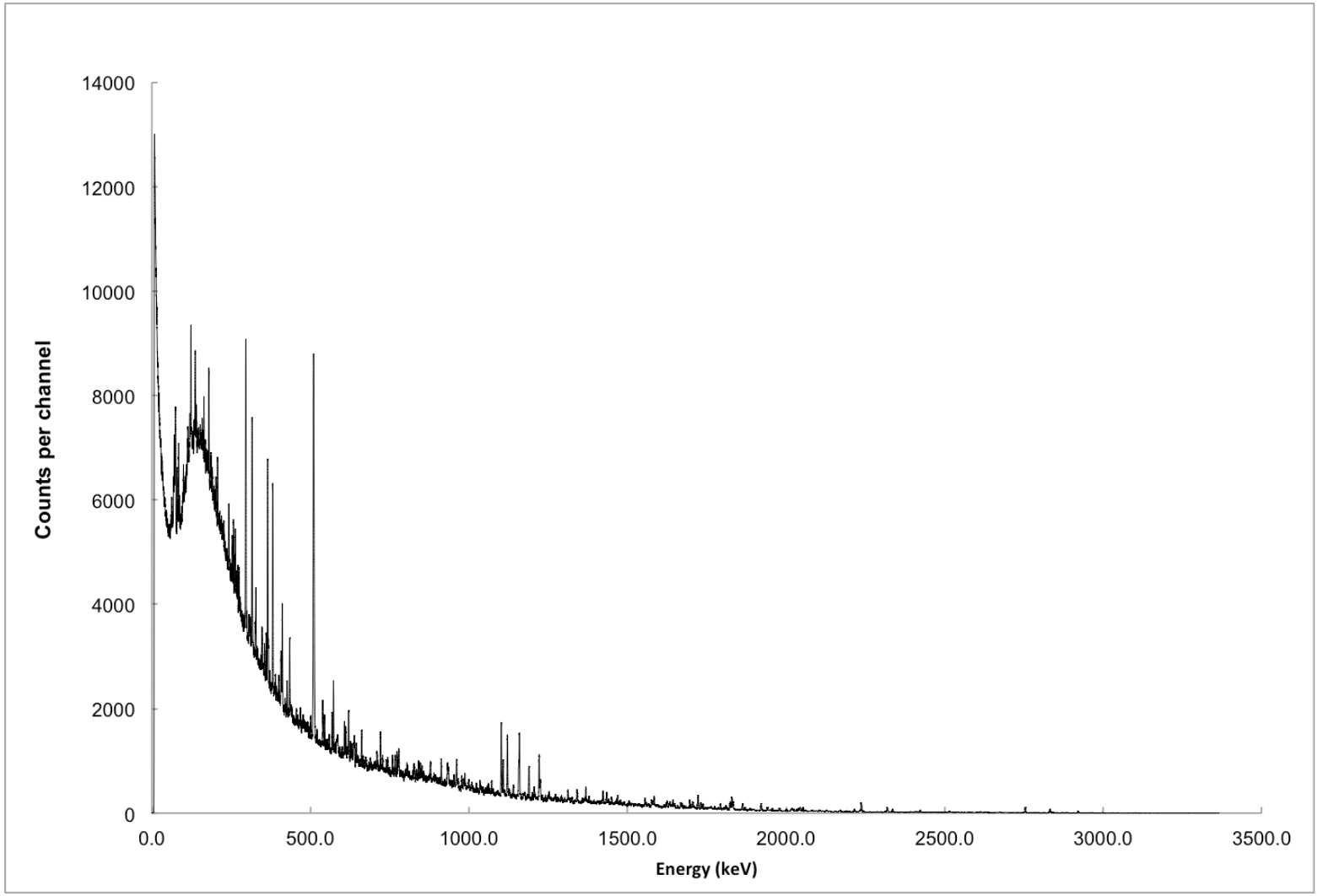

Figure C-2: Mercury Target Hg-2 Gamma Spectra, Data Set #1

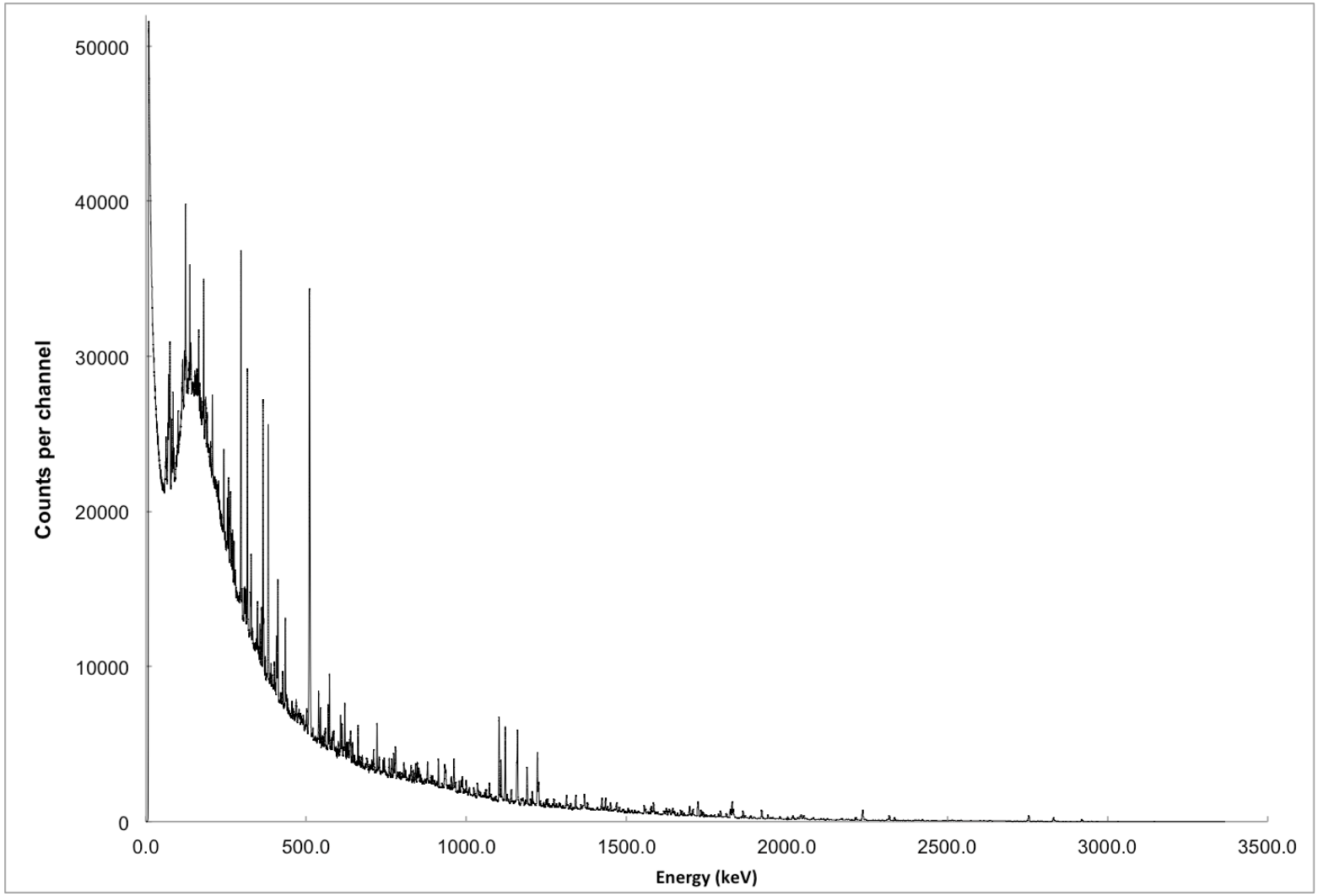

Figure C-3: Mercury Target Hg-1 Gamma Spectra, Data Set #2

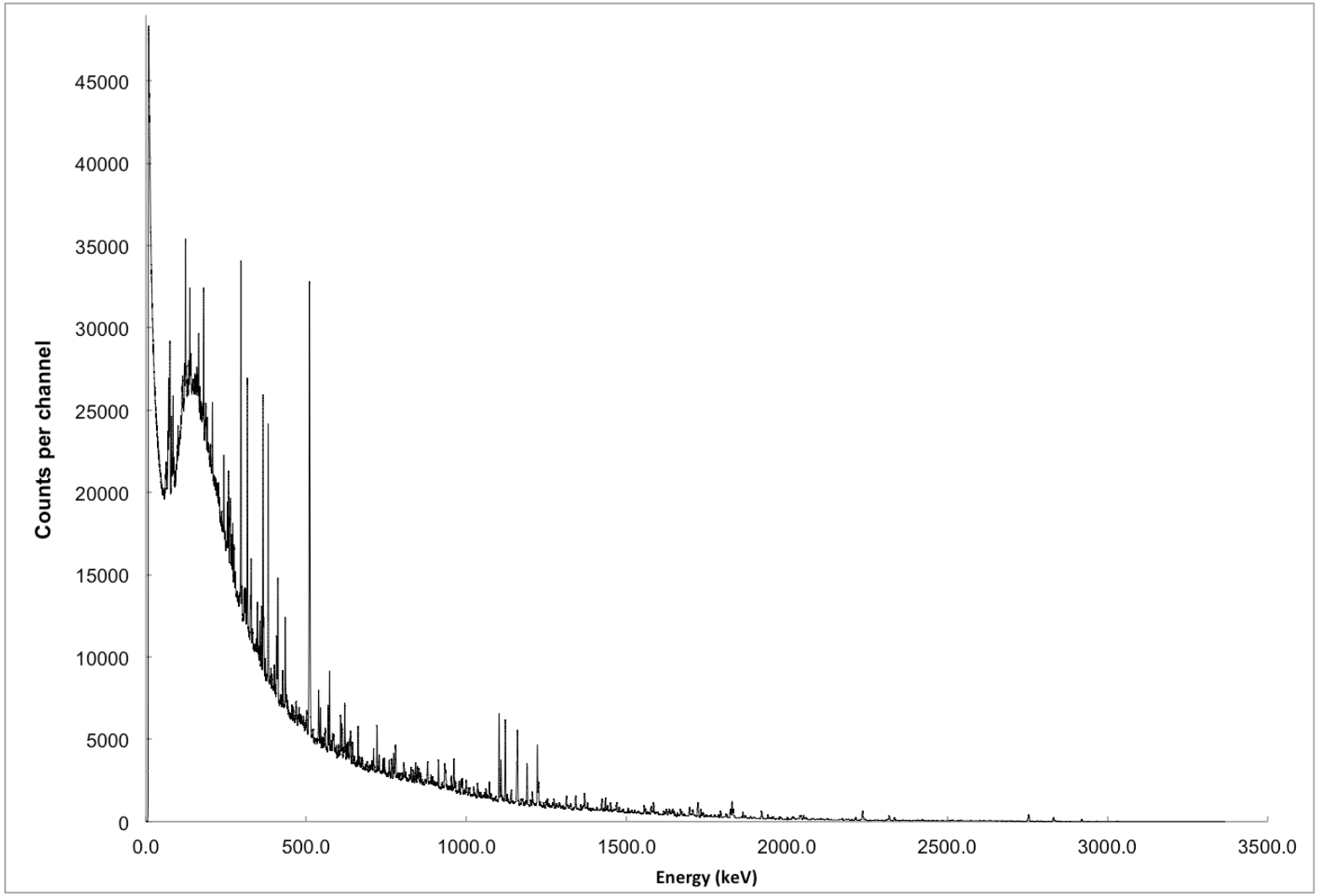

Figure C-4: Mercury Target Hg-2 Gamma Spectra, Data Set #2

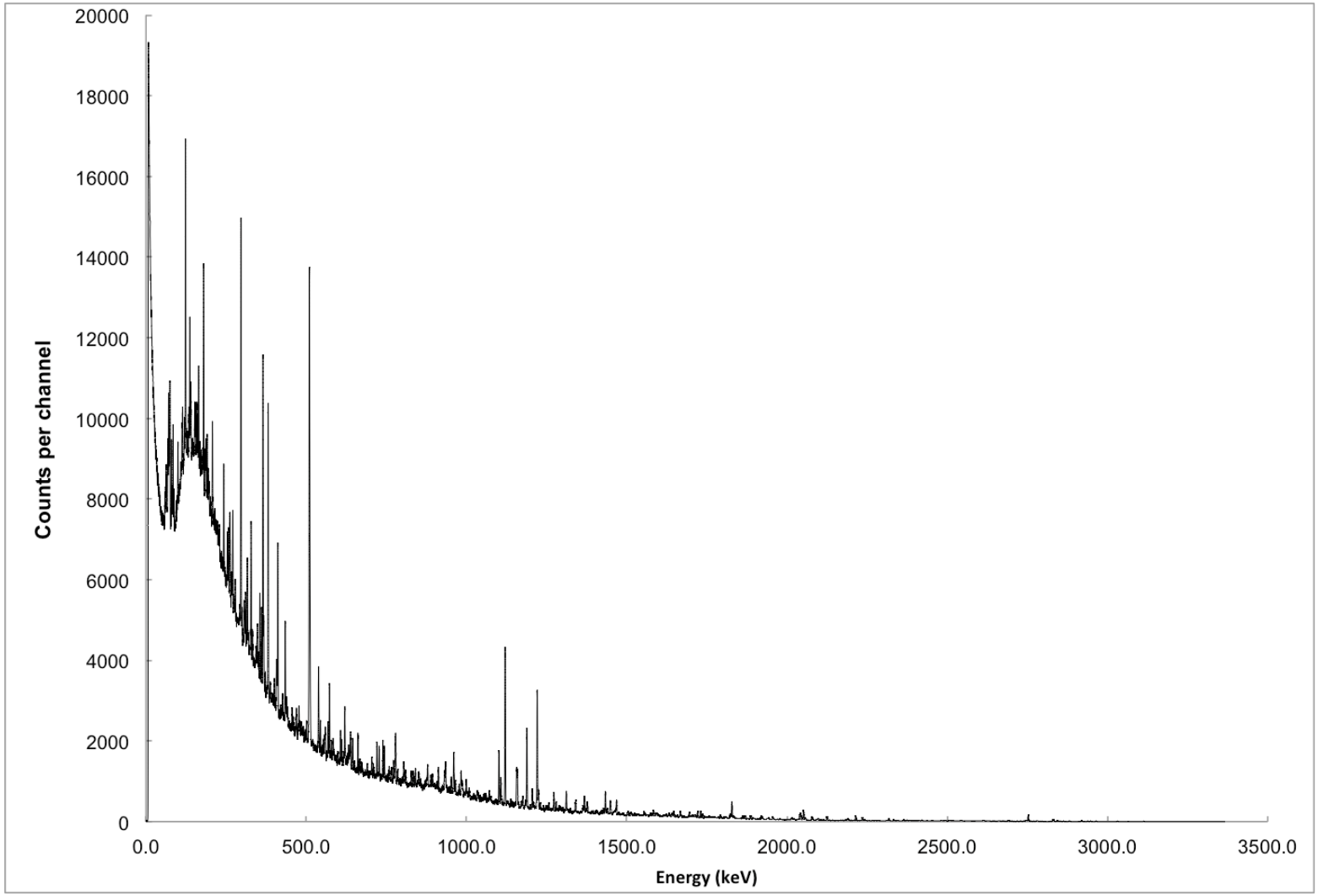

Figure C-5: Mercury Target Hg-1 Gamma Spectra, Data Set #3

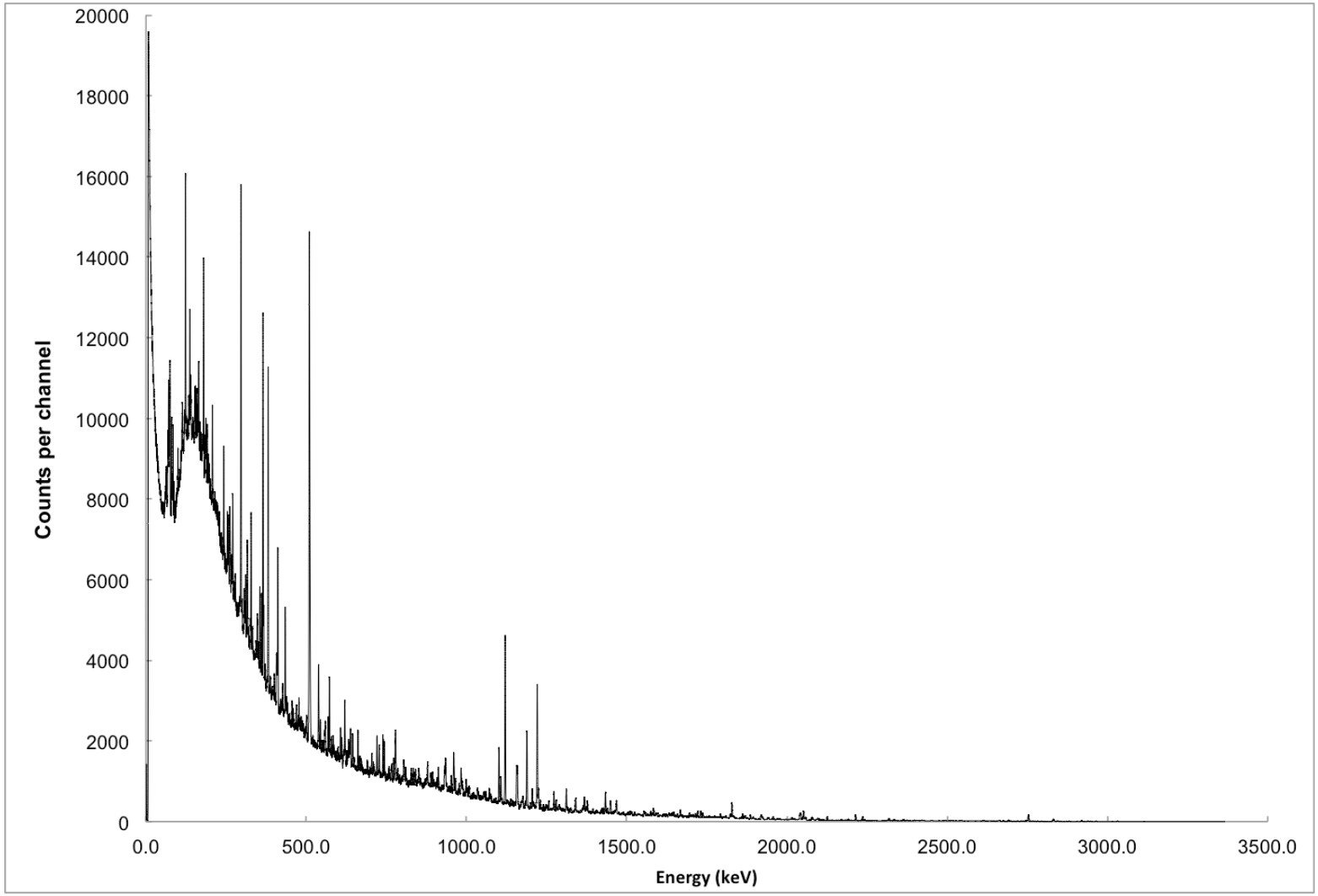

Figure C-6: Mercury Target Hg-2 Gamma Spectra, Data Set #3

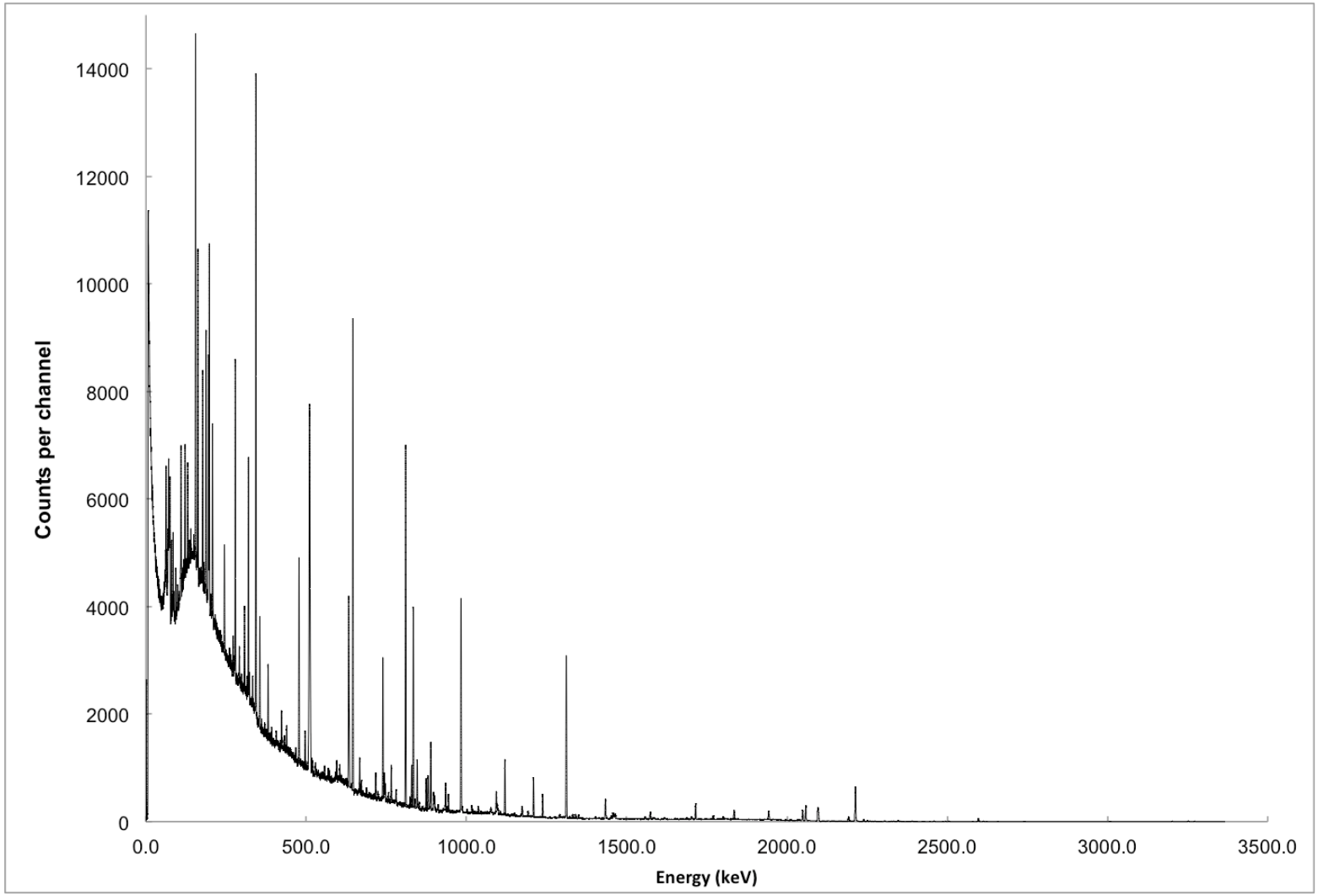

Figure C-7: Mercury Target Hg-1 Gamma Spectra, Data Set #4

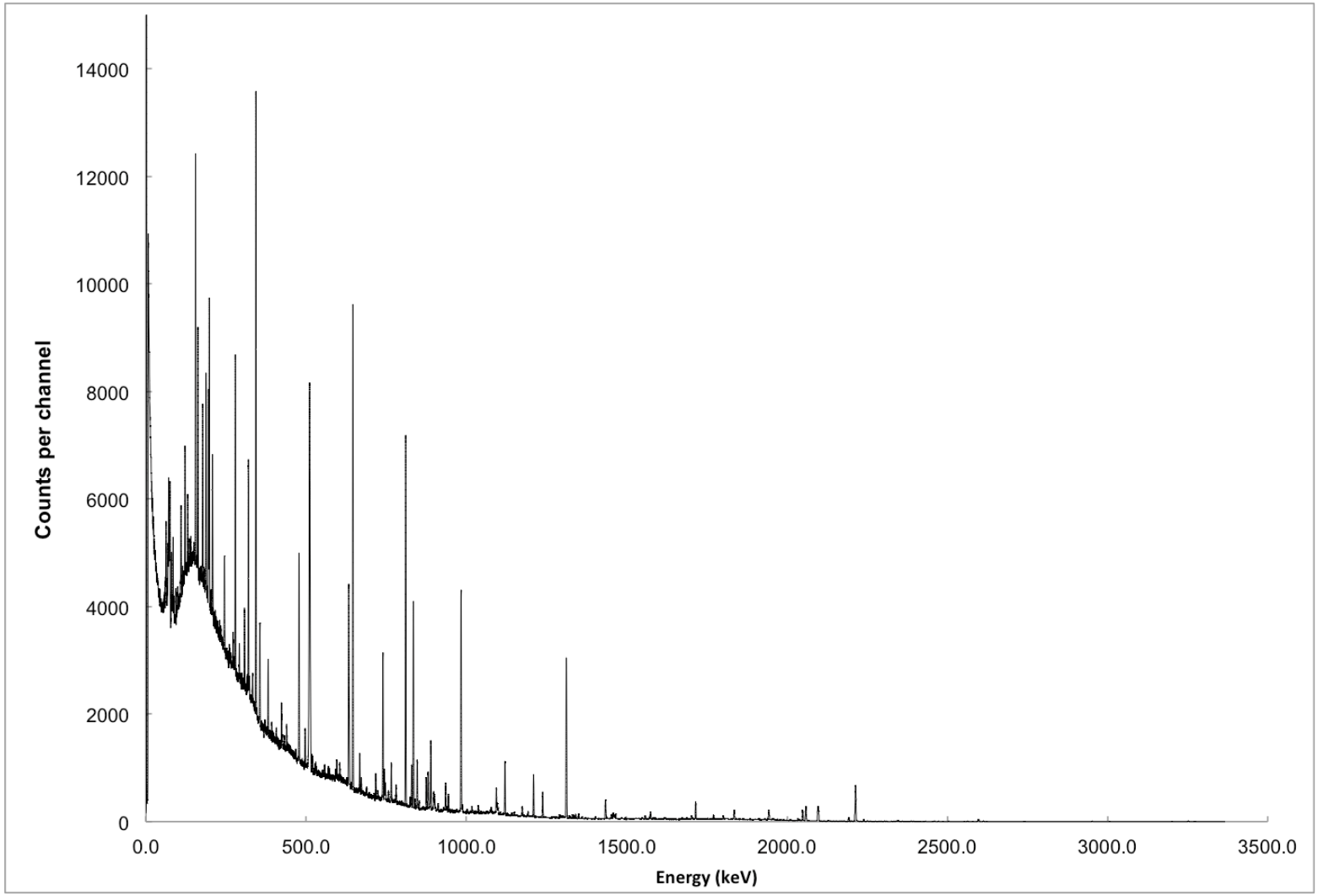

Figure C-8: Mercury Target Hg-2 Gamma Spectra, Data Set #4

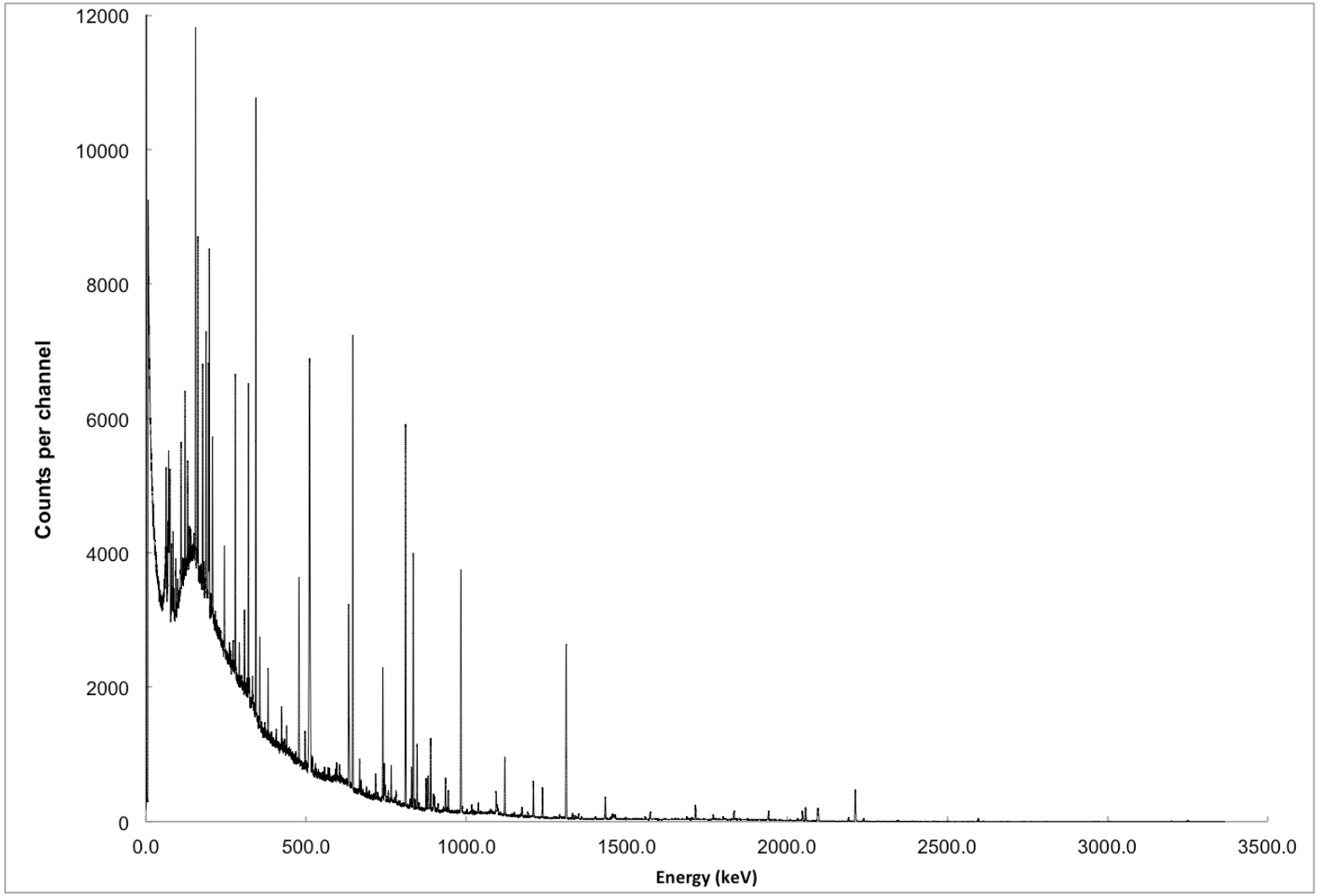

Figure C-9: Mercury Target Hg-1 Gamma Spectra, Data Set #5

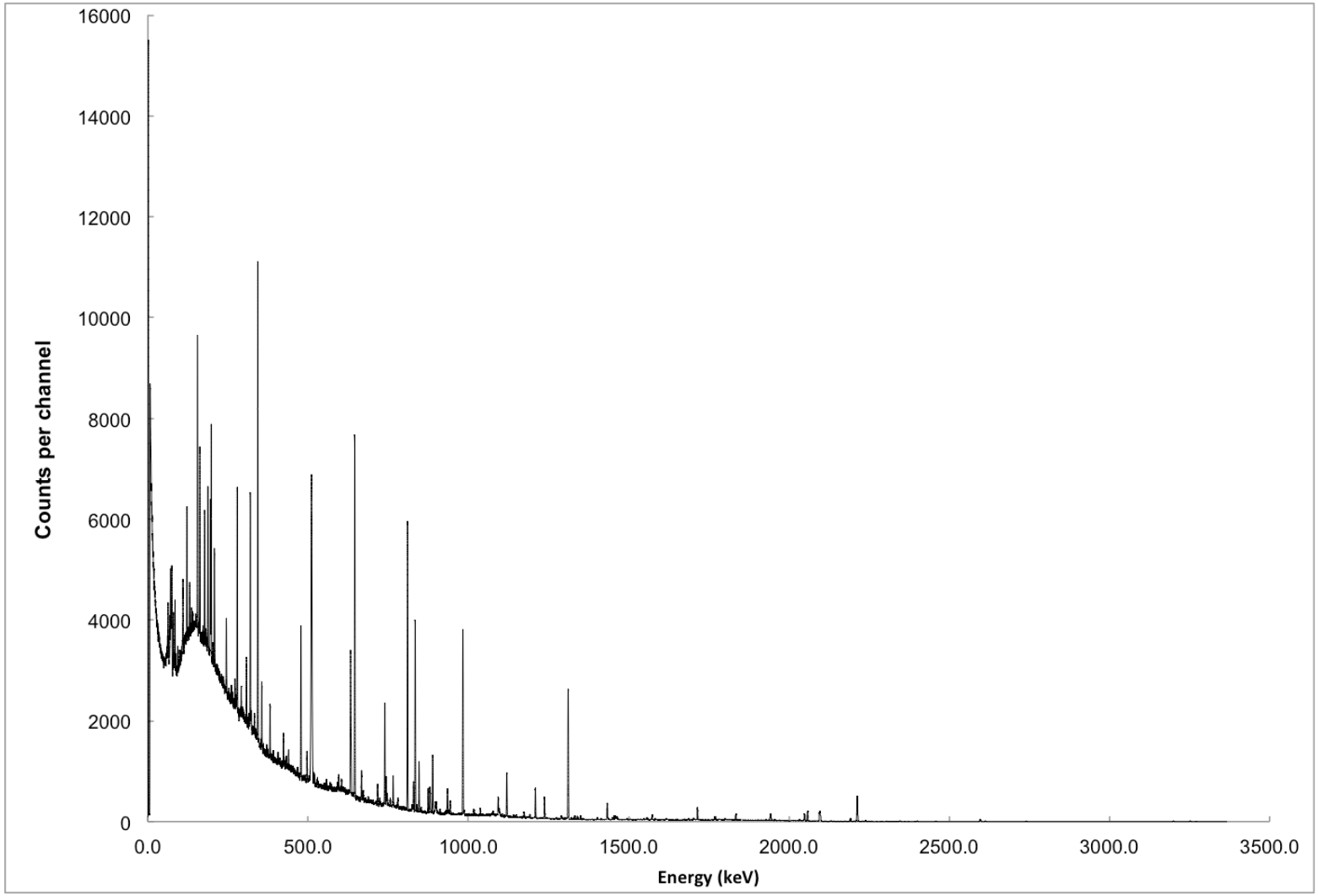

Figure C-10: Mercury Target Hg-2 Gamma Spectra, Data Set #5

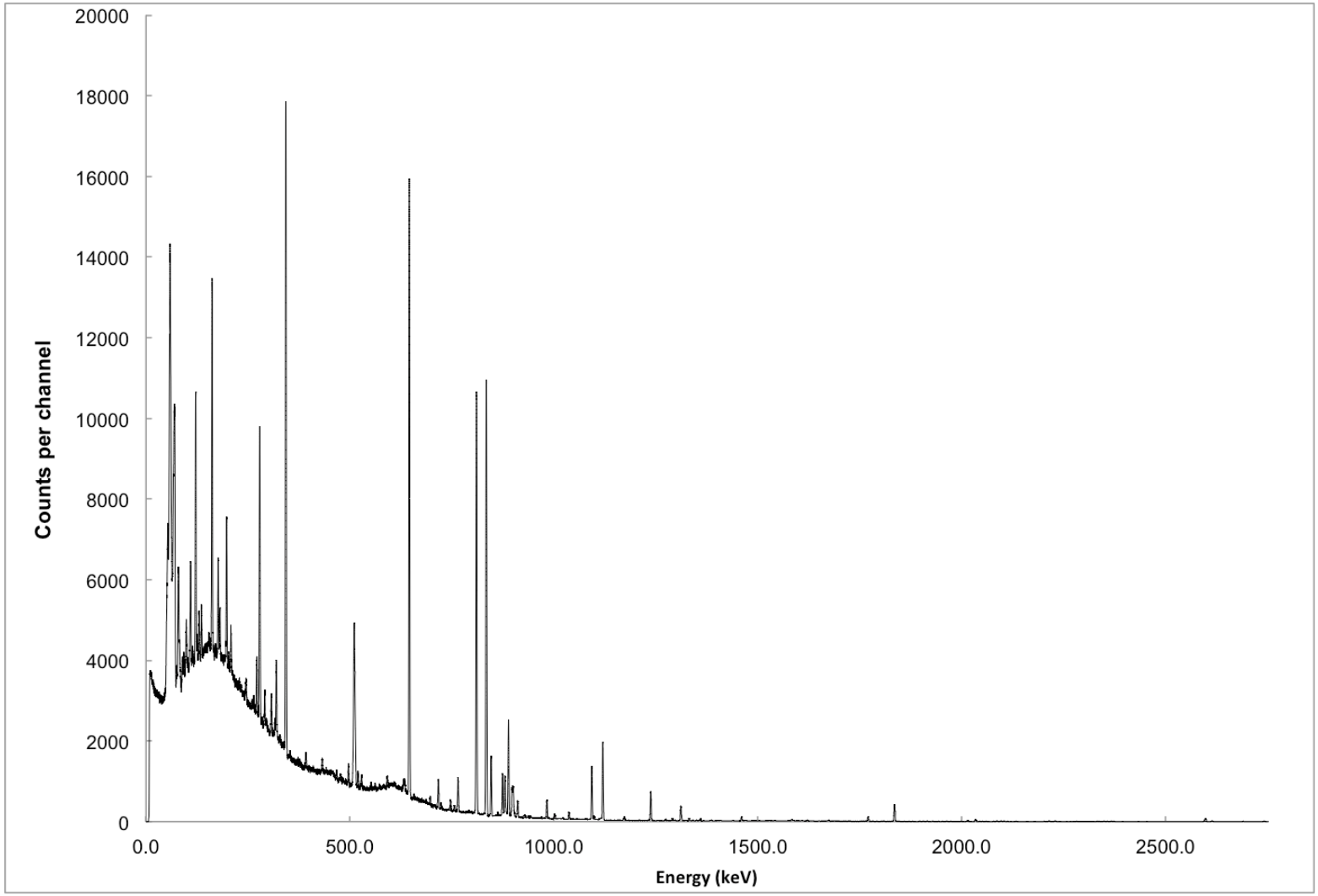

Figure C-11: Mercury Target Hg-1 Gamma Spectra, Data Set #6

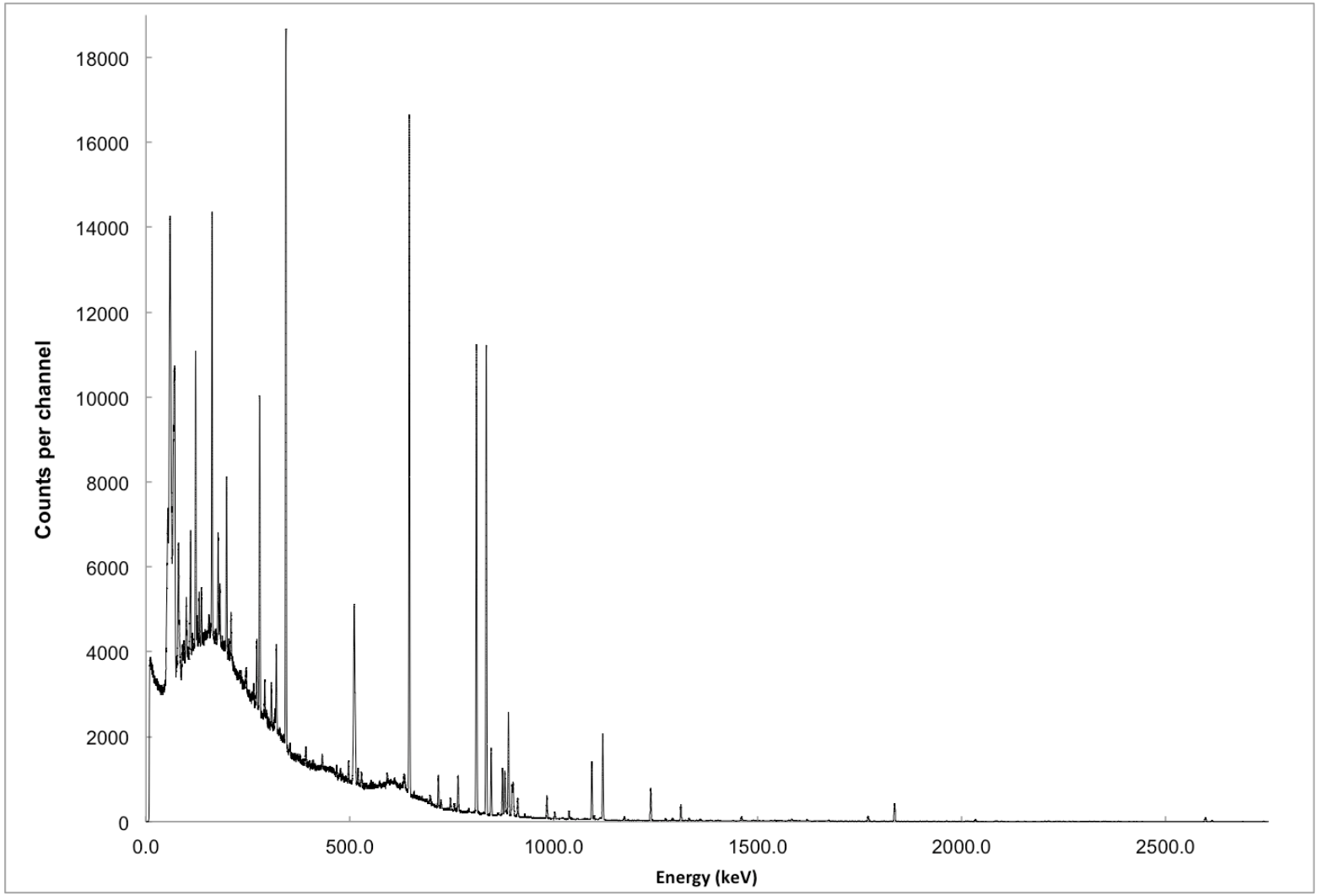

Figure C-12: Mercury Target Hg-2 Gamma Spectra, Data Set #6

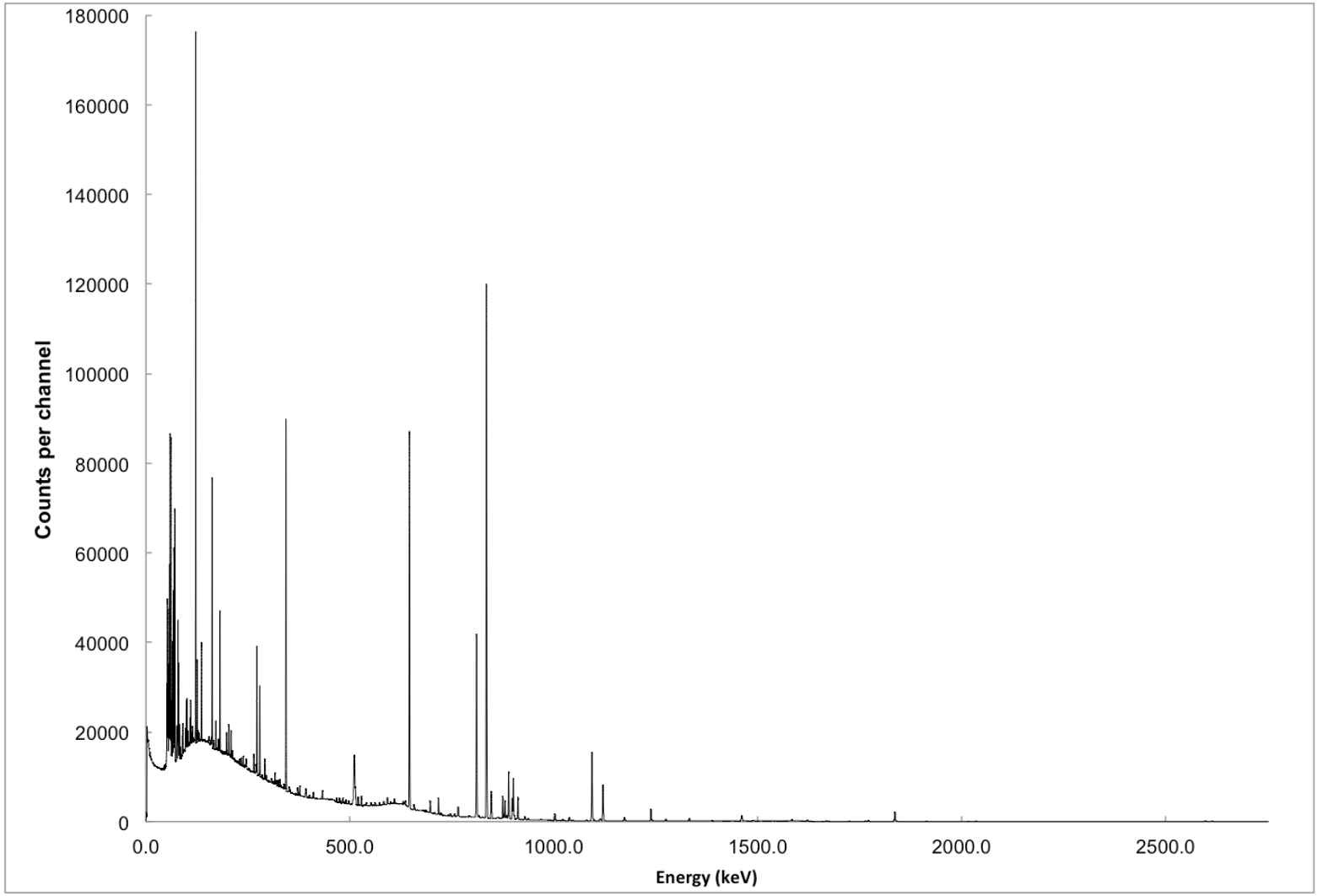

Figure C-13: Mercury Target Hg-1 Gamma Spectra, Data Set #7

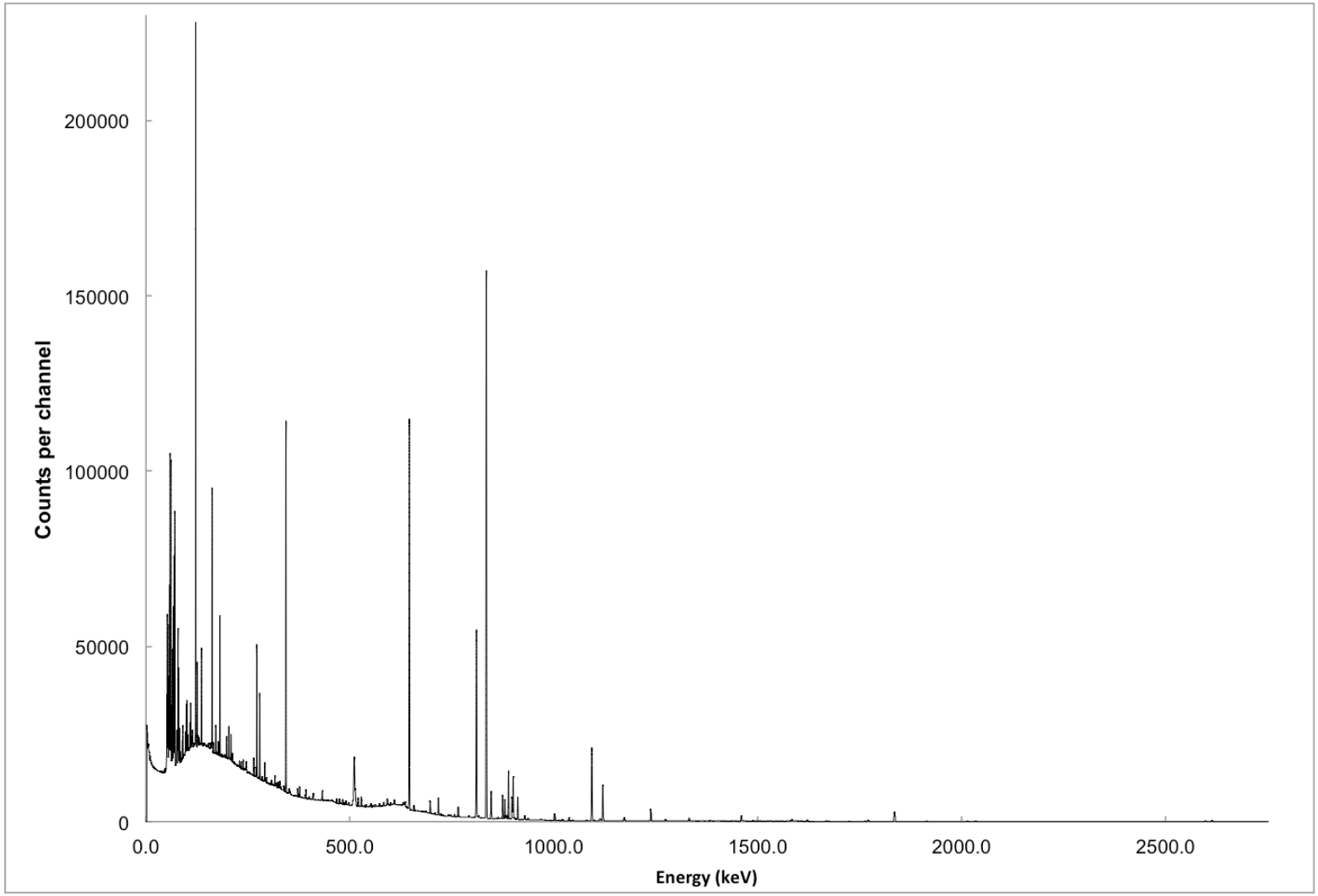

Figure C-14: Mercury Target Hg-2 Gamma Spectra, Data Set #7

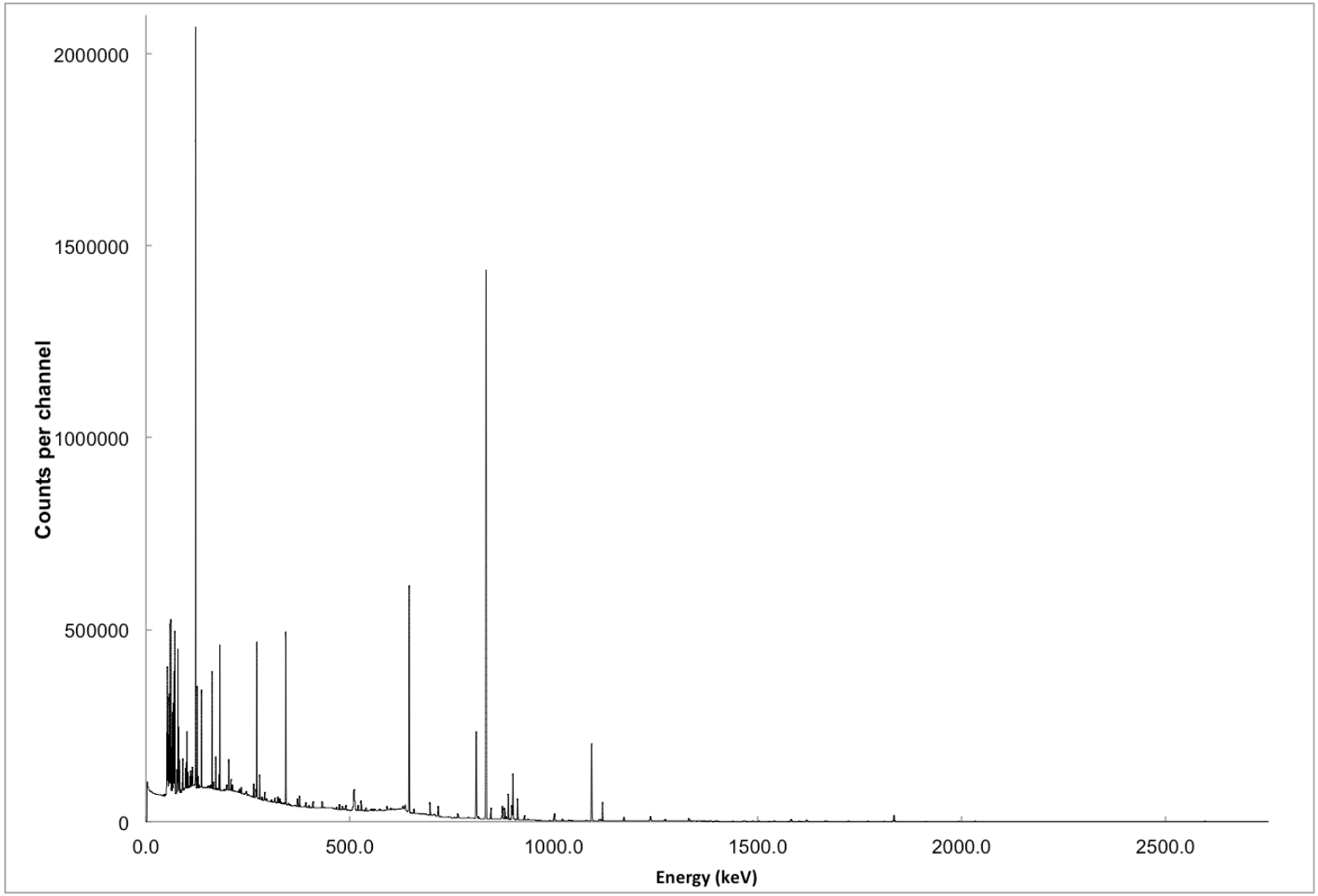

Figure C-15: Mercury Target Hg-1 Gamma Spectra, Data Set #8

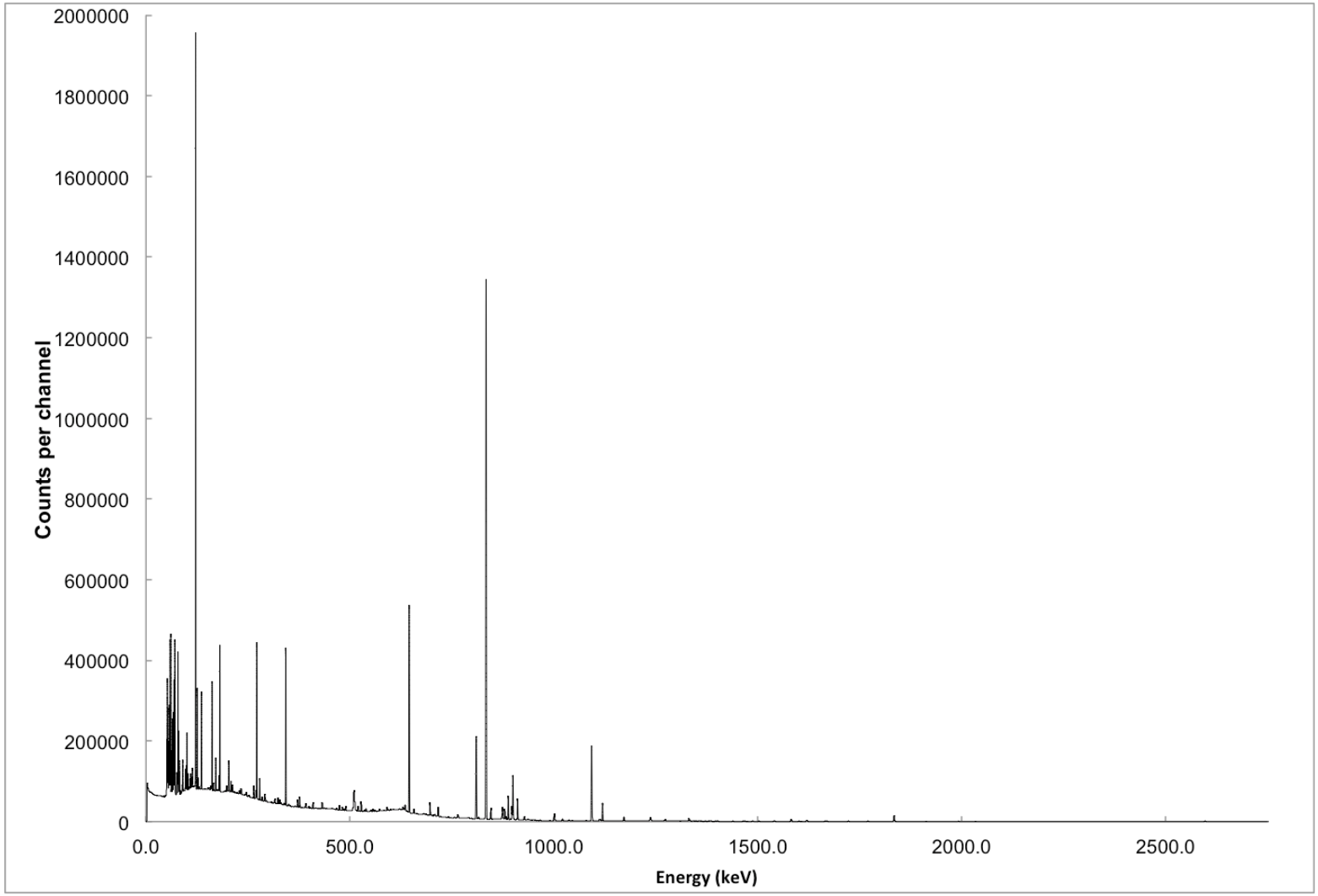

Figure C-16: Mercury Target Hg-2 Gamma Spectra, Data Set #8

APPENDIX D:

Gamma Spectroscopy Efficiency Curves

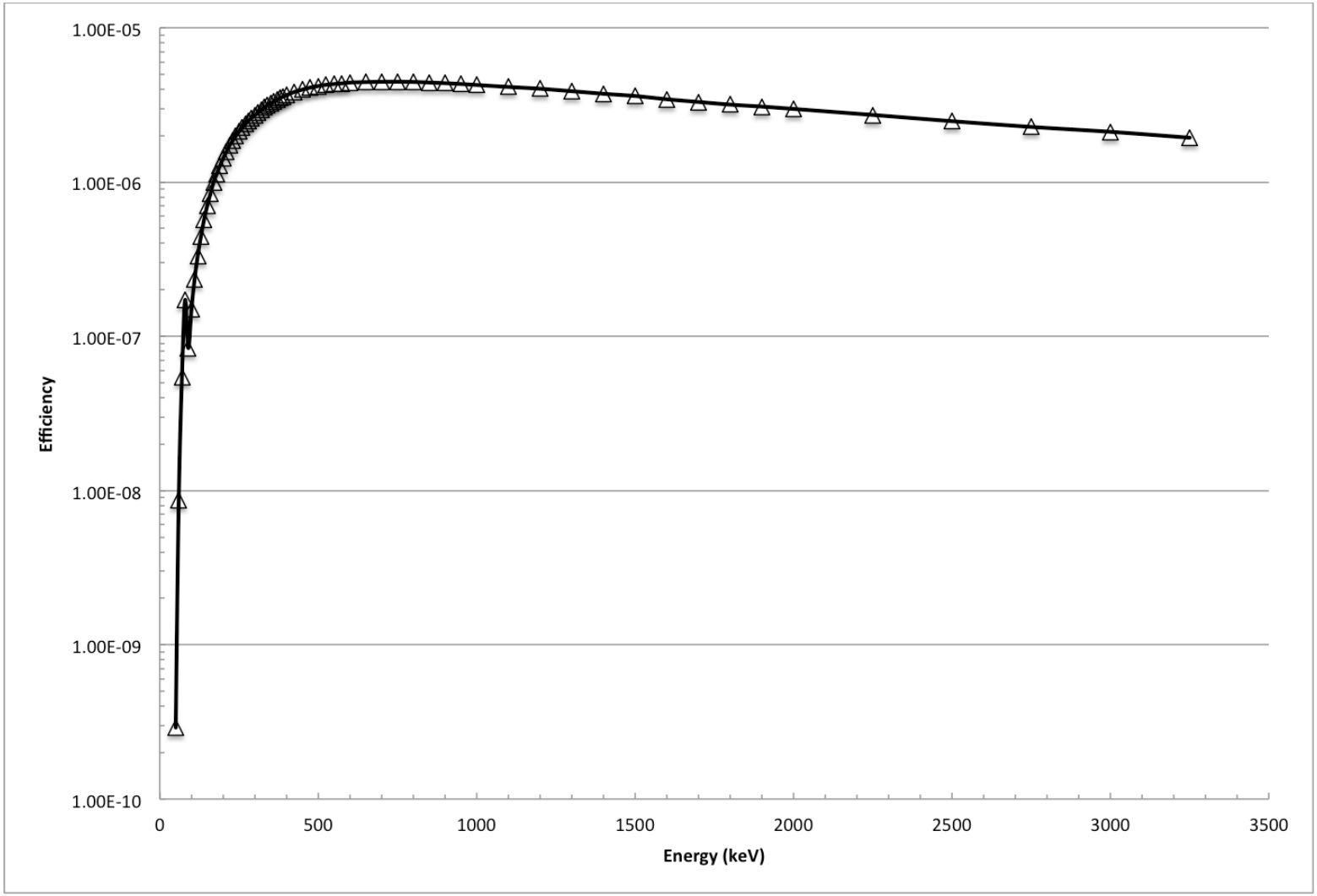

Figure D-1: MCNP efficiency calculation, Geometry #1

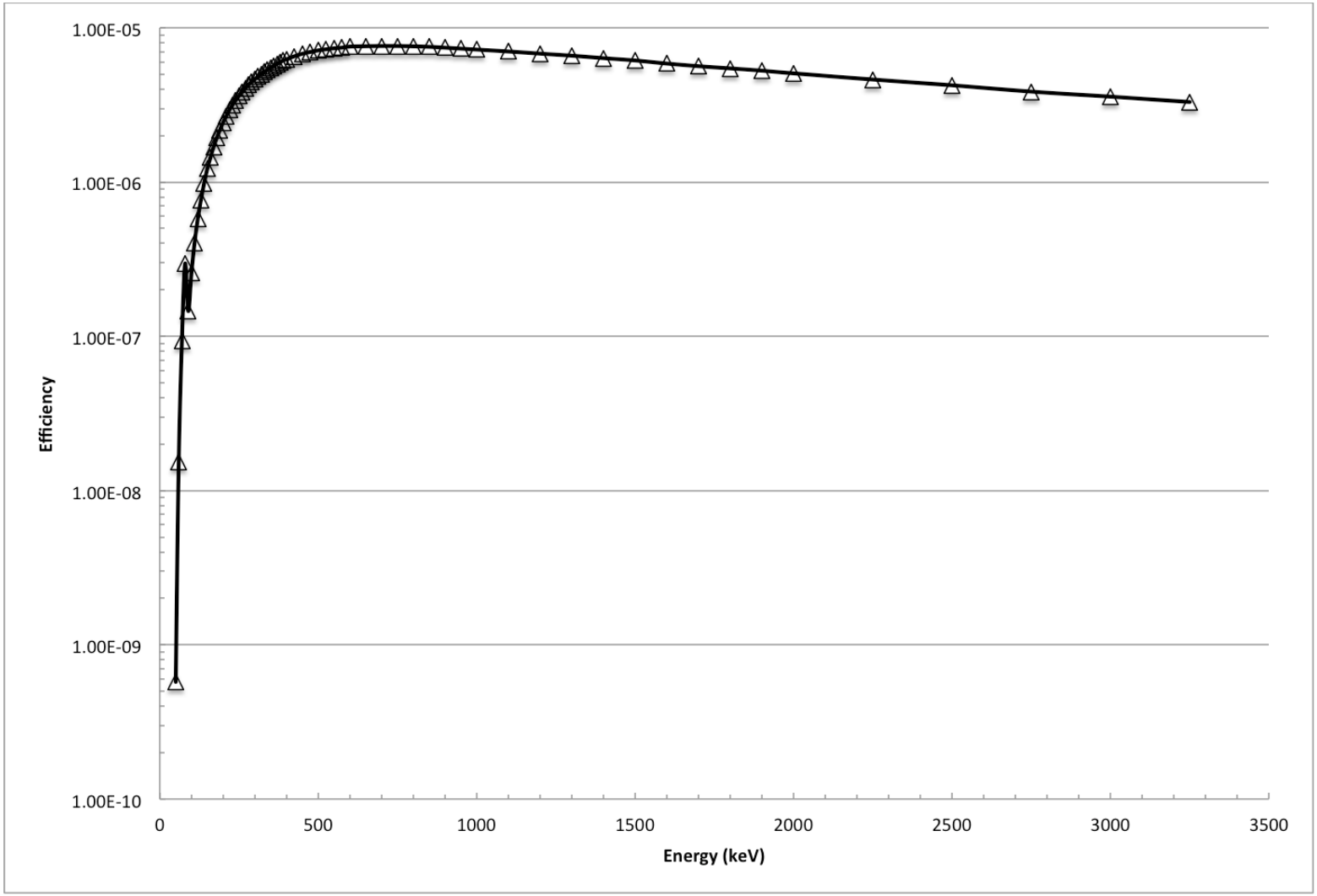

Figure D-2: MCNP efficiency calculation, Geometry #2

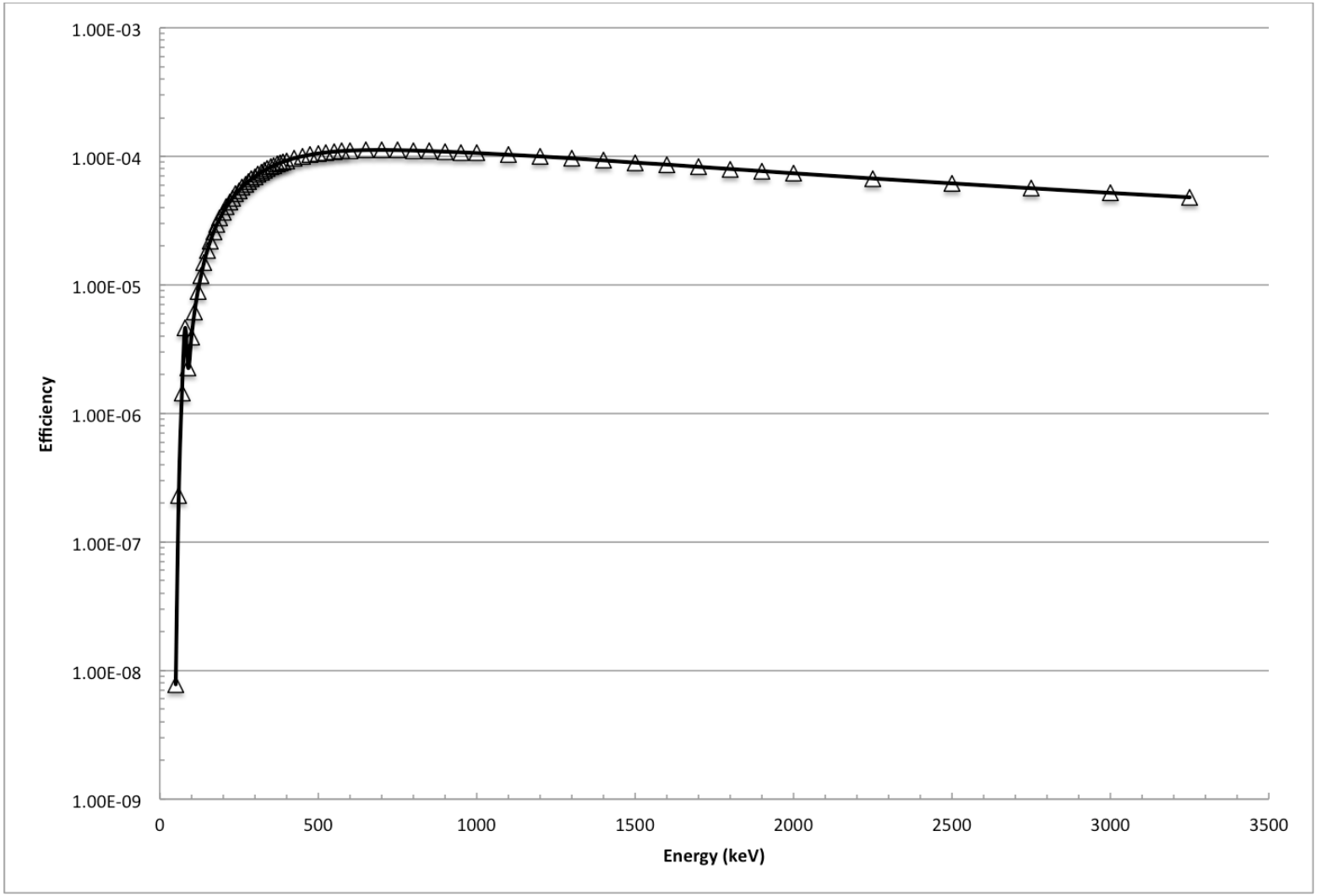

Figure D-3: MCNP efficiency calculation, Geometry #3

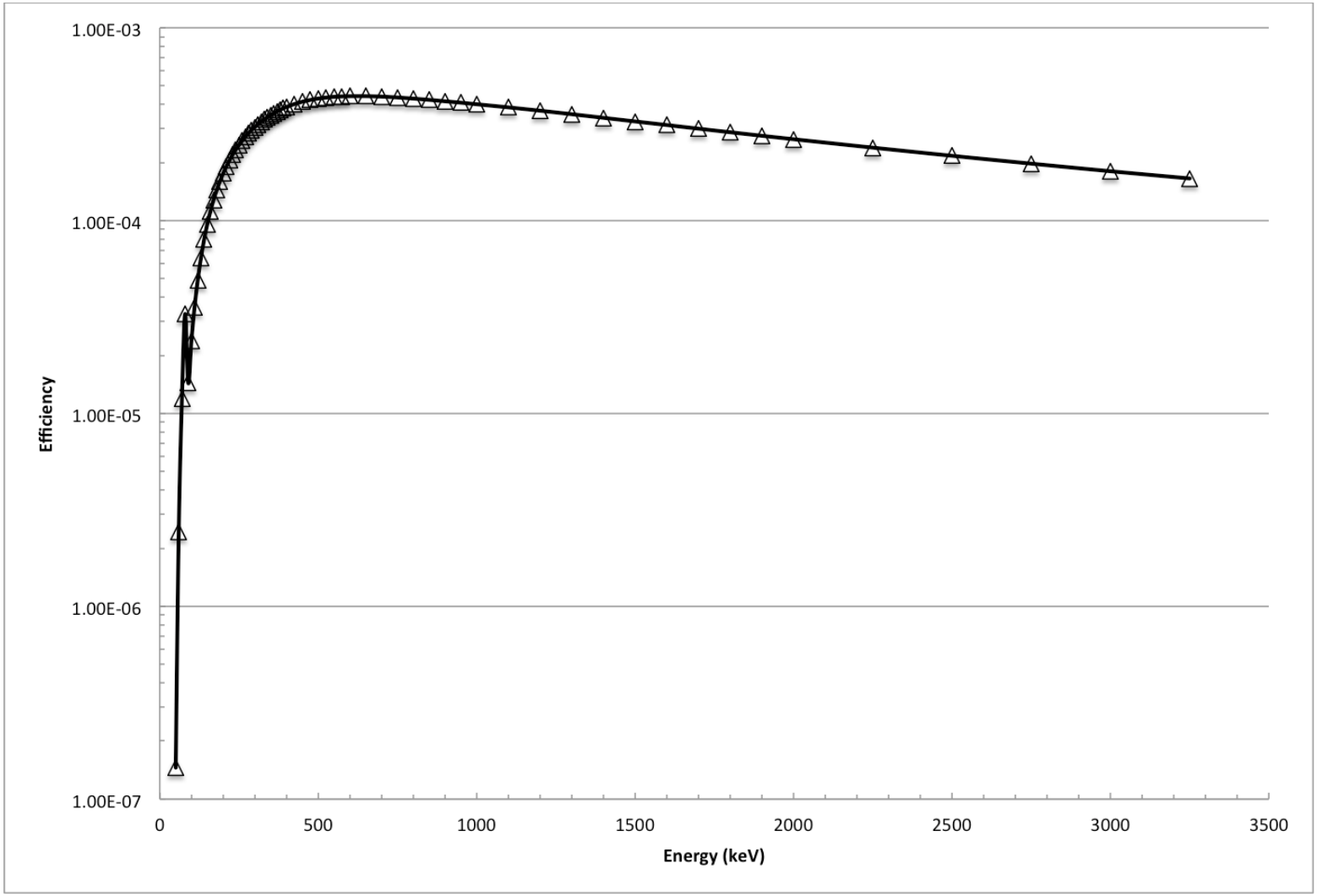

Figure D-4: MCNP efficiency calculation, Geometry #4

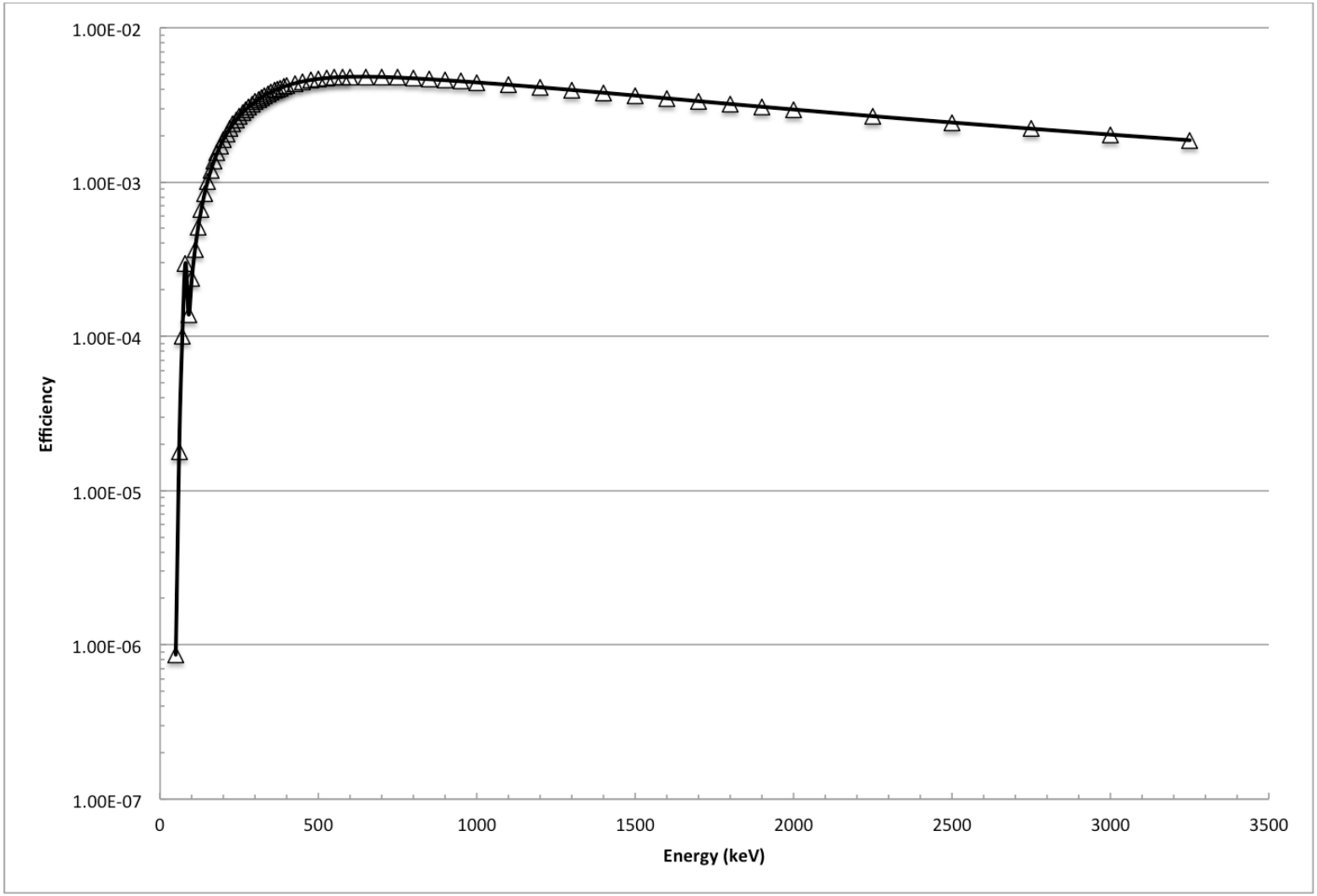

Figure D-5: MCNP efficiency calculation, Geometry #5

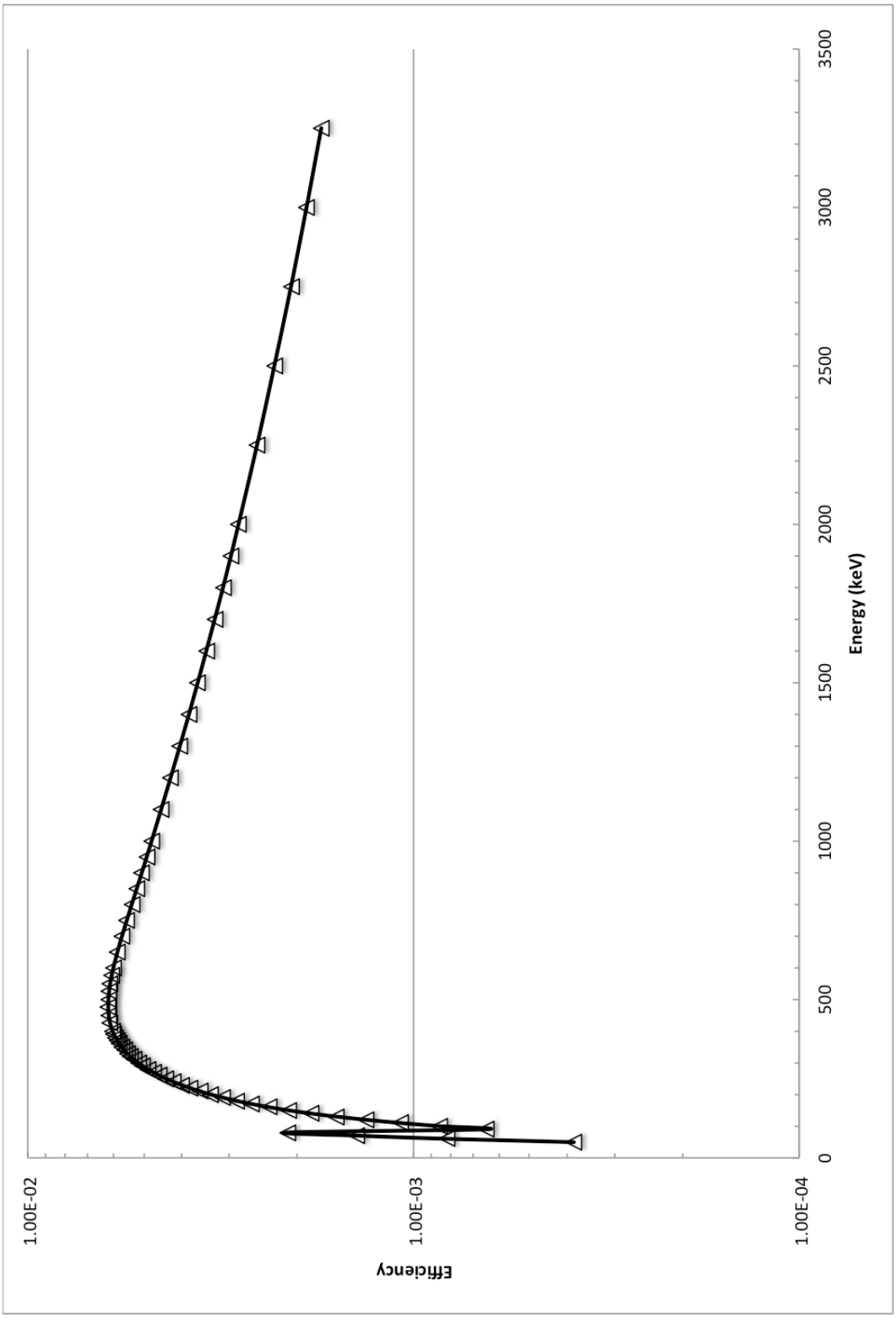

Figure D-6: MCNP efficiency calculation, Geometry #6

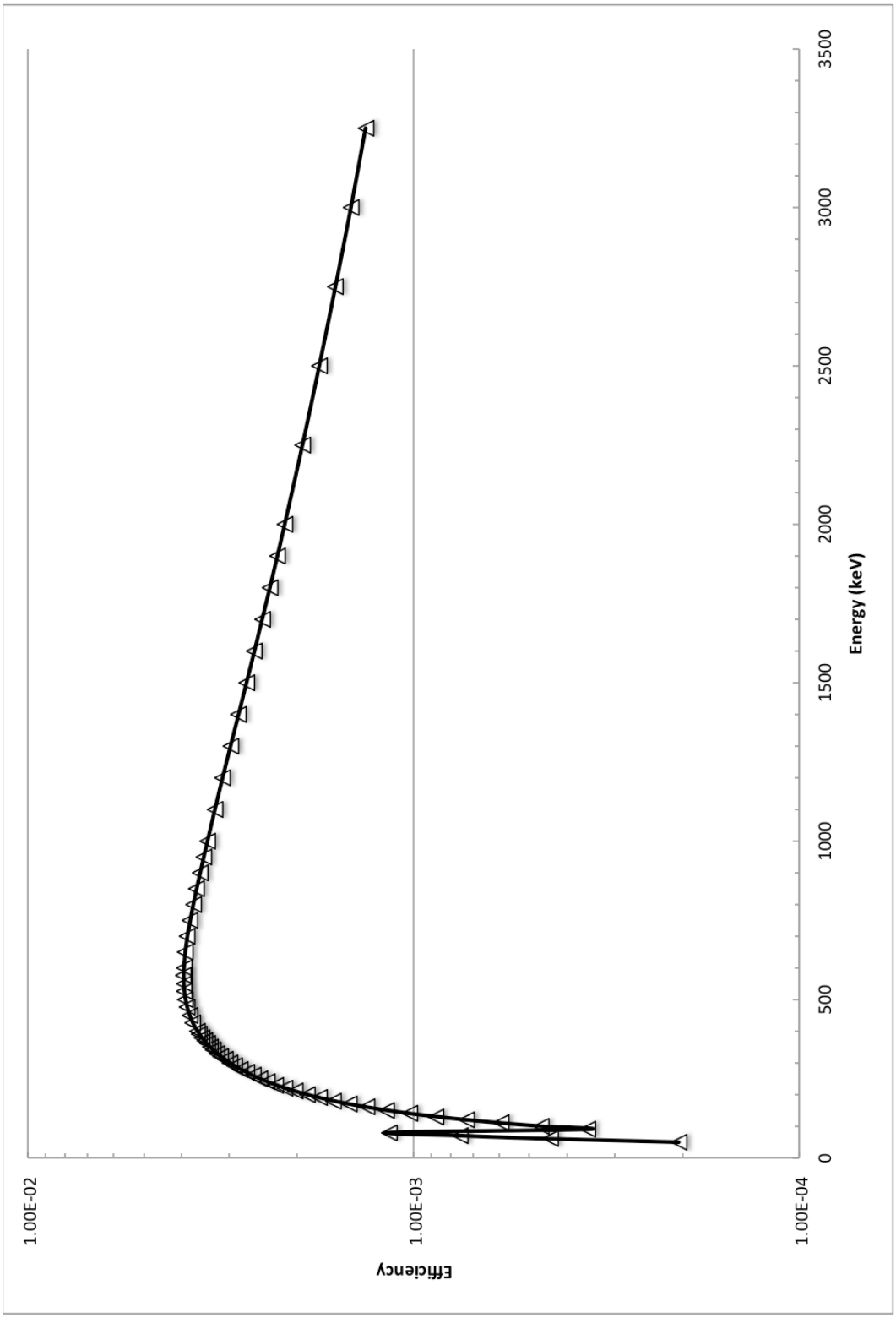

Figure D-7: MCNP efficiency calculation, Geometry #7

APPENDIX E:

MCNPX Input Files

MCNPX input file for calculation of spallation residual cross sections and development of gamma spectroscopy data libraries.

```
c message: DATAPATH=/home/fcg/mcnpx/data4
c
c - Target Cells
1 5 -13.53 32 -33 -30
2 4 -7.96 34 -32 -30
3 4 -7.96 33 -35 -30
4 4 -7.96 32 -33 30 -31
5 4 -7.96 36 -32 30 -31
6 4 -7.96 33 -37 30 -31
c
c - Container Cells
10 4 -7.96 -50
11 4 -7.96 -51
12 4 -7.96 -52
13 4 -7.96 -53
14 3 -0.001293 #1 #2 #3 #4 #5 #6 #11 #10 #12 #13 -55
15 6 -.92 -56 55
16 4 -7.96 -57
c
c - Other Structures
20 6 -.92 -70 $ Poly Block
21 8 -.387 -71 $ Wood Table
22 7 -11.4 -72 $ lead rows 1-3
23 7 -11.4 -73 $ lead row 4
24 7 -11.4 -74 $ lead row 5
97 3 -0.001293 74 73 72 71 70 57 56 -999
99 0 999

C - Target Surfaces
30 cz 3.175
31 cz 5.700
32 pz 0.00
33 pz 1.73
34 pz -0.33
35 pz 2.06
36 pz -1.73
37 pz 3.46
c
c - Container Surfaces
50 rpp -3.81 3.81 -6.404 -3.2 -2.376 -1.73
51 rpp -3.81 3.81 -7.05 -6.404 -6.805 -1.73
52 rpp -3.81 3.81 -6.404 -3.2 3.46 4.106
53 rpp -3.81 3.81 -7.05 -6.404 3.46 8.535
55 rpp -13.6144 13.6144 -7.05 19.6708 -19.9884 21.7184
56 rpp -13.97 13.97 -7.4056 20.0264 -20.344 22.074
57 rpp -3.81 3.81 -8.0406 -7.4056 -6.805 8.535
c
c - other surfaces
c
70 rpp -13.97 23.8125 -18.2006 -8.0406 -20.5 17.2825
71 rpp -47.295 54.305 -22.0106 -18.2006 -43.18 43.18
72 rpp 23.8125 33.9725 -18.2006 -2.9606 -43.18 38.1
73 rpp 23.8125 33.9725 -2.9606 2.1194 -33.02 38.1
74 rpp 23.8125 33.9725 2.1194 7.1994 17.78 38.1
999 SPH 0 0 0 1000

c - Material 3 NIST Air (density=1.23E-2 g/cc)
m3 8016 -.232 7014 -.755 6012 -1.2e-4 18000 -1.28e-2
c
```

```
c - Material 4 Stainless Steel 316 (density=7.96 g/cc)
m4       6000 3.17504E-04
        14000 1.69733E-03
        15031 6.92577E-05
        16032 4.46013E-05
        24000 1.55858E-02
        25055 1.73543E-03
        26000 5.57795E-02
        28000 9.74726E-03
        42000 1.24231E-03
c
c - Material 5 Mercury (density=13.53g/cc)
m5      80000 4.06196E-02
c
c - Material 6 Polyethylene-scaleman (density-.92 g/cc)
m6    6012 2 1001 3
c - Material 7 Lead (density - 11.4)
m7    82000 1
c
c - Material 8 wood - redwood scaleman (density-.387)
m8     6000 6 1001 10 8016 5
c
c
sdef    y=d1 x=d2 z=-50 erg=800 vec=0 0 1 dir=1 par=1
sp1     -41 0.70645 0
sp2     -41 0.70645 0
c
c
f4:n 1 2 3 4 5 6
e4     5.000e-09 1.000e-08 1.500e-08 2.000e-08 2.500e-08
       3.000e-08 3.500e-08 4.200e-08 5.000e-08 5.800e-08 6.700e-08
       8.000e-08 1.000e-07 1.520e-07 2.510e-07 4.140e-07 6.830e-07
       1.125e-06 1.855e-06 3.059e-06 5.043e-06 8.315e-06 1.371e-05
       2.260e-05 3.727e-05 6.144e-05 1.013e-04 1.670e-04 2.754e-04
       4.540e-04 7.485e-04 1.234e-03 2.035e-03 2.404e-03 2.840e-03
       3.355e-03 5.531e-03 9.119e-03 1.503e-02 1.989e-02 2.554e-02
       4.087e-02 6.738e-02 1.111e-01 1.832e-01 3.020e-01 3.887e-01
       4.979e-01 0.639279  0.82085   1.10803   1.35335   1.73774   2.2313
       2.86505   3.67879   4.96585   6.065     10.00     14.9182   16.9046
       20.0      25.0
c
c MODE n
MODE   h n p d t s a / z *
imp:h  1 1 1 1 1 1 1 0 *
imp:n  1 1 1 1 1 1 1 1 1 1 1 1 1 1 1 1 1 1  0
imp:p  1 1 1 1 1 1 1 0 *
imp:d  1 1 1 1 1 1 1 0 *
imp:t  1 1 1 1 1 1 1 0 *
imp:s  1 1 1 1 1 1 1 0 *
imp:a  1 1 1 1 1 1 1 0 *
imp:/  1 1 1 1 1 1 1 0 *
imp:z  1 1 1 1 1 1 1 0 *
phys:h  2000 *
phys:n  2000 3j 20
phys:p  2000 *
phys:/  2000 *
phys:z  2000 *
nps     1E10
print
lost  60  60
c prdmp  j -15 j 1 *
c dbcn  893452385093405 3j 12000 2j *
activ cinder 1 2 3 4 5 6 *
```

MCNPX input file for calculation of HPGe efficiency (Geometry #1, Energy 60 keV)

```
c This file models the GEM-15190-P HPGe detector (SN: 33-TP30846)
c The dead layer on top of the crystal is much thicker than specified in the
c manual, the distance between the crystal and Al can is also adjusted
c detector model created by Z. Wang Ph.D Thesis 2006
c Additonal model details by D. Blaylock
c
c - Detector Model Cells
c
1 1 -5.23 6 5 -3 -7 -4 9 imp:p=1 $ Ge layer top
2 0 -8 -7 5 6 4 imp:p=1
3 1 -5.23 (1 -8 -7 )#1 #2 #8 imp:p=1 $ detector
4 1 -5.23 (-2 7 -5 ):(5 7 -4 ) imp:p=1 $ Ge dead layer
5 1 -5.23 1 -3 8 -6 imp:p=1 $ Ge dead layer around side
6 2 -2.7 1 -10 3 -2 imp:p=1
7 0 (-3 8 4 6 5 -2 ):(7 -8 -2 4 6 5 ) imp:p=1
8 0 ((-12 -11 13 )):(-12 -13 1 ) imp:p=1 $ central hole
9 2 -2.7 -15 14 imp:p=1
10 0 ((-14 10 ):(-14 2 ))#11 #14 imp:p=1
11 2 -0.534 -20 2 -10 imp:p=1 $ Mylar
12 0 21 -1 -3 imp:p=1
13 2 -2.7 22 -21 -3 imp:p=1
14 2 -2.7 22 -1 3 -10 imp:p=1
c
c - Target Cells
20 5 -13.53 32 -33 -30 imp:p=1
21 4 -7.96 34 -32 -30 imp:p=1
22 4 -7.96 33 -35 -30 imp:p=1
23 4 -7.96 32 -33 30 -31 imp:p=1
24 4 -7.96 36 -32 30 -31 imp:p=1
25 4 -7.96 33 -37 30 -31 imp:p=1
c
c - Enclosure wall cells
30 6 -1.3 50 -51 52 -53 54 -55 imp:p=1
c
998 3 -0.00128 (-999 15) #20 #21 #22 #23 #24 #25 #30 imp:p=1 $ air
999 0 999 imp:p=0

c - Detector Surfaces
1 pz 0
2 pz 6.40
3 cz 2.355
4 tz 0 0 5.88 1.72 0.65 0.65
5 cz 2.12
6 pz 5.99
7 pz 6.243
8 cz 2.275
9 tz 0 0 5.88 1.72 0.56 0.56
10 cz 2.431
11 sz 4.5 0.52
12 cz 0.432
13 pz 4.5
14 rcc 0 0 -3 0 0 10.00 2.931
15 rcc 0 0 -3 0 0 10.13 3.061
20 pz 6.455
21 pz -2.68
22 pz -3.00
c
c - Target Surfaces
c
30 c/x 0 -0.475 3.175
```

```
31 c/x 0 -0.475 5.700
32 px 171.4185
33 px 173.1485
34 px 171.0885
35 px 173.4785
36 px 169.6885
37 px 174.8785
c
c - enclosure wall surfaces
50 px 157.0435
51 px 157.3991
52 py -13.97
53 py 13.97
54 pz -12.7
55 pz 12.7
c
999 so 500

mode p
c
c - Material 1 Germanium Crystal (density=5.23 g/cc)
m1 32000. 1
c
c - Material 2 Aluminum (density=2.7 g/cc)
m2 13000. 1
c - Material 3 NIST Air (density=1.23E-2 g/cc)
m3 8016 -.232 7014 -.755 6012 -1.2e-4 18000 -1.28e-2
c
c - Material 4 Stainless Steel 316 (density=7.96 g/cc)
m4       6000 3.17504E-04
        14000 1.69733E-03
        15031 6.92577E-05
        16032 4.46013E-05
        24000 1.55858E-02
        25055 1.73543E-03
        26000 5.57795E-02
        28000 9.74726E-03
        42000 1.24231E-03
c
c - Material 5 Mercury (density=13.53g/cc)
m5      80000 4.06196E-02
c
c - Material 6 PVC-scaleman (density-1.3 g/cc)
m6    6012 2 1001 3 17035 1
c
c - Source defination
sdef par=2 erg=.06 cell=20 pos=171.4186 0 -.475 rad=d1 ext=d2 axs=1 0 0
si1 3.174
si2 1.728
c
c - Tally Cards
e8 0 8191i 3.3675
f8:p 3
c e18 0 8191i 3.3675
c f18:p 3
c ft18 geb 9.374e-4 5.202e-4 0.75967
nps 2e11
print
```

MCNPX input file for calculation of HPGe efficiency (Geometry #4, Energy 50 keV)

```
c Model of BEGE 5030 HPGe detector (SN09088378)
c Last Edit 9/26/2012 (by D. Blaylock)
c LANSCE Irradiated target at 7 3/16" above detector surface
c
c - Detector Model Cells
c
1 1 -5.23 -1 imp:p=1                                $ Ge
2 1 -5.23 1 -2 imp:p=1                              $ Ge (dead layer)
3 0  2 -3 imp:p=1                                   $ Vacuum in Detector
4 2 -2.7 -4 3 5  imp:p=1                            $ Al Wall
5 6 -1.41 -5 #1 #2 #3 #4 imp:p=1                    $ Carbon Window
6 3 -0.001293 -6 #1 #2 #3 #4 #5 #7 imp:p=1          $ air above detector
7 2 -2.7 5 -7 6 5 4 imp:p=1           $ Al Ring
8 3 -0.001293 -999 4 7 6 #20 #21 #22 #23 #24 #24 #25 imp:p=1
c
c - Target Cells
20 5 -13.53 32 -33 -30 imp:p=1
21 4 -7.96 34 -32 -30 imp:p=1
22 4 -7.96 33 -35 -30 imp:p=1
23 4 -7.96 32 -33 30 -31 imp:p=1
24 4 -7.96 36 -32 30 -31 imp:p=1
25 4 -7.96 33 -37 30 -31 imp:p=1
c
c
999 0 999 imp:p=0

c - Detector Surfaces
1 rcc 0 0 0.295 0 0 2.6675 3.9875          $ Ge
2 rcc 0 0 0 0 0 3.00 4.025              $ Ge (dead layer)
3 rcc 0 0 0 0 0 3.5 4.93                  $ Vacuum Gap
4 rcc 0 0 0 0 0 3.56 5.08                 $ Al wall
5 rcc 0 0 3.5 0 0 0.06 4.93               $ Carbon Window
6 rcc 0 0 3.56 0 0 0.16 4.1275            $ Air above window
7 rcc 0 0 3.56 0 0 0.16 5.08              $ Al ring
c
c - Target Surfaces
c
30 cz 3.175
31 cz 5.700
32 pz 23.70625
33 pz 25.43625
34 pz 23.37625
35 pz 25.76625
36 pz 21.97625
37 pz 27.16625
c
999 so 500

mode p
c
c - Material 1 Germanium Crystal (density=5.23 g/cc)
m1 32000. 1
c
c - Material 2 Aluminum (density=2.7 g/cc)
m2 13000. 1
c - Material 3 NIST Air (density=1.23E-2 g/cc)
m3 8016 -.232 7014 -.755 6012 -1.2e-4 18000 -1.28e-2
c
c - Material 4 Stainless Steel 316 (density=7.96 g/cc)
m4       6000 3.17504E-04
        14000 1.69733E-03
        15031 6.92577E-05
```

```
        16032 4.46013E-05
        24000 1.55858E-02
        25055 1.73543E-03
        26000 5.57795E-02
        28000 9.74726E-03
        42000 1.24231E-03
c
c - Material 5 Mercury (density=13.53g/cc)
m5      80000 4.06196E-02
c
c - Material 6 carbon fiber (density-1.41 g/cc e-mail from canberra ISOCS grp)
m6    6012 1
c
c - Source defination
sdef par=2 erg=0.05 cell=20 pos= 0 0 23.706251 rad=d1 ext=d2 axs=0 0 1
si1 3.1749
si2 1.7298
c
c - Tally Cards
e8 0 8191i 3.3675
f8:p 1
c e18 0 8191i 3.3675
c f18:p 1
c ft18 geb 9.374e-4 5.202e-4 0.75967
nps 1e10
print
```

REFERENCES

[1] D. Filges, S. Leray, Y. Yariv, A. Mengon, A. Stanculescu and G. Mank Eds., in *Proceedings of the Joint ICTP-IAEA Advanced Workshop on Model Codes for Spallation Reactions,* IAEA INDC(NDS)-530, Trieste, Italy, 2008

[2] L.S. Waters, Ed., "MCNPX User's Manual, Version 2.5.0," LA-CP-05-0369, 2005

[3] R.E. Prael and H. Lichtenstein, "User Guide to LCS, The LAHET Code System." LANL Report, LA-UR-89-3014, 1989

[4] Hugo W. Bertini, "Low Energy Intranuclear Cascade Calculation," *Physical Review* 131(4), 1963, 1801-1821

[5] Hugo W. Bertini, "Intranuclear-Cascade Calculation of the Secondary Nucleon Spectra from Nucleon-Nucleus Interactions in the Energy Range 340 to 2900 MeV and Comparisons with Experiment." *Physical Review* 188(4), 1969, 1711-1730

[6] R. E. Prael and Michael Bozoian, "Adaptation of the Multistage Preequilibrium Model for the Monte Carlo Method," LANL Report, LA-UR-88-3238, 1988

[7] R. E. Prael, "A Review of Physics Models in the LAHET Code," *Intermediate Energy Nuclear Data: Models and Codes, Proceedings of a Specialists' Meeting*, OECD, 1994, 145

[8] F. Atchison, "Spallation and Fission in Heavy Metal Nuclei under Medium Energy Proton Bombardment," *Targets for Neutron Beam Spallation Sources* Jül-Conf-34, Kernforschungsanlage Jülich GmbH, 1980

[9] W. B. Wilson, S. T. Cowell, T. R. England, A. C. Hayes & P. Moller "A Manual for CINDER'90 Version 07.41 Codes and Data" LANL Report, LA-UR-07-8412, 2008

[10] F. Gallmeier, M Wohlmuther "Activation Script Version 0.5 User Guide" 2007

[11] Y. E. Titarenko, "Experimental and Theoretical Study of the Yields of Residual Product Nuclei Produced in Thin Targets Irradiated by 100-2600 MeV Protons," Technical Report of ISTC 839B-99, 2001.

[12] J. L. Ullmann, A. Gavron, J. King, R. Laird, D. Mayo, L. Waters, C. Zoeller, P.Staples, D. Jagnow, J. Koster, P. W. Lisowski, R. O. Nelson, S. A. Wender, G. Butler, R. Gritzo, M. A. Yates, M. Fowler, J. Wilhelmy, W. Wilson, C. E. Laird, D. H. Mullins, "APT Radionuclide Production Experiment Technical Report," LANL Report LA-UR-95-3327, 1995.

[13] Johanna Sabine Becker, Wolfgang Kerl, Hans-Joachim Dietze, “Nuclide analysis of an irradiated tantalum target of a spallation neutron source using high performance ion chromatography and inductively coupled plasma mass spectrometry," *Analytica Chimica Acta* 387, 1999, 145-154.

[14] S. A. Karamian, J. Adam, D. V. Filossofov, D. Henzlova, V. Henzl, V. G. Kalinnikov, N. A. Lebedev, A. F. Novgorodov, C. B. Collins, I. I. Popescu, C. A. Ur, “Accumulation of the 178m2Hf isomeric nuclei through spallation with intermediate-energy protons of tantalum and rhenium targets," *Nuclear Instruments and Methods in Physics Research A489*, 2002 448-468.

[15] J. Benlliure, P. Armbruster, M. Bernas, A. Boudard, J. P. Dufour, T. Enqvist, R. Legrain, S. Leray, B. Mustapha, F. Rejmund, K. -H. Schmidt, C. Stéphan, L. Tassan-Got, C. Volant, “Isotopic production cross sections of fission residues in 197Au-on-proton collisions at 800 A MeV," *Nuclear Physics A* 683, 2001 513-539.

[16] F. Rejmund, B. Mustapha, P. Armbruster, J. Benlliure, M. Bernas, A. Boudard, J. P. Dufour, T. Enqvist, R. Legrain, S. Leray, K. -H. Schmidt, C. Stéphan, J. Taieb, L. Tassan-Got, C. Volant, "Measurement of isotopic cross sections of spallation residues in 800 A MeV 197Au+p collisions," *Nuclear Physics A* 683, 2001, pp. 540-565.

[17] R. Michel, R. Bodemann, H. Busemann, R. Daunke, M. Gloris, H. -J. Lange, B. Klug, A. Krins, I. Leya, M. Lüpke, S. Neumann, H. Reinhardt, M. Schnatz-Büttgen, U. Herpers, Th. Schiekel, F. Sudbrock, B. Holmqvist, H. Condé, P. Malmborg, M. Suter, B. Dittrich-Hannen, P. -W. Kubik, H. -A. Synal, D. Filges, "Cross sections for the production of residual nuclides by low- and medium-energy protons from the target elements C, N, O, Mg, Al, Si, Ca, Ti, V, Mn, Fe, Co, Ni, Cu, Sr, Y, Zr, Nb, Ba and Au," *Nuclear Instruments and Methods in Physics Research B* 129, 1997, pp. 153-193.

[18] Y. Asano, S. Mori, M. Noguchi, M. Sakano, K. Katoh, K. Kondo, "Spallation and fission yields in the interactions of tantalum, tungsten, and gold with 500-MeV protons," *Journal of the Physical Society of Japan* 54(10), 1985, pp.3734-41.

[19] Von E. Ross, K. Bachmann, "Fission of gold with 580-MeV protons," *Radiochimica Acta* 21(1-2), 1974, pp. 13-20.

[20] R. Michel, B. Dittrich, U. Herpers, F. Peiffer, T. Schiffmann, P. Cloth, P. Dragovitsch, D. Filges, "Proton-induced spallation at 600 MeV," *Analyst* 114, 1989, 89.

[21] Yu. E. Titarenko, V. F. Batyaev, V. M. Zhivun, A. B. Koldobsky, Yu. V. Trebukhovsky, E. I. Karpikhin, R. D. Mulambetov, S. V. Mulambetova, Yu. V. Nekrasov, A. Yu Titeranko, K. A. Lipatov, S. G. Mashnik, R. E. Prael, K. Gudima, M. Baznat, “Cross Sections for Nuclide Production in 1 GeV Proton-Irradiated 208Pb and 0.8 GeV Proton-Irradiated 197Au," *Proceedings of the Sixth International Meeting on Nuclear Applications of Accelerator Technology, Accelerator Applications in a Nuclear Renaissance*, American Nuclear Society 2003.

[22] Stepan G. Mashnik, Richard E. Prael, Arnold J. Sierk, Vyacheslav F. Batyaev, Svetlana V. Kvasova, Ruslan D. Mulambetov, and Yury E. Titeranko, “Benchmarking Ten Codes Against the Recent GSI Measurements of the Nuclide Yields from 208Pb, 197Au, and 238U + p Reactions at 1 GeV/nucleon," LANL Report, LA-UR-01-5391, 2001.

[23] L. Audouin, L. Tassan-Got, P. Armbruster, J. Benlliure, M. Bernas, A. Boudard, E. Casarejos, S. Czajkowski, T. Enqvist, B. Fernández-Domínguez, B. Jurado, R. Legrain, S. Leray, B. Mustapha, J. Pereira, M. Pravikoff, F. Rejmund, M.-V. Ricciardi, K.-H. Schmidt, C. Stéphan, J. Taieb, C. Volant, W. Wlazło, “Evaporation residues produced in spallation of 208Pb by protons at 500A MeV”, *Nuclear Physics A*, Volume 768, Issues 1–2, 2006, pp. 1-21.

[24] T Enqvist, W Wlazło, P Armbruster, J Benlliure, M Bernas, A Boudard, S Czajkowski, R Legrain, S Leray, B Mustapha, M Pravikoff, F Rejmund, K.-H Schmidt, C Stéphan, J Taieb, L Tassan-Got, C Volant, “Isotopic yields and kinetic energies of primary residues in 1 A GeV 208Pb+p reactions,” *Nuclear Physics A*, Volume 686, Issues 1–4, 2001, pp. 481-524.

[25] J. Taïeb, K.-H. Schmidt, L. Tassan-Got, P. Armbruster, J. Benlliure, M. Bernas, A. Boudard, E. Casarejos, S. Czajkowski, T. Enqvist, R. Legrain, S. Leray, B. Mustapha, M. Pravikoff, F. Rejmund, C. Stéphan, C. Volant, W. Wlazło, “Evaporation residues produced in the spallation reaction 238U+p at 1 A GeV,” *Nuclear Physics A*, Volume 724, Issues 3–4, 2003, pp. 413-430.

[26] M. Bernas, P. Armbruster, J. Benlliure, A. Boudard, E. Casarejos, S. Czajkowski, T. Enqvist, R. Legrain, S. Leray, B. Mustapha, P. Napolitani, J. Pereira, F. Rejmund, M.-V. Ricciardi, K.-H. Schmidt, C. Stéphan, J. Taieb, L. Tassan-Got, C. Volant, “Fission-residues produced in the spallation reaction 238U + p at 1 A GeV,” *Nuclear Physics A*, Volume 725, 2003, pp. 213-253.

[27] M. V. Ricciardi, P. Armbruster, J. Benlliure, M. Bernas, A. Boudard, S. Czajkowski, T. Enqvist, A. Kelić, S. Leray, R. Legrain, B. Mustapha, J. Pereira, F. Rejmund, K.-H. Schmidt, C. Stéphan, L. Tassan-Got, C. Volant, and O. Yordanov, “Light nuclides produced in the proton-induced spallation of ^{238}U at 1 GeV” Phys. Rev. C 73, 2006

[28] M. Bernas, P. Armbruster, J. Benlliure, A. Boudard, E. Casarejos, T. Enqvist, A. Kelic, R. Legrain, S. Leray, J. Pereira, F. Rejmund, M.-V. Ricciardi, K.-H. Schmidt, C. Stéphan, J. Taieb, L. Tassan-Got, C. Volant, “Very heavy fission fragments produced in the spallation reaction 238U+p at 1 A GeV”, *Nuclear Physics A*, Volume 765, Issues 1–2, 2006, pp. 197-210.

[29] J. Tobailem, "Sections Efficaces des Reactions Nucleaires Indutes par Protons, Deuterons, Particles Alphas. V. Silicium," Report CEA-N-1466(5), Saclay, 1981.

[30] G. L. Morgan, K. R. Alrick, A. Saunders, F. C. Cverna, N. S. P. King, F. E. Merrill, L. S. Waters, A. S. Carroll, A. L. Hanson, R. P. Liljestrand, R. T. Thompson, E. A. Henry, "Total cross sections for production of 22Na and 24Na

in proton-induced reactions on 27Al from 0.4 to 22 GeV," *Nuclear Instruments and Methods in Physics Research B* 211, 2003, pp. 297-304.

[31] R. Michel, M. Gloris, H. -J. Lange, I. Leya, M. Lüpke, U. Herpers, B. Dittrich-Hannen, R. Rösel, Th. Schiekel, D. Filges, P. Dragovitsch, M. Suter, H. -J. Hofmann, W. Wölfli, P. W. Kubik, H. Baur, R. Wieler, "Nuclide production by proton-induced reactions on elements (6· Z ·29) in the energy range from 800 to 2600 MeV," *Nuclear Instruments and Methods in Physics Research B* 103, 1995, pp. 183-222.

[32] T. N. Taddeucci, J. Ullmann, L. J. Rybarcyk, G. W. Butler, T. E. Ward, "Total cross sections for production of 7Be, 22Na, and 24Na in p+7Li and p+27Al reactions at 495 and 795 MeV," *Physical Review C* 55, 1997, pp. 1551-1554.

[33] H. R. Heydegger, Anthony L. TurkeVich, A. Van Ginneken, P. H. Walpole, "Production of 7Be, 22Na, and 28Mg, from Mg, Al, and SiO2 by protons between 82 and 800 MeV," *Physical Review C* 14(4), 1976, pp. 1506-1514.

[34] G. I. Krupnyi, D. V. Snitko, A. A. Yanovich, "Cross sections of the reactions 27Al(p,spall)7Be, 27Al(p,3p3n)22Na, and 27Al(p,3pn)24Na in the proton energy range 37 MeV-70 GeV," *Atomic Energy* 89(5), 2000, pp. 939-941.

[35] H. Vonach, A. Pavlik, A. Wallner, M. Drosg, R. C. Haight, D. M. Drake, S. Chiba, "Spallation reactions in 27Al and 56Fe induced by 800 MeV protons," *Physical Review C* 55(5), 1997, pp. 2458-2467.

[36] Genie2000™, Canberra Industries, Version 3.2b

[37] Z. Wang, “Design of a Boron Neutron Capture Enhanced Fast Neutron Therapy Assembly” Ph.D Dissertation, Georgia Institute of Technology, 2006

[38] J. Tull, *Nuclear Wallet Card,* National Nuclear Data Center, Brookhaven National Laboratory, 2005

[39] M. Gloris, R, Michel, F. Sudbrock, U. Herpers, P. Malmborg, B. Holmqvist, “*Proton-induced Production of Residual Radionuclides in Lead at Intermediate Energies*”, Nuclear Instruments and Methods in Physics Research A, 463, 2001, pp 593-633

[40] A. Sonzogni, NUDAT data files, National Nuclear Data Center, Brookhaven National Laboratory 1997

[41] ICRP, 2008 *Nuclear Decay Data for Dosimetric Calculations,* ICRP Publication 107. Annals of the ICRP 38(3)

[42] K. Kelley, “Gadolinium-148 and Other Spallation Production Cross Section Measurements for Accelerator Target Facilities” Ph.D. Dissertation, Georgia Institute of Technology, 2004

[43] ICRP, 1994 *Dose Coefficients for Intakes of Radionuclides by Workers,* ICRP Publication 68, Annals of the ICRP 24(4)

[44] T. Sato, K. Niita, N. Matsuda, S. Hashimoto, Y. Iwamoto, S. Noda, T. Ogawa, H. Iwase, H. Nakashima, T. Fukahori, K. Okumura, T. Kai, S. Chiba, T. Furuta and L. Sihver, *Particle and Heavy Ion Transport Code System PHITS*, Version 2.52, J. Nucl. Sci. Technol. 50:9, 913-923 (2013)

[45] T.T. Böhlen, F. Cerutti, M.P.W. Chin, A. Fassò, A. Ferrari, P.G. Ortega, A. Mairani, P.R. Sala, G. Smirnov and V. Vlachoudis, "*The FLUKA Code: Developments and Challenges for High Energy and Medical Applications*", Nuclear Data Sheets 120, 211-214 (2014)

[46] A. Ferrari, P.R. Sala, A. Fasso`, and J. Ranft, "*FLUKA: a multi-particle transport code*", CERN-2005-10 (2005), INFN/TC_05/11, SLAC-R-773

[47] J. Allison, et al., *"GEANT4-a simulation toolkit"*, Nuclear Instruments and Methods in Physics Research A, 506(3), 2003, pp 250-303

[48] J. Allison, et al., "*GEANT4 developments and applications*", IEEE Transactions on Nuclear Science, 53(1), 2006, pp 270-278

[49] R. Serber, Phys. Rev 72, 1114 (1947)

[50] X-5 Monte Carlo Team, "*MCNP – A General Monte Carlo N-Particle Transport Code, Version 5*", LA-CP-03-0245, 2003

[51] T.A. Gabriel, et al. "*The High Energy Transport Code HETC*", ORNL/TM-9727, 1985

[52] Federal Guidance Report No. 12, "*External Exposure to Radionuclides in Air, Water and Soil*", EPA 402-R-93-081, 1993